UNIVERSIDADE FEDERAL DE PERNAMBUCO
CENTRO DE CIÊNCIAS EXATAS E DA NATUREZA
PROGRAMA DE PÓS-GRADUAÇÃO EM FÍSICA

Jefferson Augusto de Oliveira Galindo

Luminescence-based nanothermometry with lanthanide codoped yttria single nanoparticles and individual nitrogen-vacancy defects in nanodiamonds

Recife

2022

Jefferson Augusto de Oliveira Galindo

Luminescence-based nanothermometry with lanthanide codoped yttria single nanoparticles and individual nitrogen-vacancy defects in nanodiamonds

Tese apresentada ao Programa de Pós-Graduação em Física do Departamento de Física da Universidade Federal de Pernambuco como parte dos requisitos para obtenção do título de Doutor em Física.

Área de Concentração: Óptica

Orientador: Leonardo de Souza Menezes

Recife

2022

Catalogação na fonte
Bibliotecária Nataly Soares Leite Moro, CRB4-1722

G158l Galindo, Jefferson Augusto de Oliveira
Luminescence-based nanothermometry with lanthanide codoped yttria single nanoparticles and individual nitrogen-vacancy defects in nanodiamonds / Jefferson Augusto de Oliveira Galindo. – 2022.
138 f.: il., fig., tab.

Orientador: Leonardo de Souza Menezes.
Tese (Doutorado) – Universidade Federal de Pernambuco. CCEN, Física, Recife, 2022.
Inclui referências.

1. Óptica. 2. Nanotermometria de luminescência. 3. Íons de lantanídeos. 4. Nanodiamante. 5. Ressonância eletrônica de spin. I. Menezes, Leonardo de Souza (orientador). II. Título.

535.2 CDD (23. ed.) UFPE- CCEN 2022 - 65

JEFFERSON AUGUSTO DE OLIVEIRA GALINDO

LUMINESCENCE-BASED NANOTHERMOMETRY WITH LANTHANIDE CODOPED YTTRIA SINGLE NANOPARTICLES AND INDIVIDUAL NITROGEN-VACANCY DEFECTS IN NANODIAMONDS

Tese apresentada ao Programa de Pós-Graduação em Física da Universidade Federal de Pernambuco, como requisito parcial para a obtenção do título de Doutor em Física.

Aprovada em: 30/03/2022.

BANCA EXAMINADORA

Prof. Leonardo de Souza Menezes
Orientador
Universidade Federal de Pernambuco

Prof. Lúcio Hora Acioli
Examinador Interno
Universidade Federal de Pernambuco

Prof. Marcio Heraclyto Gonçalves de Miranda
Examinador Interno
Universidade Federal de Pernambuco

Prof. André de Lima Moura
Examinador Externo
Universidade Federal de Alagoas

Prof. Nikifor Rakov Gomez
Examinador Externo
Universidade Federal do Vale do São Francisco

This Thesis is dedicated to my parents Marilane and José and to my brother Valter. I love you!

ACKNOWLEDGEMENTS

This Thesis and the work in the last four years would not have been possible without the support of many people. I would like to start by thanking my advisor Prof. Leonardo Menezes, who took me by hand and gave me the opportunity to discover and work with this exciting research field. He encouraged me all the way through, specially in the darkest hours, expressing his confidence and giving me the freedom to choose my way to get to the results presented in this Thesis. I really appreciated that.

I want to thank Prof. Anderson Amaral for the valuable contributions, fruitful discussions and good laughs during the past year and half. Without your insightful considerations and advice much of this work would not be possible. My best regards, Professor.

I cannot forget to thank my colleagues from the UFPE Nano-Optics Laboratory: Igor for the important conversations; Edwin for teaching me most of the techniques learned during the doctorate's period and for teaching me how to have the necessary courage and patience to carry on; Rodrigo for the valuable discussions and instructions; and of course, Allison "the brilliant boy", who shared with me the last two years in a dark and cold laboratory carrying out endless and unsuccessful experiences, sharing the worst kind of infamous jokes and complaints and helping me out with theoretical discussions and data analysis... we have much more to do, man! My time with you guys is unforgettable, thank you for everything!

Thanks to my peers at the Physics and Materials Science departments/UFPE Manoel, Jessica, Cecília, Winnie, Felipe, Tawan, Joyce, Alisson, Melissa and Pollyanna with whom I shared funny moments in the halls, online meetings and laboratories. Furthermore, I am truly grateful to the professors of the Physics Department/UFPE: Cid B. de Araújo, Anderson S. L. Gomes, Clécio C. de S. Silva, José R. R. Leite, José W. R. Tabosa, Lúcio H. Acioli, Eduardo P. Hernándes and Márcio H. G. de Miranda. Whether on the advanced courses, seminars or casual meetings at the department, you were fundamental to my scientific formation.

I like to thank the technicians Daniel from the Electronic Workshop/DF and Virginia/DF from the Chemistry Lab for saving my life and my research so many times when I was in trouble.

A special thanks to Luis Fernando dos Santos and prof. Rogéria R. Gonçalves and from the Laboratory of Micro and Nanostructured Luminescent Materials at the USP - Ribeirão Preto, who provided the lanthanide-doped yttria nanocrystals. Without your estimated collaboration,

this work would not be possible.

Thanks to my dear friend Gizele, for sharing with me the last ten years of academic formation. You more than anyone knows the arduous path we need to walk to get here. To Amanda, the sympathy in person, and Alexandre, who who were my housemates during years, I would like to thank you. Also, a big hug to my friends from the times at Nevinha's house Marcione and Ari. Thanks to Márcio, Genicélia, Diego and Ruann, my oldest and closest friends. For sharing the worst times with me, you all live in my fondest memories.

For most important people in my life, my family and specially my parents and brother who believed and supported me when no one else did. I am very thankful for every sacrifice made by them for giving me education. I would never be able to thank them enough. Thanks Aryane, my girlfriend, for having enough patience to put up with me through the hardest years of graduate school.

ABSTRACT

In the last two decades, the development of nanoscale luminescent materials presenting temperature-dependent optical properties led to the emergence of the so-called luminescence-based nanothermometers. Nowadays, these sensing devices are responsible for unveiling temperature related phenomena at the micro- and nanometric scales. However, most of the current literature on luminescence nanothermometry reports ensemble averaged data, which neglects the particular characteristics of each nanothermometer, leading to important inaccuracies in the temperature measurements. Therefore, in this work, the thermal sensing capabilities of individual luminescent nanothermometers are investigated through the use of two different techniques in a temperature range compatible with biological systems. The first study consists on characterizing the same five individual Yb^{3+}/Er^{3+}codoped yttria nanocrystals (NCs) as nanothermometers in different environments (air, water and ethylene glycol) applying the Luminescence Intensity Ratio (LIR) technique. The second study reports on the characterization of individual nanodiamonds containing a single negatively charged nitrogen-vacancy defect (NV^{-}) as nanothermometers *via* Optically Detected Magnetic Resonance technique. The obtained LIR results show that the thermometric behavior of each NC in air and water are equivalent, returning relative sensitivities (S_R) and thermal resolutions (δT) as high as 2.3 $\%$ K^{-1} and 0.4 K, respectively. It was also observed that S_R and δT for each nanothermometer can be much more precisely determined than those obtained from the average on the set of five NCs. The increased uncertainties of the average parameters are related to the NC's size variations, which manifest through the differences on the surface/volume ratio between the selected NCs. This assumption is reinforced by the observed correlation between the single-NC thermometric parameters with the NC brightness. In addition, the relevance of the NC-solvent interaction becomes evident when the NCs are embedded in ethylene glycol, for which molecular vibrational modes can resonantly interact with the Er^{3+} ions electronic excited states. Meanwhile, results on nanothermometry with single NV^{-} defects on nanodiamonds also present differences on the measured thermal parameters. A linear dependence of the electron spin resonances (ESR) with temperature was observed for three nanodiamonds and varies from -88 kHz K^{-1} to -110 kHz K^{-1}. The distinct thermal responses may be due to the presence of structural defects, impurities and inner strain of each nanodiamond. This argument is reinforced by the observed correlation between the measured strain parameter and the temperature dependency of the ESR frequencies for each nanodiamond. These results corroborate those obtained for the individual lanthanide-doped nanothermometers. Also, an Arduino-based ESR tracking system is implemented to continuously monitor temperature changes of the sample with a nanodiamond, reaching δT values on the order of 1.7 K. Such system may be implemented to measure spatial temperature inhomogeneities with spatial resolutions only limited by the nanodiamond size ($\sim$25 nm). The results reported in this Thesis point out to the importance of the calibration of individual luminescent nanothermometers and its interaction with the surrounding medium, reinforcing the ultra-high resolution thermal sensing capabilities of both nanothermometric systems.

Keywords: luminescence nanothermometry; lanthanide ions; nanodiamond; electron spin resonance; scanning optical microscopy.

RESUMO

Nas últimas duas décadas, o desenvolvimento de materiais luminescentes em nanoescala que apresentam propriedades ópticas dependentes foi responsável pelo surgimento dos nanotermômetros luminescentes. Atualmente, esses sensores são os principais responsáveis por desvendar os fenômenos relacionados à temperatura na escala sub-micrométrica. Contudo, a maior parte da literatura atual sobre nanotermometria de luminescência relata dados obtidos com ensembles, negligenciando as características particulares de cada nanotermômetros, podendo levar a imprecisões importantes nas medidas de temperatura. Portanto, neste trabalho, as capacidades de sensoriamento térmico de nanotermômetros individuais são investigadas através do uso de duas técnicas diferentes. Mais especificamente, esta Tese relata e discute dois estudos experimentais sobre nanotermometria. O primeiro consiste em caracterizar como nanotermômetros os mesmos cinco nanocristais (NCs) de ítria codopados com Yb^{3+}/Er^{3+} em diferentes ambientes (ar, água e etilenoglicol) aplicando a técnica de Razão de Intensidade de Luminescência (LIR). O segundo estudo relata a caracterização de nanodiamantes individuais contendo um único defeito de nitrogênio-vacância (NV$^-$) como nanotermômetros luminescentes, através da técnica de Ressonância Magnética Opticamente Detectada. Os resultados obtidos com LIR mostram que o comportamento termométrico de cada NC no ar e na água são equivalentes, retornando sensitividades relativas (S_R) e resoluções térmicas (δT) máximas de 2.3 $\%$ K^{-1} e 0.4 K, respectivamente. Observou-se também que S_R e δT de cada nanotermômetro podem ser determinados com maior precisão se comparados àqueles obtidos a partir da média dos cinco NCs. As maiores incertezas dos parâmetros médios estão relacionadas às variações de tamanho dos NCs, manifestando-se através da relação superfície/volume dos NCs selecionados. Esta suposição é reforçada pela observação de uma correlação entre os parâmetros termométricos dos NCs individuais com o seu brilho. Além disso, a relevância da interação NC-solvente torna-se evidente quando estes são embebidos em etilenoglicol, onde os modos vibracionais moleculares podem interagir de forma ressonante com os estados excitados eletrônicos dos íons de Er^{3+}. Enquanto isso, os resultados de nanotermometria com defeitos NV$^-$ únicos também apresentam diferenças em S_R e δT entre os nanotermômetros selecionados. Foi observada uma dependência linear das frequências de ressonância eletrônica de spin (ESR) dos defeitos com a temperatura, variando entre -88 kHz K^{-1} a -110 kHz K^{-1} para os três nanodiamantes. As diferentes respostas térmicas podem ser causadas por defeitos estruturais, impurezas e tensão interna. Esse argumento é reforçado pela correlação observada entre o parâmetro de tensão medido e a dependência das frequências ESR com a temperatura para cada nanodiamante. Os resultados corroboram aqueles obtidos para os nanotermômetros individuais codopados com íons lantanídeos. Ademais, um sistema de rastreamento de frequências de ESR baseado em Arduino é implementado para monitorar continuamente a temperatura da amostra com um nanodiamante, atingindo δT da ordem de 1.7 K. Este sistema de monitoramento pode ser implementado para medir inomogeneidades de temperatura com resolução espacial limitada apenas pelo tamanho do nanotermômetro (~25 nm). Portanto, estes resultados apontam para a importância da calibração de nanotermômetros luminescentes individuais e sua interação com o ambiente, reforçando as capacidades de sensoriamento térmico de altíssima resolução de ambos sistemas nanotermométricos.

Palavras-chaves: nanotermometria de luminescência; íons de lantanídeos; nanodiamante; ressonância eletrônica de spin; microscopia óptica de varredura.

LIST OF FIGURES

LIST OF TABLES

LIST OF ABBREVIATIONS AND ACRONYMS

CW	Continuous wave
ET	Energy transfer
ESA	Excited state absorption
ESR	Electron spin resonance
GSA	Ground state absorption
HBT	Hanbury-Brown and Twiss
LIR	Luminescence Intensity Ratio
MP	Multiphonon
MW	Microwave
NC	Nanocrystal
NIR	Near-infrared
NV	Nitrogen-vacancy defect
NV^0	Neutral nitrogen-vacancy defect
NV^-	Negatively charged nitrogen-vacancy defect
ODMR	Optically Detected Magnetic Resonance
TCSPC	Time-Correlated Single-Photon Counter
TTL	Transistor-Transistor-Logic
UC	Upconversion
UV	Ultraviolet
ZFS	Zero-field splitting

LIST OF SYMBOLS

ΔE	Energy gap between coupled energy levels
Δf	Half width at half maximum of electron spin resonance of nitrogen-vacancy defects
ΔT	Temperature difference
δT	Thermal resolution
ε	Intrinsic bulk strain
ϵ_{gs}	hydrostatic pressure shift of the zero-field splitting of nitrogen-vacancy defects
γ_i	Spontaneous emission rate from excited state i
λ	Wavelength
τ	Excited state lifetime
ν_i	Emission frequencies from the excited state i
$\nu_\pm$	Electron spin resonance frequencies of spin sublevels ± 1
μ_B	Bohr magneton
σ	Tensile strain
$\mathcal{B}$	Bulk modulus of diamond
$\mathcal{D}_{gs}$	Zero-field splitting for the ground state of nitrogen-vacancy defects
$\mathcal{D}_{es}$	Zero-field splitting for the excited state of nitrogen-vacancy defects
$\mathcal{E}$	Strain parameter for nitrogen-vacancy defects on diamonds
$FWHM$	Full-width at half maximum
g	Landé factor
g_i	Degeneracies of the energy state i

$g^{(2)}(\tau)$	Second order correlation function
h	Planck's constant
$\hbar$	Reduced Planck's constant
I	Emission intensity
J_i	Total angular momentum of the energy state i
k_B	Boltzmann's constant
Ln^{3+}	Trivalent lanthanide ions
m_{gs}	Spin projection of the ground state of nitrogen-vacancy defects
m_{es}	Spin projection of the excited state of nitrogen-vacancy defects
$N.A.$	Numerical aperture
$\mathcal{P}$	Excitation power density
P	Average excitation power
PSF	Point Spread Function
S	Thermal sensitivity
S_R	Relative thermal sensitivity
S_R^{LIR}	Relative thermal sensitivity obtained through LIR technique
S_R^{ODMR}	Relative thermal sensitivity obtained through ODMR technique

CONTENTS

1 INTRODUCTION

The description of several phenomena found in nature relies on the determination of one of the most fundamental physical quantities ever investigated by mankind: temperature. It can be described as the manifestation of thermal energy present in all matter, being a measure of coldness or hotness expressed in several arbitrary scales and indicates the direction that heat energy spontaneously flows between bodies with different temperatures. Temperature-dependent phenomena manifest themselves in the most extreme situations of nature, from the greatest and hottest - as the early moments of the Big-Bang with temperatures up to 10^{32} K [1] - to the coldest and smaller phenomena - as the temperatures obtained in ultra-cold Bose-Einstein condensates comprising a thousand atoms, reaching outstanding 38×10^{-12} K [2].

The first discussions on the thermal behavior of bodies go all way back to the ancient Greece, as depicted by the ideas of *hot* and *cold* discussed by Aristotle whose definitions lasted for about two thousand years [3]. However, quantitative temperature investigations of natural phenomena could only be possible due to the advent of the first thermometers, as the water thermoscope invented by Galileo Galilei in 1596 and the mercury thermometer built by Daniel G. Fahrenheit in 1714 [3]. Such sensing devices were based on the fact that some materials present physical properties strongly dependent on temperature. In the two mentioned cases, the temperature measurements were possible due to the physical phenomenon of thermal dilation, in which the the volume of the liquids (water and mercury) are dependent on temperature. The development of these sensing devices significantly contributed to the first studies in physics, chemistry, medicine and biology.

Currently, the miniaturization of electronic systems and the investigation of physical/biological phenomena down to the micrometric (10^{-6} m) and nanometric (10^{-9} m) scale have led to the necessity of developing thermal sensors with similar scales. Investigating such small structures creates the demand of developing non-invasive sensing methods in order to preserve the physical integrity of the investigated system and to assure the non-interference of the sensing device. Thus, at first sight, it seems impossible to find a way to measure physical quantities as temperature with nanometric spatial resolution *via* non-invasive methods. However, a possible alternative to this to this problem is direct and simple: light!

The recent advances on synthesis of luminescent materials presenting interesting temperature-dependent physical phenomena allowed the development of thermometers in the nanometric scale, capable of obtaining the local temperature of sub-micrometric structures in a non-invasive way. These modern nanoscale thermal sensors, named luminescent nanothermometers, are based on the temperature dependence of the light emitted by specific materials. Similar to the first developed nanothermometers, in this case, a temperature-related physical phenomenon - luminescence - can be used to determine the temperature of a system, leading the possible applications of thermometry to a new level regarding spatial and thermal resolution.

The number of current candidates for luminescent thermometry are practically countless [4]. Among the current temperature-sensing strategies, those based on luminescence intensity, excited state lifetime, peak position, fluorescence polarization anisotropy, emission/excitation emission intensity ratio and optically detected magnetic resonance can be mentioned [5]. To get a better idea concerning the capabilities of luminescence nanothermometry, such techniques were responsible for unveiling the temperature-governed underlying mechanisms of heat transport in living cells [6]; heterogeneous temperature distribution in cell organelles [7]; diagnosis of subcutaneous tissue inflammation *in-vivo* [8]; and contactless monitoring of local heat dissipation on microelectronic devices [9].

However, the current nanothermometry sensing studies are often performed with ensembles of nanoparticles which may lead to inaccurate temperature readings depending on the homogeneity of the nanothermometers. For instance, spatially resolved temperature measurements performed with ensembles of intensity-based nanothermometers may present temperature misreadings if the local distribution of nanoparticles fluctuate with time or spatial position [5]. Other studies presented a dependence on size of the thermal responses of intensity ratio-based nanosensors [10, 11], which may cause temperature reading errors depending on the size inhomogeneity of the nanoparticles on a ensemble. Thus, the use of a single calibrated nanothermometer is the best alternative to overcome these problems [5].

The interaction between a thermometer and its surrounding medium is a *sine qua non* condition for the operation of the thermometer. This means that the interaction must not modify the thermometer sensing properties. In real application scenarios, the nanothermometer is usually used to determine the temperature inside biological and complex chemical media. However, the behavior of luminescent centers close to the surface may change significantly due to nanocrystal (NC) surface defects [12] or quenching induced by energy transfer to vibrational modes on nearby molecules [13, 11]. Therefore, the influence of the surrounding environment on the thermal response of the nanothermometers must to be taken in account in order to obtain precise temperature measurements.

Due to the aforementioned relevance on the development of efficient and precise luminescent nanothermometers, this Thesis brings results on the investigation of the thermal sensing capabilities of single luminescent nanothermometers through the use of different temperature-sensing techniques, carried out in two major experiments. The first one focuses on studying the influence of the environment on the thermal response of individual yttria (Y_2O_3) NCs codoped with Yb^{3+} and Er^{3+} through Luminescence Intensity Ratio (LIR) technique. It is based on the spectroscopic analysis of the upconversion (UC) emission intensities from the $^2H_{11/2}$ and $^4S_{3/2}$ excited states of Er^{3+} ions under near infrared excitation. The experiment was carried out by measuring the thermal sensing capabilities of five individual NCs on three different environments: air, water and ethylene glycol. The thermal responses were quantitatively obtained through the ratio between the integrated luminescence intensities of the Er^{3+} green emission lines centered at 528 nm and 550 nm under 977 nm excitation light. The experimental setup consists in an inverted sample-scanning optical microscope which allows the identification and spatial localization of single NCs spread over a glass coverslip through their emitted luminescence. In addition, in order to investigate the NCs in the chosen environments, a liquid deposition protocol was developed and is reported in detail on chapter 3.

The second major experiment is based on investigating the thermal sensing capabilities of single negatively charged nitrogen-vacancy (NV^-) defects on nanodiamonds. This study was carried out with the aim of monitoring the temperature of a sample through the use of Optically Detected Magnetic Resonance (ODMR) temperature-sensing technique. This nanothermometry technique is based on the optical detection of the NV^- electron spin resonances (ESRs) under CW illumination. To detect the luminescent nanodiamonds, a home-assembled confocal optical microscope associated with a Hanbury-Brown and Twiss (HBT) interferometer was used to identify and localize the single emitters through their emitted red luminescence (600 nm to 800 nm wavelength) under 532 nm laser excitation light. The experimental setup used in this study and the deposition of fluorescent nanodiamonds over a photolithographed microwave (MW) antenna allow the identification of individual NV^- defects and the obtaining of their thermal responses *via* ODMR measurements. With the nanothermometers calibrated, a low-cost ESR tracking system based on Arduino Due-LabVIEW interface is then used to monitor the temperature of the sample with a nanodiamond containing a single NV^- defect.

The work is organized as follows. In chapter 2 the main concepts about luminescence nanothermometry with single NCs are presented along with the fundamental principles of LIR and ODMR temperature-sensing techniques. The discussions about the two implemented techniques are followed by the main justifications of using codoped lanthanide ions and single NV^{-} defects on nanodiamonds for nanothermometry purposes. Still in this chapter, the concepts of relative sensitivity and thermal resolution are discussed, including the methods implemented in this work for determine these parameters for single nanothermometers. Chapter 2 is finalized with a discussion on the fundamentals of the high-resolution luminescence microscopy techniques used in this Thesis. Chapter 3 brings the results on the experiments about the environment influence on the thermal response of individual LIR-based Y_2O_3:Yb^{3+}/Er^{3+}nanothermometers. In chapter 4 the experimental results on real-time nanothermometry with single NV^{-} defects are reported. Finally, in chapter 5 the conclusions and perspectives of this Thesis are presented.

2 LUMINESCENCE NANOTHERMOMETRY WITH SINGLE NANOPARTICLES

As previously mentioned, current advances on the investigations of temperature variations on sub-micron scale systems result in a demand to develop non-invasive nanothermometry methods. The cornerstone of current nanothermometry is the fact that some materials present luminescent properties that are strongly dependent on temperature, which can lead to the development of temperature sensors at nanoscale with high thermal sensitivity and spatial resolution [4]. Thanks to modern physicochemical synthesis routes, the discovery of new temperature-dependent properties in a range of luminescent materials broadened the possibilities of nanoscale thermal sensing techniques [5]. The current sensing strategies employed for performing nanothermometry are based on the temperature dependence of the molecular-, atomic- and even electronic-scale dynamics of a given nanothermometer. Each of these dynamics may be phenomenologically measured through optical indicators such emission intensity, absorption/emission peak position, excited state lifetime, electron spin resonance, optically detected magnetic resonance, and others [4, 5].

Among the luminescence-based nanothermometry techniques, two specific sensing strategies can be highlighted due to recent advances in high resolution nanothermometry: LIR and ODMR. The temperature-dependent behavior of the optically detectable luminescence for both techniques is schematically represented in Figure 1. The LIR technique can return temperature values by monitoring the ratio between the integrated intensity of two emission or excitation peaks [Figure 1a)]. Meanwhile, thermometers based on the ODMR technique [Figure 1b)] rely on the temperature dependence of the spin resonance of nitrogen-vacancy defects, which can be optically detected through a coherent control of the spin states with microwave pulses. In this sense, this chapter will present in more detail the LIR and ODMR techniques and the necessary physical properties that a system must present in order to be implemented as a nanothermometer.

Figure 1 – a) LIR and b) ODMR temperature sensing strategies for performing luminescence nanothermometry. The blue and red lines indicate the detected optical signals for low and high temperatures, respectively.

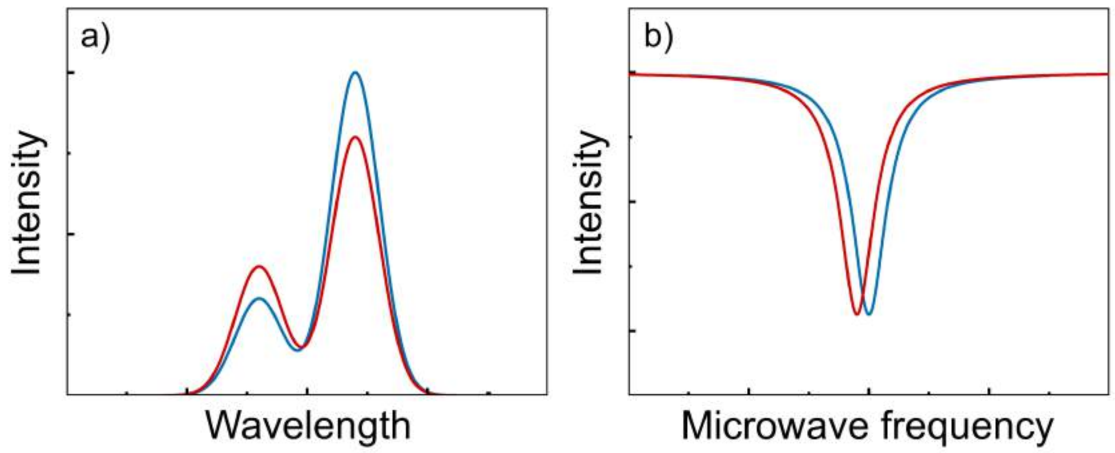

Font: The Author (2022)

2.1 LUMINESCENCE INTENSITY RATIO TECHNIQUE

As mentioned above, LIR-based luminescence thermometry is an experimental technique based on the ratio between the integrated emission intensities from two excited states of a given fluorophore. Before presenting the results obtained with this thermometric technique, it is necessary to introduce the physical properties that allow performing LIR nanothermometry. Thus, the current subsection is dedicated to understanding of the physical mechanisms behind the implementation of LIR nanothermometry. In order to do that, the fundamental concepts of statistical distribution of thermal population between two close lying energy states will be introduced, followed by the discussion of how multiphonon assisted processes are related to the energy UC processes in trivalent lanthanide ions (Ln^{3+})-doped solid state matrices In the sequence, the definition of LIR is formally presented. Next, the main reasons for performing LIR thermometry with Ln^{3+} complexes are presented, with a special emphasis on those justifying the LIR thermometry with Ln^{3+} codoped systems. Last but not least, discussions will be presented concerning the NC-solvent interactions on LIR-based nanothermometers, which are the main reason for investigating the interactions between individual nanothermometers and the outer environment, as will be shown in the experimental results on Chapter 3.

Figure 2 – Schematic representation of spontaneous Raman scattering depicting the emission of a a) Stokes photon and b) Anti-Stokes photon. Here, ν_L is the frequency of the excitation photons and ν_P is the frequency of the created or annihilated quantum of vibrational energy.

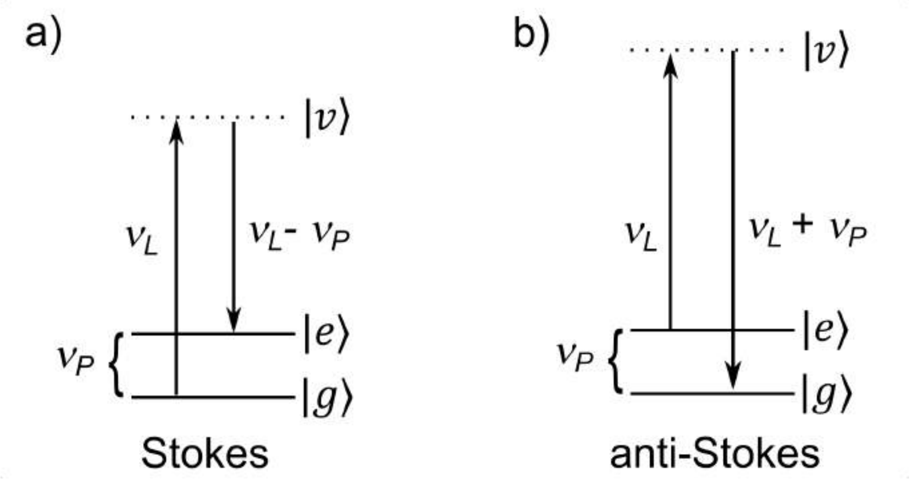

Font: Adapted from [15]

2.1.1 Statistical distribution of thermal population

In order to understand the underlying physical mechanisms which allows one to perform nanothermometry by implementing the LIR technique, it is interesting to discuss first a few physical processes, such as the Raman scattering. The reason for this will become clear soon. In Stokes Raman scattering, as depicted in Figure 2, the incident laser photon with frequency ν_L interacts with the material and is inelastically scattered by a molecule which can be excited to a high vibrational energy state associated with the electronic ground state manifold. In this picture, we can consider two vibrational levels: the ground state $|g\rangle$ and the first vibrational state $|e\rangle$ such that the energy separation between them is the vibrational energy $h\nu_P$ [14]. Thus, a laser photon may induce a transition through a virtual level, $|v\rangle$, simultaneously generating a Stokes-shifted photon with frequency $\nu_L - \nu_P$. The result is that the scattering leads the system to the vibrational level $|e\rangle$ and a quantum of molecular vibration (or the generation of a phonon in a crystalline lattice) was created. The creation of a quantum of vibration means that the molecular system becomes hotter. An opposite Raman scattering process happen, and is called anti-Stokes. In this situation, the sample is pumped with the same photon energy, but the molecule is initially found in its vibrational excited state $|e\rangle$. The interaction with the sample promotes the system to the virtual level $|v\rangle$ instantaneously generating an anti-Stokes photon with frequency $\nu_L + \nu_P$ which drives the system to its ground state $|g\rangle$. In this situation a vibrational excitation (or phonon) is annihilated and the molecule becomes colder [14].

The occupation probability distribution of the molecules' energy levels is related to the temperature of the system T through the Maxwell-Boltzmann statistics, given by [16]

$$N_{|e\rangle}(T) = N_{|g\rangle} e^{-\frac{\hbar \nu_P}{k_B T}}, \tag{2.1}$$

where $\hbar = h/2\pi$ is the reduced Planck's constant and k_B is the Boltzmann's constant. Equation 2.1 tells us that one fraction of the total population in the ensemble of molecules can reach the vibrational excited state $|e\rangle$ due to available thermal energy in the system. In this sense, one can refer to the two molecular energy states $|g\rangle$ and $|e\rangle$ as "thermally coupled energy levels" since their populations are intrinsically connected with the temperature of the system. Then, in spontaneous Raman scattering, since the intensity of the Stokes and anti-Stokes emissions are proportional to the population of molecules in the states $|g\rangle$ and $|e\rangle$, respectively, if one knows the molecular vibrational modes' energies activated in the Raman process and records the intensities of the Stokes and anti-Stokes Raman signals, one gets the temperature T of the molecular ensemble [14].

The aforementioned features are also found in solid-state systems, in which a quanta of vibration are defined as being quasi-particles with energy and momentum, called phonons, representing the collective oscillations of the crystalline matrix. Just as in the case of vibrational energy modes in molecules mentioned before, nonradiative transitions mediated by phonons of an ion in a crystalline matrix can either promote an ion to high energy levels or make the ion nonradiatively decay to lower energy states. These scenarios are possible because the energy gaps of close energy levels can be bridged by the annihilation or creation of matrix phonons, cooling or heating the matrix, respectively. Therefore, if an ion/atom in a crystal has a pair of thermally coupled energy levels and information about the physical characteristics of the system is available (absorption and emission spectra, for example), one can measure the energy difference between these two energy levels by recording the luminescence intensity of each emission line of the atom and determine the temperature of the sample. On the other hand, if one has information about the samples' temperature, one can get information about the matrix phonons, as the effective energy of the phonons, their density of states, etc. [14]

2.1.2 Multiphonon assisted processes

The discussion in 2.1.1 of the statistical distribution of thermal population is based on the assumption that the two thermally coupled energy levels have an energy difference that matches the maximum phonon frequency of the host matrix (see Figure 2). However, for some systems, such as matrices doped with Ln^{3+} (as discussed in the next chapter), the energy difference between two close energy levels is usually larger than the maximum phonon energy of the host matrix and the nonradiative transitions cannot be mediated by a single phonon. Thus, it means that energy UC processes in Ln^{3+} -doped crystals are possible due to multiphonon (MP) assisted processes. This possibility was first analyzed by Auzel *et al.* [17] who demonstrated that is possible to induce luminescence of Ln^{3+} in solids even when the energy difference between the two excited energy states of the ions is larger than the maximum phonon energy of the host material.

In order to understand the MP transitions in a solid state matrix it is interesting to write down the expression for the MP excitation rate [18]

$$\Lambda_{ij}(T) = W_{ij}^{NR}(T_0)[exp(\hbar\omega/k_BT) - 1]^{-q_{ij}}, \tag{2.2}$$

where $\hbar\omega$ is the energy of the cutoff phonons (discussed below), q_{ij} is the number of phonons involved in the MP excitation from level i to level j and $W_{ij}^{NR}(T_0)$ is the nonradiative decay rate from level j to level i determined by using the energy gap law at a given temperature (T_0) [19]

$$W_{ij}^{NR}(T_0) = \beta\ exp(-\alpha\Delta E_{ij}), \tag{2.3}$$

in which E_{ij} is the energy gap between the investigated energy levels i and j and the parameters α and β depend on the host matrix [19]. The population relaxation rate for a given energy state $\gamma = \gamma^{rad} + W^{NR}(T)$ depends on the radiative (γ^{rad}) and nonradiative [$W^{NR}(T)$] decay rates. As the radiative rates are usually temperature independent for Ln^{3+} [20], the nonradiative decay rate can be directly related to the MP processes and is given by [21]

$$W_{ij}^{NR}(T) = W_{ij}^{NR}(T_0)\left[\frac{1 - exp(\hbar\omega/k_BT)}{1 - exp(\hbar\omega/k_BT_0)}\right]^{-q}, \tag{2.4}$$

where q is the number of phonons involved in the nonradiative decay to the lowest energy level.

The cutoff energy phonon mode is important because the MP processes are described in the framework of perturbation theory. Thus, processes involving just one phonon will be treated as a first-order perturbation process being more probable than processes involving two phonons which are considered as second-order perturbation processes [14]. Therefore, the higher the cutoff phonon energy, the higher will be the probability of observing MP-assisted processes, *e.g.*, it is more probable to have a phonon-assisted process with a single high energy cutoff phonon than having the same process mediated by two phonons with half the energy of the cutoff phonon.

An exception or, as we can say, an addition to the discussion of the cutoff phonons is given by the fact that until now the phonon density of states for a given crystal host, *i.e.*, the number of phonon modes *per* unity of frequency *per* unity of volume of real space hasn't been taken into account. In real situations, the number of cutoff phonons can be small if compared with the number of phonons with smaller energy such that, effectively, all phonon modes of a given lattice are responsible for promoting the nonradiative transitions. Thus, in order to account for such phononic multi-mode processes, the MP assisted transitions can be described in terms of an "effective phonon mode" or "promoting mode" with a frequency smaller than the cutoff frequency of the host material [14]. This effective phonon energy represents a kind of weighted average between the phonon energies and the density of states for each phonon mode and will depend on the host matrix. This effect was verified in several studies [22, 23, 24] and can depend on the crystal size [25, 11], excitation power [26], and the interaction with the crystal and the surrounding medium [11, 27, 28]. Some of these dependencies imply different thermal responses of luminescent thermometers and these aspects are discussed in more detail in the next chapters when presenting the research results with individual codoped $\mathrm{Yb}^{3+}/\mathrm{Er}^{3+}$NCs. First, we need to introduce the luminescence based thermal sensing technique used in this work, which is the subject of the next subsection.

2.1.3 Definition of Luminescence Intensity Ratio

Having discussed the possibility of performing thermal measurements with solid-state systems due to MP processes, we can now present the LIR thermal sensing technique used to investigate some properties of luminescent nanothermometers based on Ln^{3+} compounds. For systems that possess an energy level structure with two thermally coupled levels, their thermal population distribution can be described by the Maxwell-Boltzmann statistics, introduced here as Equation 2.1. It is also known that for fluorescent materials, the population of a given energy level is proportional to the integrated fluorescence intensity originating from that very state. Consequently, one can obtain from Equation 2.1 a relation for the ratio between the populations of the two thermally coupled energy levels in the form

$$R = \frac{I_2}{I_1} = A \cdot exp\left(\frac{-\Delta E}{k_B T}\right), \tag{2.5}$$

here, I_i is the resulting luminescence intensity which arises from the electronic transition from high $(i = 2)$ and low $(i = 1)$ energy states to the ground state of a given system. The energy gap between the two states is given by ΔE ; T is the absolute temperature and A is a constant which depends both on the experimental apparatus used for detect the fluorescence and on spectroscopic parameters of the investigated material. The constant A can be expressed as [29]

$$A = \frac{c_2(\nu_2)\gamma_2 g_2 h\nu_2}{c_1(\nu_1)\gamma_1 g_1 h\nu_1}, \tag{2.6}$$

where $c_i(\nu_i)$ are the fluorescence collection efficiencies as function of the emission frequencies ν_i; γ_i is the spontaneous emission rate of each thermally coupled level; g_i is the degeneracy of the ith level and as before $i = 1, 2$ for the lower and high lying energy levels, respectively. In Equation 2.6, the dependence of A on the $c_i(\nu_i)$ terms may suggest that the LIR method isn't reproducible. However, as the emission lines of two thermally coupled energy levels are quite close in frequency, the collection efficiencies are also very similar and the detection system will be able to detect the fluorescence signal of both states [30]. Thus, it is a good approximation to consider the ratio $c_2(\nu_2)\nu_2/c_1(\nu_1)\nu_1 \approx 1$ and then rewrite the parameter A (Equation 2.6) as

$$A = \frac{\gamma_2 g_2}{\gamma_1 g_1}. \tag{2.7}$$

The expression above for the parameter A only depends on the spontaneous emission rates and the degeneracy of the thermally coupled energy levels. Depending on the luminescent material, the emission rates are dependent on the host matrix and the degeneracies (g_i) are usually given by the equation $g_i = 2J_i + 1$, where J_i is the total angular momentum of the ith energy level of the luminescent ion. [15].

There are some advantages in using the LIR technique over alternative thermometric techniques available for performing thermal sensing like the fluorescence lifetime technique. The main advantage is that the LIR technique is immune to excitation light intensity fluctuations and can be implemented with use of CW excitation instead of pulsed (or at least modulated) light sources needed for lifetime measurements [31]. Besides, the LIR technique reduces the complication of measuring the fluorescence signal, since it is only necessary to take the ratio between the intensity of two emission lines instead of register the time-resolved photodetector signal over the time as done in lifetime measurements.

Despite the apparent simplicity of implementing the LIR technique described in the paragraph above, there are some requirements regarding the experimental apparatus and the energy levels of the emitting atoms in a host matrix that need to be met [30, 32].

1. The experimental setup used to acquire the spectroscopic signals must possess enough resolution to distinguish the individual emission bands generated from the electronic transitions of the thermally coupled states to the ground state. In other words, the detection system must be capable of distinguishing the wavelengths of the investigated emission lines.

2. The energy gap between the thermally coupled levels must be larger than the thermal energy of the system $k_B T$ at 300 K $\sim$ 200 cm^{-1}. It means that at room temperature the high lying energy level has 40$\%$ of the total population which results in low LIR thermal sensitivity with temperature variations;

3. For measuring temperatures around 300 K, the energy gap between the thermally coupled levels must be smaller than $\sim$ 2000 cm^{-1}. This requirement needs to be met in order to have some thermal coupling between the to energy levels. Otherwise, the thermal population of the high energy state will be too small;

4. Both states must originate electronic transitions resulting in luminescence intensities strong enough to allow the detection of optical signal. However, one of the requirements to obtain systems capable of performing LIR nanothermometry with high thermal sensitivity is that the nonradiative transitions dominates over the radiative ones. Once the nonradiative processes dominates the excitation/emission dynamics of the transitions from the thermally coupled energy levels, the MP assisted processes have higher probabilities of contribute to the thermal population distribution between both energy levels.

Thus, by ensuring that the experimental setup and the investigated nanothermomters present the aforementioned conditions, the LIR method can be implemented to characterize the thermal response of luminescent nanothermometers and/or to investigate their fundamental physical properties.

The physical concepts presented so far are the basis for the implementation of LIR nanothermometry within a wide range of fluorescent materials. However, no example of the applications of LIR thermometry has yet been presented. Thus, the next subsection will present a few examples about the applications of LIR thermometry with different systems and what are the main advantages of working with lanthanide-based systems compared to other luminescent materials.

2.1.4 Applications of LIR thermometry with trivalent lanthanide ions

As mentioned in section 2.1.3, the LIR technique can be applied for performing high resolution thermometry in a broad variety of luminescent materials. Among them are fluorescent particles [33, 34], organic dyes [35, 36, 37], polymeric nanoparticles [38, 39], quantum dots [40, 41, 42] and lanthanide complexes [43, 44]. Some of those systems are at the cutting-edge of applied nanothermometry, allowing the investigation of thermal effects inside cell organelles with sub-micrometric precision [5]. For instance, thermosensors based on fluorescent particles named green fluorescent protein were used to visualize the thermogenesis in the mitochondria of brown adipocytes and endoplasmic reticulum of myotubes and to detect thermogenic heterogeneities inside HeLa cancer cells [33]. Similar experiments were carried with organic dyes [37]. Quantum dots, for example, have already been used to quantify temperature differences in neural cells which suggests that inhomogeneous heat production and dissipation may take place in brain tissue cells [40]. Despite the outstanding applications of these luminescent systems, some of them often present optical characteristics that limit their applicability.

Among the possible drawbacks found in LIR-based nanothermometers it is worth mentioning photobleaching and photoblinking which are common issues of organic dyes, polymeric particles and quantum dots under continuous exposure to excitation light [45]. These drawbacks, associated with the necessity of excitation light in the ultraviolet (UV) and visible regions of the spectrum often restricts the possibilities of thermal sensing on living tissue with quantum dots and fluorescent particles [33, 46]. When used in biological applications, the excitation with UV or visible light may cause the appearance of background fluorescence in addition to low tissue penetration and even damage of biological tissue [47].

Lanthanide complexes, on the other hand, are perhaps the most investigated systems for LIR-thermometry purposes. The reason for this select group of elements being widely applied for nanothermometry is their high photostability, high thermal sensitivity and minimally invasive thermal sensing properties due to low or almost null cytotoxicity of several Ln^{3+} -doped NCs [48]. The lanthanides are a special set of the periodic table of chemical elements which comprises 15 elements. The atomic numbers of this group ranges from $Z = 57$ (lanthanum) to $Z = 71$ (lutecium) and due to their distinctive physico-chemical properties, they have a particular position at the periodic table, as can be seen in the periodic table representation on Figure 3. Among these properties are the progressive filling of the $4f$ electronic shell and the shielding of the $4f$ electronic shell by the outer electronic shells $5s$, $5p$ and $6s$. This electrostatic shielding effect for the $4f$ orbitals makes the transitions between the $4f$ states very sharp, presenting atomic like spectroscopic characteristics [49]. Besides, the manifestation of inter-ionic ET, excited state absorption (ESA) and MP assisted processes allows one to observe energy UC on lanthanide-doped nanoparticles. In the energy UC, the fluorophore absorbs NIR photons and emit radiation at shorter wavelengths than the incident light, in the NIR or visible spectrum, *i.e.*, photons with high energy than the excitation ones [50]. LIR nanothermometers that present energy UC possess several advantages such as the negligible photodamage to living cells caused by the excitation light, weak autofluorescence background and deeper tissue penetration for biomedical thermometry purposes having also lower toxicity than other materials, as quantum dots [47].

Particularly, the closely lying states of the Ln^{3+} systems make it possible for different elements to present thermally coupled energy levels being, as said before, the main requisite for LIR-based thermometry. Besides, this proximity of the energy states also allows for luminescence detection from the UV to the near-infrared (NIR) spectroscopic range. These aspects can be better seen by looking at the Dieke's diagram of the lanthanides energy levels on Figure 4 [51]. Nanothermometers based on lanthanide complexes are mostly composed by solid dielectric NCs doped with a Ln^{3+} in its trivalent state. Nd^{3+} [52], Eu^{3+} [53], Er^{3+} [29], Tb^{3+} [54], Tm^{3+} [55], Ce^{3+} [56], are among the most common Ln^{3+} used for performing thermometry with NCs. For instance, LIR-based nanothermometry can be performed under NIR illumination with Nd^{3+}-doped Y_2O_3 upconverting NCs through the analysis of the luminescence intensities generated from the electronic transitions of the $^4F_{5/2}$ and $^4F_{7/2}$ levels to the ground state of Nd^{3+} which in turn exhibit emission lines at 820 nm and 750 nm, respectively [52]. For

Figure 3 – Representation of the periodic table o elements highlighting the family of Lanthanide elements.

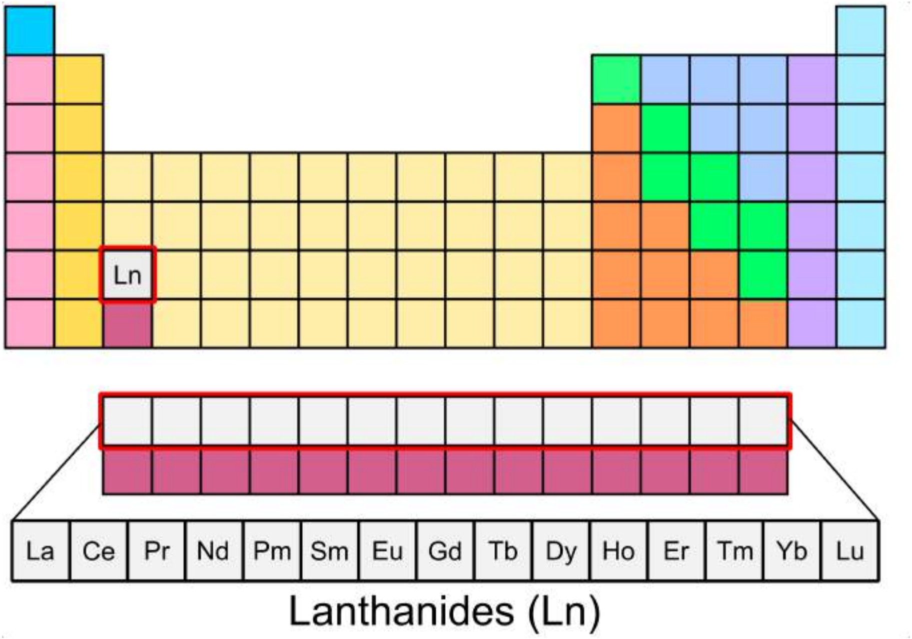

Font: The author (2022)

LIR measurements with upconverting Er^{3+} -doped systems, it is possible to investigate the detectable fluorescence generated from the radiative decay of the $^2H_{11/2}$ (526 nm) and $^4S_{3/2}$ (547 nm) states under $\sim$ 980 nm excitation [29]. Recently, high relative sensitivities (up to 4.92 % K^{-1}) were obtained with Tb^{3+}-doped Y_2O_3 and Lu_2O_3 nanocrystalline systems while investigating the luminescence generated from the $^5D_4 \rightarrow {}^7F_6$ electronic transition of Tb^{3+} at 540 nm [57].

Despite the notorious performance obtained with the implementation of LIR thermometry using NCs doped with a single Ln^{3+} element, it is also possible to perform LIR nanothermometry and achieve even high thermal sensitivities when working with NCs codoped with two or three different Ln^{3+} . These thermometric systems take advantage of inter-ionic energy transfer (ET) processes to maximize the efficiency of the energy UC in Ln^{3+} -doped NCs [50]. For codoped systems, there are countless combinations of Ln^{3+} that can be used as dopants for LIR-based thermometry. Some of the possible combinations that have been exploited are Yb^{3+}/Er^{3+}[24], Tb^{3+}/Eu^{3+} [58], Yb^{3+}/Nd^{3+} [59], Er^{3+}/Ho^{3+} [60], Cr^{3+}/Nd^{3+} [61], Yb^{3+}/Tm^{3+} [14], Yb^{3+}/Ho^{3+} *etc.*. Tri-doped systems can also be used for thermometric systems with high sensitivity. For instance, Mi *et al.* synthesized and implemented $NaFY_4$ NCs doped with Yb^{3+} ,Er^{3+} and Nd^{3+} as ratiometric nanothermometers under 980 nm excitation and obtained relative sensitivities up to 9.6 % K^{-1} at room temperature. In their work, the

Figure 4 – Energy levels of the lanthanide ions.

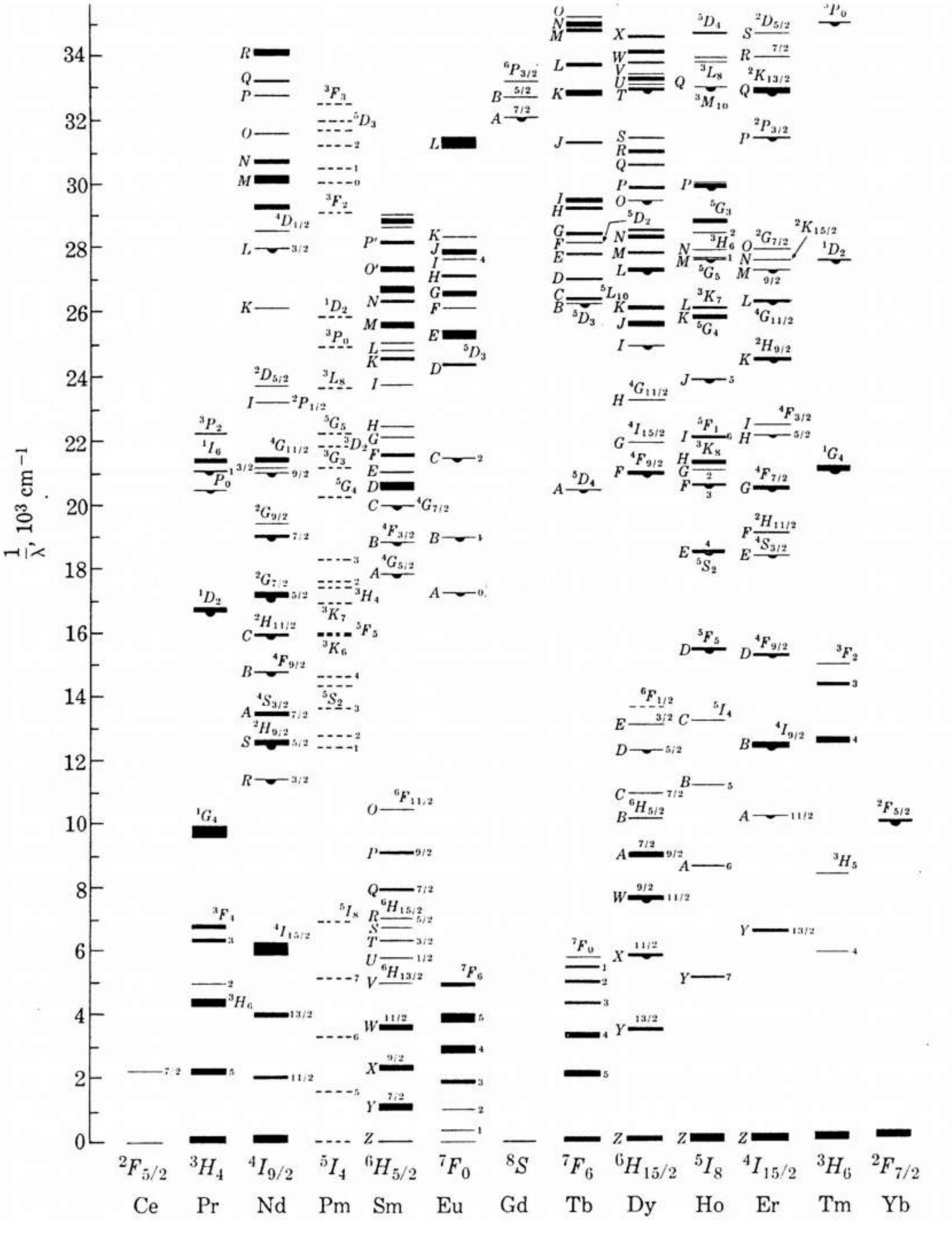

Font: Adapted from [51]

LIR measurements were performed with the ratio between the integrated emission bands originated from the radiative decay of the Nd^{3+} ($^4F_{3/2} \rightarrow$ $^4I_{9/2}$ at 803 nm) and Er^{3+} ($^4F_{9/2} \rightarrow$ $^4I_{15/2}$ at 654 nm) with the Yb^{3+} a sensitizer. The unbelievably high sensitivity obtained for this system is observed because the investigated transitions present opposite behaviors under temperature increase: the luminescence from the pair of Yb^{3+}/Nd^{3+} dopants, assisted by MP processes, increases when the temperature increases; in contrast, the UC emission from the pair of Yb^{3+}/Er^{3+} dopants, suffering from the thermal quenching effect, decreases due to the stronger multiphonon relaxation [9].

The main interest of this work is to study individual luminescent nanothermometers codoped with Yb^{3+}/Er^{3+}. The application of this particular combination of dopants for thermometry has been investigated for the last three decades [62] being until today a solid tool for nanothermometry applications. Zhu *et al.*, for example, combined UC Yb^{3+}/Er^{3+}-doped NCs, photothermal agents and anticancer drugs in a nanocomposite capable of performing simultaneous hyperthermia treatment and thermally activated drug delivery while monitoring the in situ temperature in mice cancer cells [63, 64]. Another example on the application of Yb^{3+}/Er^{3+}codoped systems was reported by Bastos *et al.*, in which codoped $LiYF_4$ NCs were used to determine the thermal properties of lipid bilayers through UC LIR nanothermometry [65].

UC LIR thermometry with $Yb^{3+}/Er^{3+}$is generally based on the luminescence generated from the radiative decay of the $^2H_{11/2}$ and $^4S_{3/2}$ energy levels, which generate emission bands around 528 nm and 559 nm under laser excitation light at 977 nm. The photophysics that explains the excitation mechanisms responsible for the visible luminescence in such systems are the ground state absorption (GSA), ET UC and ESA. The transitions mechanisms responsible for the detected luminescence of Yb^{3+}/Er^{3+}codoped systems are well established [66]. The excitation and emission dynamics are represented on Figure 5 and are described below. Out of the three aforementioned excitation processes, the ET upconversion dominates since the absorption cross-section of the Yb^{3+} at 977 nm is much larger than for Er^{3+} ions [46]. Once the codoped system is illuminated with 977 nm laser light, some of the Yb^{3+} ions are promoted to the state $^4F_{5/2}$ and subsequent nonradiative energy transfer from the Yb^{3+} to Er^{3+} may promote the Er^{3+} ions to the $^4I_{11/2}$ metastable state. Thus, a second nonradiative energy transfer from the Yb^{3+} can take place, promoting part of the Er^{3+} ions to the $^4F_{7/2}$ energy level. This process is known as a two-step one-photon absorption process [29]. Subsequent relaxation of the $^4F_{7/2}$ state can populate the $^2H_{11/2}$ (generating the emission band around 528 nm) and $^4S_{3/2}$ (emission band around 559 nm) via fast nonradiative decay. The states $^2H_{11/2}$ and $^4S_{3/2}$ are sufficiently close in energy to become thermally coupled and their populations follow a Boltzmann distribution (see subsection 2.1.1) [11]. Nonradiative decay from the $^4S_{3/2}$ state can populate the $^4F_{9/2}$ state, generating an emission band around 664 nm. The system can also decay nonradiatively from the $^4I_{11/2}$ state to the $^4I_{13/2}$ level and absorb a second quantum of energy and, promoting the Er^{3+} ion to a virtual state that decays instantly via multiphonon processes to the $^4F_{9/2}$ state. This is a second possibility of explaining the red emission generated by Er^{3+} -doped matrices. The thermally induced population redistribution between $^2H_{11/2}$ and $^4S_{3/2}$ should not be significantly affected by the Er^{3+} excitation pathway that involves the $^4I_{13/2}$ state and the red emission at 664 nm as long as the $^4F_{9/2}$ state is non-saturated [11].

Figure 5 – Energy level diagram for the Yb^{3+}/Er^{3+}codoped systems. The solid arrows indicate radiative absorption/emission processes; the gray dashed line represents ET between the Yb^{3+} and Er^{3+} ions; curly arrows indicate MP processes.

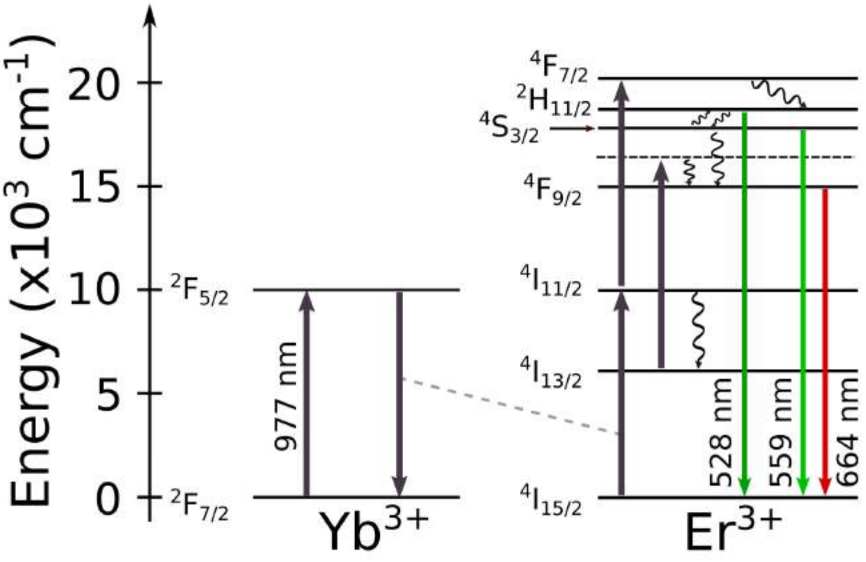

Font: Adapted from [11]

The photophysics of the Yb^{3+}/Er^{3+}codoped systems described in the previous paragraph helps us to understand the excitation mechanisms behind the common situation of studying the emission lines of the $^2H_{11/2}$ and $^4S_{3/2}$ energy levels to perform LIR-based thermometry under NIR excitation light. However, the literature on nanothermometry using Ln^{3+} -based materials often overlooks important deviations from the Boltzmann population distribution that are frequently present in experiments [27]. These deviations appear when thermometric experiments are performed with luminescent nanothermometers embedded in complex biological or liquid environments, as in the application scenarios mentioned in the last paragraphs [11]. Thus, in order to have a better understanding on the interaction between the LIR-based nanothermometers and the surrounding medium, the next subsection discuss some physical aspects that can generate thermal artifacts and temperature misreadings due to NC-solvent interaction in Ln^{3+} -doped systems.

2.1.5 NC-solvent interaction and its influence on LIR-based nanothermometers

Once we discussed how to perform temperature measurements through LIR technique followed by some examples of the applications of this technique with Ln^{3+}, we will now turn our attention to application scenarios in which the interaction of the nanometric thermometers with the surrounding medium are of fundamental importance. For instance, Xu *et al.* [67] applied the the LIR technique with Ln^{3+} doped energy UC nanothermometers to diagnose tissue inflammation in-vivo. Other studies used Ln^{3+} nanothermometers capable of detect temperature gradients during catalytic reactions [68, 69]. More specifically, Geitenbeek [69] investigated methanol-to-hydrocarbons catalytic reactions, with the need of having the nanothermometers embedded in methanol, without consider the possible effects of the NC-solvent interactions. In another study, Stripka *et al.* [27] measured concentration-dependent sensitivities for lanthanide nanothermometers suspended in a solution containing water and heavy water (D_2O). The authors proposed that the distinct sensitivities can be explained by the different energy mismatches between H-O and D-O bonds with respect to a radiative transition. Further experimental studies found in recent literature [70, 27, 11, 13] also show a solvent dependence on the physical properties of Ln^{3+} nanothermometers. This means that despite the inner radial distribution of the $4f$ shell favoring electrostatic shielding, the inter-band transitions are not completely isolated from the external media. This solvent dependence changes the emission dynamics of the excited energy levels in Ln^{3+} -doped NCs which in turn affects their thermal responsiveness in different media. Therefore, the investigation of emission properties in various environments must be performed to adequately understand the NC-solvent interactions.

The quenching mechanisms due to the solvent interactions with $\mathrm{Yb}^{3+}/\mathrm{Er}^{3+}$codoped β-NaYF_4 NCs were investigated by Rabouw *et al.* [13]. In their work, it is presented a microscopic quantitative model for the quenching dynamics of the in energy UC NCs in that will be taken as the main theoretical model for the discussion presented in this section.

The NC-solvent interaction can be interpreted as a form of Föster energy transfer [50], in which dipole-dipole coupling between the electronic transitions of the Ln^{3+} dopant to vibrations of the solvent and ligand molecules in contact with the surface of the NC. In this sense, the rate of ET by dipole-dipole coupling γ_{ET} depends on the inverse sixth power of the separation between the energy donor (the emitting Ln^{3+}) and the energy acceptor (the solvent vibration mode) being written as

$$\gamma_{ET}(\mathbf{r}_0,\mathbf{r}) = \frac{C}{|\mathbf{r}_0 - \mathbf{r}|^6}, \tag{2.8}$$

where $\mathbf{r}$ and $\mathbf{r}_0$ are the respective positions of the donor and the acceptor and C is the "energy-transfer strength" prefactor [71]. The value of the parameter C depends on the the oscillator strengths of the donor and acceptor transitions involved [72] as well as on the energy matching of the transitions in the Ln^{3+} to the vibrational energies of the solvent [73, 13, 74]. Thus, the total solvent quenching rate Γ_Q experienced by a luminescent center must depend on the dipole-dipole interactions with all solvent vibrations surrounding the NC. Thus, the quenching rate should depend on the diameter of the NC and on the location of the ion inside the NC. One can consider the NC as a sphere with an outer radius a_{out} and obtain a simple expression for Γ_Q by integrating the Equation 2.8 over all solvent molecules outside the NC [13]

$$\Gamma_Q(r_0,\rho C) = \int_{V_{out}} \gamma_{ET}(\mathbf{r}_0,\mathbf{r})\rho d\mathbf{r} = \frac{4\pi\rho C a_{out}^3}{3(a_{out}^2 - r_0^2)^3}, \tag{2.9}$$

where V_{out} is the volume occupied by the solvent, $r_0 = |\mathbf{r}_0|$ is the radial position of the emitting center and ρ is the density of solvent vibration modes involved in the quenching. As one would expect (see Equation 2.9 above), the quenching effect depends on the geometric shape of the NC and on the product between the vibrational density of states and the energy-transfer parameter, ρC, which is called the "quenching density" of the interaction; with units of volume *per* time and describes the interaction of the emitters with the solvent. In order to avoid the infinite Γ_Q at the surface of the NC ($a_{out} = r_0$ in Equation 2.9), it can be considered a thin layer (say 0.3 nm) between the physical outer radius and the solvent. Such spacing is on the order of a single atomic layer and its existence is confirmed by electron microscopy [13]. This thin layer can be related to the presence of other species such as fluoride anions (for β-NaYF$_4$ doped NCs), headgroups of the ligands (carboxylate head groups of oleates), etc., which contribute significantly less to the vibrational quenching than the solvent does. Figure 6 shows the normalized $\Gamma_Q\ /\rho C$ (Equation 2.9) as a function of the ion-solvent distance r_0 for a 70 nm sized NC. It can be noticed that the energy transfer rate differs by orders of magnitude between the ions at the center of the NC and those located close to the surface of the NC [13]. This model can predict the spatial distribution of the quenching rates for any spherical NC geometry if the quenching density ρC of a particular solvent to a particular dopant is known.

Figure 6 – Normalized total rate $\Gamma_Q/\rho C$ of solvent quenching by dipole-dipole interaction. It can be noticed that the total rate strongly depends on the radial position of the lanthanide ion in the NC, plotted here for a NC with 70 nm radius.

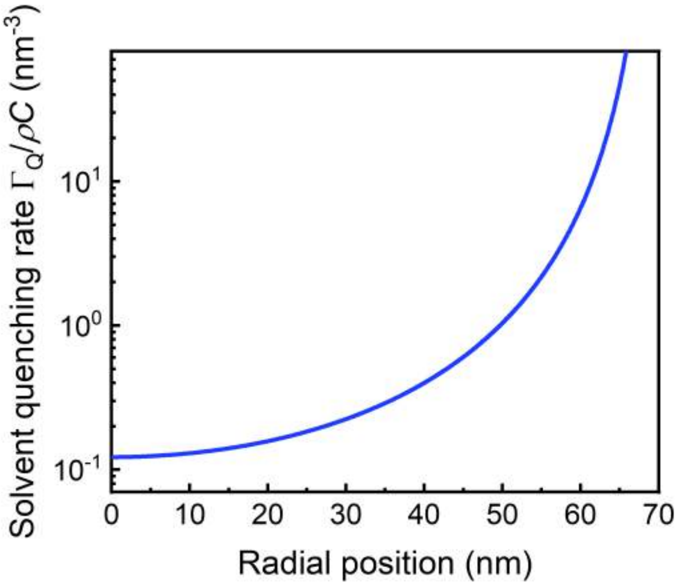

Font: Adapted from [13]

Besides the nonradiative ET between the emitting ions and the solvent vibrational modes presented in the last paragraph, the radiative quenching due to the solvent's refractive index may also affects the dynamics of Ln^{3+} -doped NCs. The radiative decay rate Γ_R of dopant centers in NCs can be written as [70]

$$\Gamma_R(n) = \frac{\Gamma_R^0}{n}\left[\frac{3n^2}{2n^2 + n_{NC}^2}\right]^2, \tag{2.10}$$

where n is the refractive index of the solvent, Γ_0 is the radiative decay rate of the emitters in a bulk sample, and n_{NC} is the refractive index of the NC material. As can be noticed from Equation 2.10, the effect of the refractive index of the solvent on all the ions is the same for all ionic centers independent of their location inside the NC - if the NC is (quasi-)spherical and much smaller than the emission wavelength [70]. Thus, the total decay rate Γ_T due to the interaction of the emitting centers and the solvent can be given as the sum of Γ_Q and Γ_R as

$$\Gamma_T = \Gamma_R(n) + \Gamma_Q(r_0, \rho C), \tag{2.11}$$

in which the radiative decay rate Γ_R explicitly depends on the solvent refractive index n and the nonradiative quenching rate Γ_Q depends on the the radial coordinate of the emitting ion in the NC r_0 and on the quenching density ρC of the solvent.

Some experimental results corroborate the quenching mechanism described in the previous paragraphs. For instance, Rabouw *et al.* performed experimental studies with codoped NaYF$_4$:Yb^{3+}/Er^{3+}NCs. They measured the nonradiative quenching effects of the ^{4}F$_{9/2}$ $\rightarrow ^4$I$_{15/2}$ and ^{4}S$_{3/2}$ $\rightarrow ^4$I$_{15/2}$ transitions of Er^{3+} in various solvents: hexane, octane, cyclohexane, chloroform, toluene, chlorobenzene, and o-dichlorobenzene. Their results show that for both transitions and for all solvents there is an increase in the decay rates of the NCs if compared with bulk samples, which confirms the existence of quenching pathways in the codoped NCs. The ET to the solvent is present for the two transitions. Indeed, the two investigated energy levels of the Er^{3+} (^{4}F$_{9/2}$ and ^{4}S$_{3/2}$) are apart from the next lower level by approximately 3000 cm^{-1}, which can bridged by coupling to vibrations in organic molecules, such as the C - H stretching vibration mode [13]. The ET between the emitting Er^{3+} and the solvent is represented in Figure 7 below. The vibrational levels of the solvent molecule is given by v $= i$, where $i = 0, 1$ are the ground and excited vibrational states, respectively.

Figure 7 – Schematic representation of the NC-solvent quenching effects for the ^{4}F$_{9/2}$ and ^{4}S$_{3/2}$ emitting states of Er^{3+} . Here, the population dynamics of the two states can be changed due to the presence of vibrational modes of the solvent almost resonant with the energy differences between the excited states and the low-lying energy levels. The gray dashed line represents the ET process between the Er^{3+} and the solvent.

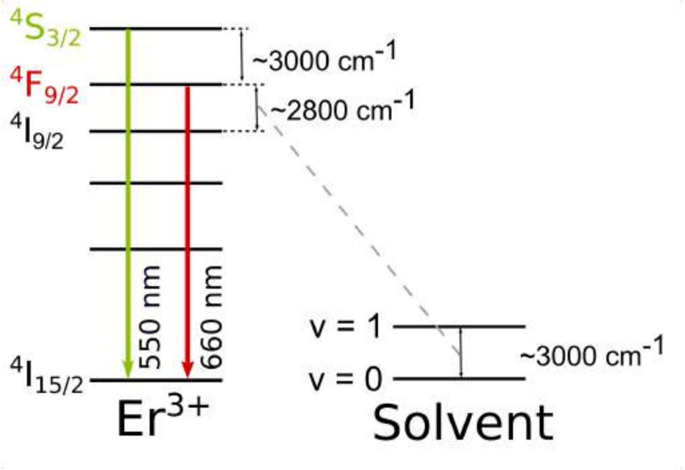

Font: The author (2022)

In another study, Skripka and collaborators reported experimental LIR results on the IR transitions of core-shell tri-doped NCs and their results show that IR ^{4}I$_{11/2}$ $\rightarrow ^4$I$_{13/2}$ transition of the Er^{3+} ions is strongly affected by the nonradiative quenching due to the water surrounding medium. Since the LIR technique is based on the ratio between the intensities of two thermally coupled emission lines, this change in the population dynamics due to the solvent results in different measured relative sensitivities in distinct environments. Indeed, the $^4\text{I}_{11/2} \rightarrow ^4\text{I}_{13/2}$ transition is resonant with the stretching O - H modes of water molecules (3400 - 3500 cm^{-1}) which may bridge the energy gap between the two levels by coupling to the vibrational modes. This assumption is confirmed in their work by the study of the thermal response of the same synthesized particles in D_2O for which this effect is reduced due to the mismatch between the H - O and the D - O vibrational modes of water and the deutered water, respectively. These results are a strong evidence that the performance of the LIR-based nanothermometers can be environment dependent [27].

The digression on LIR-based thermometry in this section is necessary to present the experimental results and the discussions contained in chapter 3, which presents the experimental studies performed on the influence of the surrounding medium on the thermal properties of single luminescent NCs codoped with $\text{Yb}^{3+}/\text{Er}^{3+}$.

Before jumping to the experimental investigations, we need to introduce the second luminescence-based thermometric technique used in this thesis to perform nanothermometry with single nitrogen-vacancy defects in individual nanodiamonds. We shall start by presenting the physical properties of the nitrogen-vacancy defects on diamonds along with the main characteristics presented by the defects that allows the implementation of these emitters as luminescent nanothermometers.

2.2 ODMR-BASED THERMOMETRY WITH NITROGEN-VACANCY DEFECTS

Previously, in section 2.1, the principles of LIR-based nanothermometry were introduced along with a brief discussion about the applications of this technique with lanthanide complexes compared to other luminescent materials as quantum dots, organic dyes and polymeric nanoparticles. This section, in turn, is focused on the description of the physical mechanisms that allow one to perform nanothermometry through optically detected magnetic resonance (ODMR) with nitrogen-vacancy defects in diamond. Unlike the LIR technique presented in section 2.1 that can be applied in a wide range of optical materials, ODMR-based nanothermometry is, to the best of our knowledge, a thermal sensing technique only possible to be performed with nitrogen-vacancy defects on a diamond host because of the unique temperature dependent physical properties of these defects. Therefore, this section will bring an introduction about the aspects of the color centers found on nanodiamonds, highlighting of course the nitrogen-vacancy centers; the singular photophysical properties of these defects and what are the temperature-dependent effects that can be optically detected in order to perform luminescence nanothermometry with these fluorophores.

2.2.1 Color centers and nitrogen-vacancy defects in diamond

Diamond has been object of desire for long time not only by the inherent beauty of this marvelous mineral, but also by its applicability on industry and medicine due to its particular physical characteristics. The industry takes advantage of many of those properties, such as mechanical hardness, heat conductivity, optical transparency and chemical inactivity for most acid and bases [75, 76]. The wide optical bandgap of diamond (5.5 eV, corresponding to the violet region of the spectrum) makes it transparent for most of the wavelengths, including visible light [77]. This physical feature gives the ultra-pure diamonds their typical colorless appearance, with refractive index of $n = 2.4$ for visible light [78]. However, diamonds can also be found in a variety of colors due to the presence of impurities which can cause significant changes in the physical properties of pristine diamonds [79, 80]. The presence of defects in the diamond host matrix is responsible for the creation of donor (or acceptor) levels within the diamond bandgap, that can trap an electron (or a hole) nearby this defect (Figure 8a). Thus, as observed in quantum confinement for semiconductor doped matrices, the trapping of an electron leads to the generation of an optically active energy level structure [78]. These luminescent structural defects are commonly called "color centers". Up to these days, over a 100 optically active defect types were identified in diamonds [79]. For instance, boron impurities make diamonds have a blue tonality; nitrogen defects, which are the more abundant color centers found in nature, give the diamond a yellow coloration; green diamonds can exist due to the presence of electronic holes in the diamond host; in a particular case, when there is an association of nitrogen defects and the absence of a carbon atom in the diamond lattice, named a NV defect, diamond tends to present a rosy aspect [78, 79].

Some color centers in diamond have attracted attention due to the quantum nature found in the dynamics governing their optical electronic transitions. Associated with it, the high photostability of luminescent defects makes the color centers in diamond excellent candidates for applications in solid-state quantum technologies [83, 80]. Among all the color centers, the NV defect is one of the most studied in the recent years because of all the aforementioned qualities and its applications in quantum information [79, 80], quantum thermodynamics [84], biology [85], and high resolution sensing for magnetometry [86, 87], electrometry [88, 89], and

Figure 8 – a) The presence of defects in the diamond host matrix may lead to the creation of donor (acceptor) energy levels (dashed lines) within the wide bandgap of diamond due to the association of electrons (holes) and impurity centers. The energy of the donor, E_D (acceptor, E_A), and diamond energy gap, E_G are given by solid arrows. b) Colored diamonds containing electronic holes (green), boron (blue), NV color centers (rose) and nitrogen (yellow). c) Schematic representation of the NV defect on a diamond lattice.

Font: a) Adapted from [78]. b) Image available at [81]. c) Adapted from [82]

thermometry [90, 91].

Nitrogen is by far the most studied color center in diamond and is naturally found as a substitutional atom within the crystalline matrix [83]. The NV defect, in turn, can either be found in synthesized and natural diamonds. As mentioned before, this luminescent defect happens due to the association of a substitutional atom of nitrogen and a vacancy in its immediate neighborhood [Figure 8c)] and there are a few fabrication methods used to synthesize diamonds with NV defects. The most common techniques are High Pressure High Temperature (HPHT) [92] and Chemical Vapor Deposition (CVD) [93]. Besides these methods, the defects can be produced by irradiation and annealing of natural nitrogen-doped diamonds. It is possible because vacancies can be produced inside a diamond host by irradiating the crystal with an electron beam with energies ranging from keV to MeV. These vacancies can then diffuse inside the diamond lattice as a result of an annealing treatment at high temperatures. Thus, if the irradiated matrix possesses nitrogen centers, the annealing treatment can take the vacancies towards a lattice site adjacent to the existent nitrogen defects, generating NV color centers [83, 94]. The next subsections will bring discussions on the electronic structure, the photophysical properties of the NV defects and the principles of ODMR.

2.2.2 Electronic structure and charge states of the NV defect

The molecular arrangement that defines the NV center is composed by the nitrogen atom, the vacancy, and the carbon atoms surrounding the vacancy. The structure of the center displays C_{3v} symmetry, which means that the defect is invariant under rotations of 120° relative to the its symmetry axis. The NV center is represented on Figure 9a) and the symmetry axis is the line connecting the vacancy and the nitrogen atom (z axis on inset).

The NV center is commonly found in two charge states, the neutral (NV^0) and the negatively charged nitrogen-vacancy (NV$^-$) defect. The NV^0 configuration is the basic electronic state of the NV defects in which five electrons occupy the dangling bonds of the nitrogen and carbon atoms surrounding the vacancy [95]. The nitrogen atom adjacent to the vacancy site can also accept an extra electron from the crystal lattice, giving rise to the NV$^-$ defect. The six-electron configuration has been accepted since its proposal [96, 97] and successfully explains the optical and spin properties of the NV$^-$ center. NV defects in this last charge state are the main subject of this and the next chapter.

In order to describe the electronic structure of the NV$^-$ defect it is necessary to use the theoretical formalism of group theory [98]. This treatment allows one to use symmetry properties in order to construct a set of molecular orbitals describing the electronic occupation states of the NV$^-$ center, which can be written as $\{a_1, a_1', e_x, e_y\}$ [83, 99]. In its ground state, represented in Figure 9b), the NV$^-$ defect has the molecular orbitals a_1 and a_1' completely filled with two electrons each, and both the $e_{x,y}$ orbitals are occupied by one electron according to the Aufbau principle [99, 98]. The electronic configuration of atoms in the ground state is commonly represented by $a_1^{2\prime}a_1^2e^2$, where the superscripts represent the number of occupying electrons in each molecular orbital. In the group theory formalism, the ground state correspond to a $^3A_2$ state due to its electronic configuration [96]. When sufficient energy is given to promote the NV$^-$ defect to its excited state, Figure 9c), one electron of the a_1 state is excited to either e_x or e_y orbitals, assuming a configuration represented by $a_1^{2\prime}a_1^1e^3$, corresponding to a ^3E state in group theory formalism [99, 100, 98]. In both excited and ground states, the total spin angular momentum is $S = 1$ and the energy levels for both states are defined by spin triplets. The consequences of the electronic distribution in the spin properties and energy levels for optical activated NV$^-$ defects will be discussed in the next subsection.

Figure 9 – a) Schematic representation of the NV defect in diamond. The vacancy (gray shaded region) is connected with the nitrogen (orange sphere) and the carbon atoms (gray spheres) by dangling bonds (blue shaded areas). The center has C_{3v} symmetry and is invariant under 120° rotations relative to the symmetry axis of the center (z axis). Electronic spin occupation in a six electron scheme for the a) ground and b) excited states of the nitrogen vacancy center.

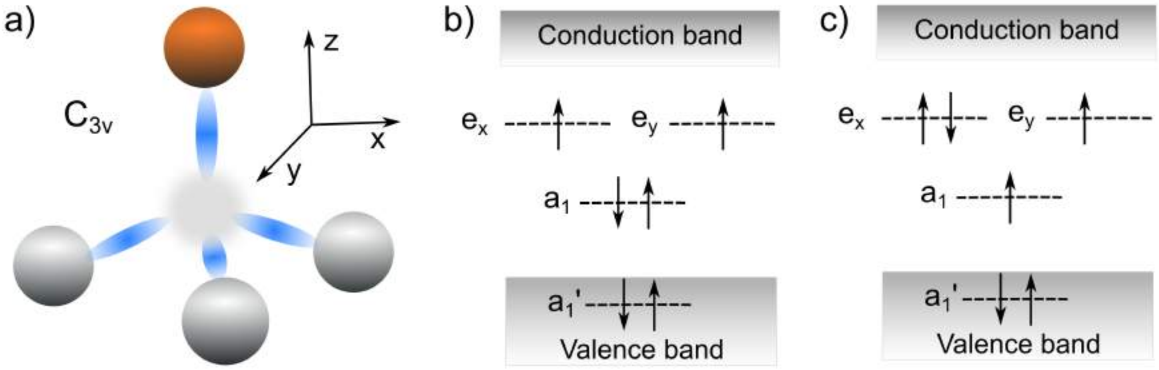

Font: a) Adapted from [83]

2.2.3 Energy levels and spin properties of NV$^-$ defects

The utilization of single NV$^-$ defects as sensing devices is only possible by virtue of their distinct spin angular momentum properties which defines the energy levels of the color centers. As mentioned in subsection 2.2.2, the existence of two unpaired electrons out of the six electrons trapped on the vacancy leads to a total spin of $S = 1$. This spin configuration allows the formation of spin triplets in the ground $|g\rangle$ ($^3A_2$) and first excited $|e\rangle$ (^3E) electronic states [79]. Optical excitation of the NV$^-$ defects typically performed with green light originates electronic transitions that, at room temperature, lead to a broad vibronic photoluminescence spectrum ranging from 600 to 800 nm with a zero phonon line (ZPL) at 637 nm (1.95 eV) [101], as shown in Figure 10. In the absence of any perturbative field, both ground and excited states of the NV$^-$ are spin triplets presenting spin projections along the defect symmetry axis of $m = 0$ for the lower spin state and $m = \pm 1$ as a degenerate doublet state. The energy separation between the lower and upper spin sublevels for the ground state is predominantly caused by spin-orbit interactions resulting in a zero field splitting $\mathcal{D}_{gs} \approx$ 2.87 GHz. The splitting is present in the first excited state, but with a zero field splitting of $\mathcal{D}_{es} \approx$ 1.42 GHz [102].

The photophysics of a single NV$^-$ defect can be discussed when the color center is illuminated with linearly polarized CW laser light, resulting in spin-conserving optical transitions between the ground and excited states of the defect. It means that the optical transitions are subjected to the spin angular momentum conserving selection rules which states that the

Figure 10 – Luminescence spectrum of a single NV^{-} center with a characteristic zero phonon line at 637 nm (red arrow), taken at room temperature under the excitation of a CW laser emitting at 532 nm.

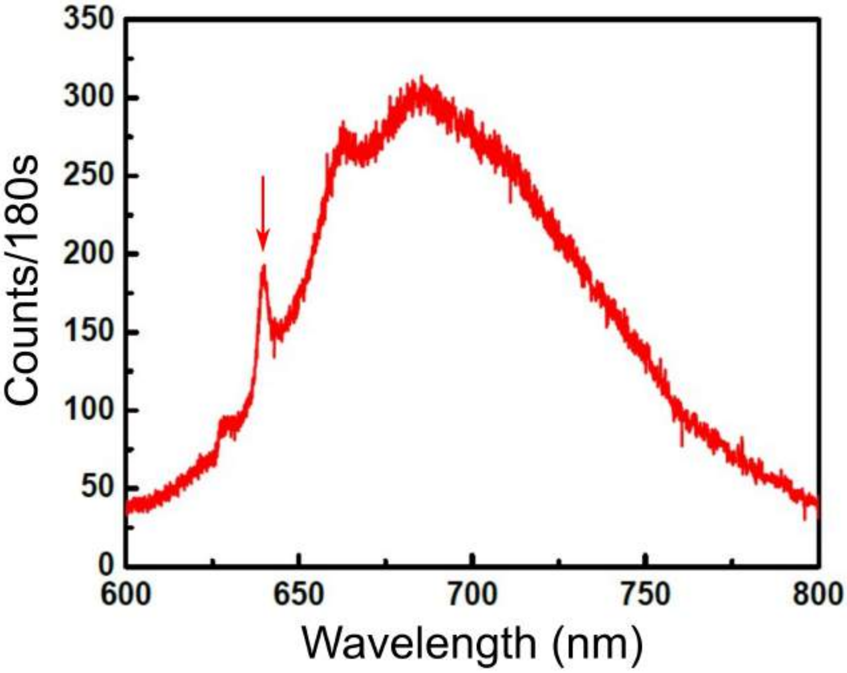

Font: Adapted from [83]

electronic transitions between the ground and excited states can only occur when $\Delta m = m_{gs} - m_{es} = 0$, where m_{gs} and m_{es} are the spin sublevels of the ground and excited states, respectively. These electronic transitions are schematically shown in Figure 11a). The transition from $m_{gs} = 0 \ \rightarrow \ m_{es} = 0$ results in a predominantly radiative decay, indicated by the red thick arrow on Figure 11, with small probability (thin gray dashed arrow) of nonradiative decay via intersystem crossing (ISC) and returning to the $m_{gs} = 0$ spin sublevel. Meanwhile, for the electronic transitions between the $m_{gs} = \pm 1$ to the excited $m_{es} = \pm 1$ the system has a higher probability of nonradiatively decaying (thick gray dashed arrow) crossing to the metastable singlet state and then to the $m_{gs} = 0$ of the ground state [83]. This increased nonradiative decay via ISC is from the $m_{es} = \pm 1$ sublevels is mainly due to transverse spin-orbit interactions, resulting in highly state-selective ISC transitions [103].

The decay dynamics of the excited state with $m_{gs} = \pm 1$ is very useful for two reasons. First, even if the system has its initial state at the $m_{gs} = \pm 1$, after a few optical cycles the system returns to the ground state with spin projection $m_{gs} = 0$. It means that the NV^{-} can be spin polarized by optical pumping, allowing one to prepare it in an initialized known state [104]. The second reason is that the luminescence emission rate depends on the spin state

Figure 11 – a) Schematic of the energy level structure of the NV$^-$ defect, presenting the dynamics of the system in the process of optical excitation (green arrow) and fluorescence emission (red arrows). The numbers indicate the spin z-projection $m = 0, \pm 1$. Transitions between ground and excited states are spin conserving. Decay through ISC (gray dashed arrows) results in the spin polarization with high probability to achieve a switch from $m_g = \pm 1$ to $m_g = 0$ by means of nonradiative decay processes. b) Normalized ODMR simulated spectrum obtained in the absence of any field, indicating a dip centered on a resonance frequency of 2.87 MHz. c) Normalized ODMR simulated spectrum obtained for a NV$^-$ defect in the presence of intrinsic strain and piezoelectricity of the diamond host matrix. In the absence of any external fields, two ESR frequencies ν_- and ν_+ are apart by $2\Delta = 2\mathcal{E}$ and $\mathcal{D}_{gs}$ is the average of the two resonance frequencies.

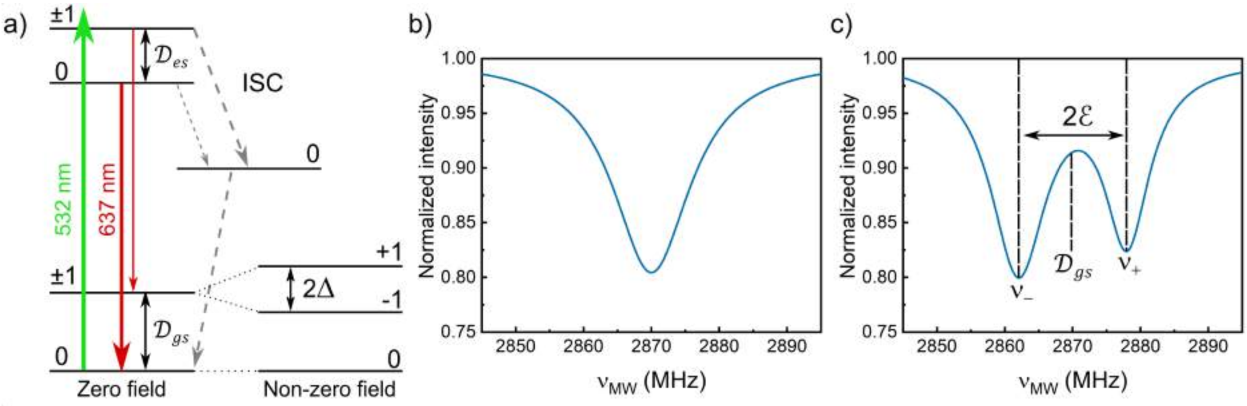

Font: a) the author (2022). b) and c) adapted from [83]

of the NV$^-$ defect which leads to the possibility of performing ESR frequency measurements by detection of optical signal. In a typical experimental situation, the ESR measurements are performed by tuning a microwave field close to the ESR frequencies of NV$^-$ defects, while monitoring the emitted luminescence of the color centers. By sweeping the frequency of microwave pulses and synchronously detecting the defect's emission, it is possible to promote the transition from $m_{gs} = 0$ to the $m_{gs} = \pm 1$ and due to the ISC nonradiative deactivation path described above, it causes a decrease in fluorescence by $\sim$20$\%$ when the frequency of the microwave field matches the spin resonances, as is schematically shown in Figure 11b). This experimental principle is the basis of the so-called Optically Detected Magnetic Resonance technique that allows one to perform thermometry with the NV$^-$ defects. The experimental setup assembled for performing the ODMR sensing with single NV$^-$ defects will be described in Chapter 4 along with the application of this technique on thermometry measurements.

In the presence of non-zero fields, as shown in Figure 11a), the degenerate states with $m = \pm 1$ undergo an axial symmetry break, leading to a splitting of the $m_{gs} = -1$ and $m_{gs} = +1$ spin sublevels. This lift in degeneracy, corresponding to a splitting parameter Δ, can be caused by inherent strain of the diamond lattice and diamond's piezoelectricity [98], Zeeman effect due to external magnetic fields [86] and Stark effect caused by the interaction of the NV$^-$ center and electric fields [105]. In these cases of symmetry breaking, the resonance frequencies ν_- and ν_+ correspondent to the sublevels $m_{gs} = -1$ and $m_{gs} = +1$, respectively, can be detected with the same optically detected ESR principles described in the last paragraph. Figure 11c) depicts a typical ESR signal in the absence of external fields obtained for a NV$^-$ defect for nondegenerate $m_{gs} = -1$ and $m_{gs} = +1$ spin sublevels, whose frequencies are apart $2\Delta = 2\mathcal{E}$ from each other. In this case, as discussed in the subsection 2.2.4, the splitting parameter Δ is solely determined by the local strain and piezoelectricity of the diamond matrix, being defined as the strain parameter $\mathcal{E}$, which is a common situation when dealing with single nanodiamonds [87].

The last paragraphs presented a description of the photophysical properties of the NV$^-$ defect that allow one to manipulate and optically detect the spin state of a color center. However, one of the main goals of this work is to perform real-time thermometric measurements with the NV$^-$ defects. Thus, it is necessary to explain how temperature-dependent phenomena can modify the energy states of these centers and what are the measurable physical parameters that can be used to determine the temperature of a system by using single NV$^-$ defects on nanodiamonds as thermal nanoprobes, which is done it what follows.

2.2.4 Temperature dependence of the NV$^-$ ESR frequencies

The experimental technique applied in this work in order to determine the temperature of a given sample by using a single NV$^-$ defect in a nanodiamond host is based on the temperature-dependence of the ESR frequencies of the NV$^-$ ground state. These thermal effects are mediated by a combination of lattice thermal expansion and electron-phonon interactions and are discussed in more detail in the following paragraphs.

The manifestation of thermal effects on the ground state of the NV$^-$ defects can be better understood by studying its Hamiltonian. The spin-spin interaction between the two unpaired electrons involved by the NV$^-$ gives rise to an energy separation between the $m_{gs} = 0$ and $m_{gs} = \pm 1$ sublevels, known as zero field splitting (ZFS) written as $\mathbf{S} \cdot \mathcal{D} \cdot \mathbf{S}$ [106], where $\mathbf{S}$ is the spin operator and $\mathcal{D}$ is the tensor that describes the dipolar interaction. By considering the contribution of intrinsic strain of the diamond matrix, the spin Hamiltonian for the ground state of the NV$^-$ defect can be written as [83]

$$H_{ZFS} = h\mathcal{D}_{gs}S_z^2 + h\mathcal{E}(S_x^2 - S_y^2), \tag{2.12}$$

where $\mathcal{D}_{gs}$ and $\mathcal{E}$ are the ZFS and the strain parameters [see Figure 11c)], respectively; S_x, S_y and S_z are the Pauli matrices for $S = 1$ spin operators and the z coordinate coincides with the C_{3v} symmetry axis. In this Hamiltonian, $\mathcal{D}_{gs}$ is the largest energy scale and is given by the energy that separates the spin sublevels $m_{gs} = 0$ from $m_{gs} = \pm 1$ with value of $\mathcal{D}_{gs} = 2.87$ GHz at room temperature.

When the NV$^-$ defect is in the presence of an external magnetic field, there is the manifestation of the Zeeman effect which induces energy changes on the $m_{gs} = \pm 1$ sublevels. The Zeeman splitting is proportional to the magnitude of the applied external field. It means that by increasing the magnitude of the applied magnetic field the splitting between the spin sublevels increases as well. Thus, another term needs to be added to the Hamiltonian given in equation 2.12 in order to account for the interaction of the NV$^-$ with the external magnetic field. The Hamiltonian term due to the Zeeman effect H_Z can be written as [107]

$$H_Z = g\mu_B \mathbf{B} \cdot \mathbf{S}, \tag{2.13}$$

where $\mathbf{B}$ is the external magnetic field; $g \simeq 2$ is the Landé factor; μ_B is the Bohr magneton. Thus, disregarding the hyperfine interaction, we can write the total Hamiltonian with the use of Equations 2.12 and 2.13 as

$$H = H_{ZFS} + H_Z \ , \tag{2.14}$$

$$H = h\mathcal{D}_{gs} S_z^2 + h\mathcal{E}(S_x^2 - S_y^2) + g\mu_B \mathbf{B} \cdot \mathbf{S}. \tag{2.15}$$

The Hamiltonian in Equation 2.15 is sufficient to understand the relevant points of the temperature-dependent spin dynamics of the NV$^-$-doped nanodiamonds. One should notice that early studies by the time of the first identification of the NV$^-$ defects had already identified temperature dependent effects. Davies [108] proposed an accurate vibronic model that explains the observation of changes in the ZPL energy accompanied by changes in its homogeneous linewidth and luminescence intensity. Later, the Davies model of the temperature shift of the visible ZPL was generalized by Doherty *et al.* [109] for the temperature dependence of $\mathcal{D}_{gs}$. The generalization for $\mathcal{D}_{gs}$ follows from the recognition that the spin transitions of the ground state spin resonance are zero-phonon transitions, *i.e.*, the observed spin resonance is in itself a ZPL.

In Davies' model, there are two contributions responsible for the temperature shifts of the spin resonances: (1) the spin energies are perturbed by strain of thermal expansion, and (2) the vibrational frequencies associated with different spin states differ. The latter is a consequence of quadratic electron-phonon interactions.

Regarding the role of strain, since thermal expansion is closely related to the hydrostatic pressure, the contribution of thermal expansion to the ground state spin resonances can be simply expressed as [109, 110]

$$\Delta\mathcal{D}_{gs}^{ex}(T) = \epsilon_{gs}\ P(T), \tag{2.16}$$

where $\epsilon_{gs} = 14.58$ MHz/GPa [111] is the hydrostatic pressure shift of $\mathcal{D}_{gs}$ and $P(T)$ is the pressure due to thermal expansion given by

$$P(T) = \mathcal{B}\int_0^T e(T')dT', \tag{2.17}$$

where $\mathcal{B} = 442$ GPa is the bulk modulus of diamond and $e(T)$ is the diamond volume expansion coefficient as a function of temperature.

If the vibrational frequencies associated with different electronic levels differ, the energy of a zero-phonon transition will depend linearly on vibrational quantum number. We can now introduce the vibrational density of modes $\rho(\omega)$ and performing the thermal average, the contribution of electron-phonon interactions to the $\mathcal{D}_{gs}$ temperature shift is written as

$$\Delta\mathcal{D}_{gs}^{e-p}(T) = \int_0^\Omega n(\omega,T)\delta_{gs}(\omega)\rho(\omega)d\omega, \tag{2.18}$$

where $n(\omega,T) = (e^{\hbar\omega/k_BT} - 1)^{-1}$ is the Bose-Einstein distribution of vibrational occupations; $\Omega \sim 165$ meV is the highest vibrational frequency of diamond and $\delta_{gs}(\omega)$ is the average vibrational frequency difference between the electronic states [109]. Thus, it is possible to write down an expression for the dependence for $\Delta\mathcal{D}_{gs}(T)$ given by the two contributions described on Equations 2.16 and 2.18 as

$$\Delta\mathcal{D}_{gs}(T) = \Delta\mathcal{D}_{gs}^{ex}(T) + \Delta\mathcal{D}_{gs}^{e-p}(T), \tag{2.19}$$

which results in

$$\Delta\mathcal{D}_{gs}(T) = \epsilon_{gs}\ \mathcal{B}\int_0^T e(T')dT' + \int_0^\Omega n(\omega,T)\delta_{gs}(\omega)\rho(\omega)d\omega\ . \tag{2.20}$$

According to Doherty *et al.* [109], given the power series expansion of $e(T)$ and $\delta_{gs}(\omega)\rho(\omega)$, the temperature shift $\Delta\mathcal{D}_{gs}(T)$ can be expressed by a polynomial in the temperature T. For instance, experimental studies with NV$^-$ ensembles in bulk samples reported an adequate fit with a polynomial terminating at T^5 for a temperature range of 5 K to 300 K [109]. Another study with individual nanodiamonds obtained a good experimental fit by using a quadratic polynomial expression for $\Delta\mathcal{D}_{gs}(T)$ for temperature values ranging from 300 K to 500 K [110]. The difference between the data analysis proposed in the two studies can be explained either by the high temperature range and the use of individual nanodiamonds on the second work. An explicit indicator of it is the fact that the contributions of $\Delta\mathcal{D}_{es}^{e-p}(T)$ begins with powers of T^3 because as $\omega \rightarrow 0$ the Debye density, *i.e*, $\rho(\omega)$ is proportional to ω^2 and for quadratic electron-phonon interactions $\delta_{gs}(\omega) \propto \omega$. Thus, for high temperatures, the contribution of $\Delta\mathcal{D}_{gs}^{ex}(T)$ to the lower powers of T on $\Delta\mathcal{D}_{gs}(T)$ tends to be accentuated [110]. Besides, the bulk modulus of nanodiamonds can be as high as 560 GPa [112] which would increase the contribution of $\Delta\mathcal{D}_{gs}^{ex}(T)$ due to thermal expansion (see Equation 2.16). For intervals in the biological temperature range (305 to 320 K) the experimental measurements of $\Delta\mathcal{D}_{gs}(T)$ can be adjusted with a linear function of T, as reported by [113].

As mentioned before, one of the focus of this work is to perform temperature measurements with NV$^-$ defects in temperature intervals compatible to biological systems. Thus, according to the studies carried on by Fujiwara *et al.* [113] a linear fit of the experimental measured resonance frequencies ν_- or ν_+ for the spin sublevels as function of temperature returns the same information as measuring $\Delta\mathcal{D}_{gs}(T)$, being suitable to analyze the acquired data. The reason to work with the spin resonances instead of the ZPS, given by $\mathcal{D}_{gs}$, is that the strain parameter for the ground state do not present detectable variations up to 600 K [110]. It means that measuring the frequency shifts of a given resonance due to temperature variation, say $\nu_-(T)$, will return the same information of measuring the shift of $\Delta\mathcal{D}_{gs}(T)$. An example is shown in Figure 12 in the absence (a) and in the presence (b) of an external magnetic field. It can be noticed from the figure that the thermal shifts on the spin resonances $\Delta\nu_\pm(T)$ are equal in frequency to $\Delta\mathcal{D}_{gs}(T)$. Thus, either $\Delta\mathcal{D}_{gs}(T)$ or $\Delta\nu_\pm(T)$ can be used as thermal parameters in order to perform the temperature sensing of a sample with the single NV$^-$ defects. An experimental advantage of this technique in the presence of an external magnetic field is the capability to perform the real-time monitoring of the ESR frequency of a given spin sublevel, which allows one to obtain the real-time temperature of the sample, as will be shown in the the experimental results reported on Chapter 4.

Figure 12 – Normalized ODMR simulated spectrum in the a) absence and in the b) presence of an external magnetic field. The blue and red lines represent simulated spectra at low and high temperatures, respectively. The thermal shifts induced in $\mathcal{D}_{gs}$ and $\Delta\nu_{\pm}$ are equal in frequency, being equivalent for the determination of temperature from these parameters.

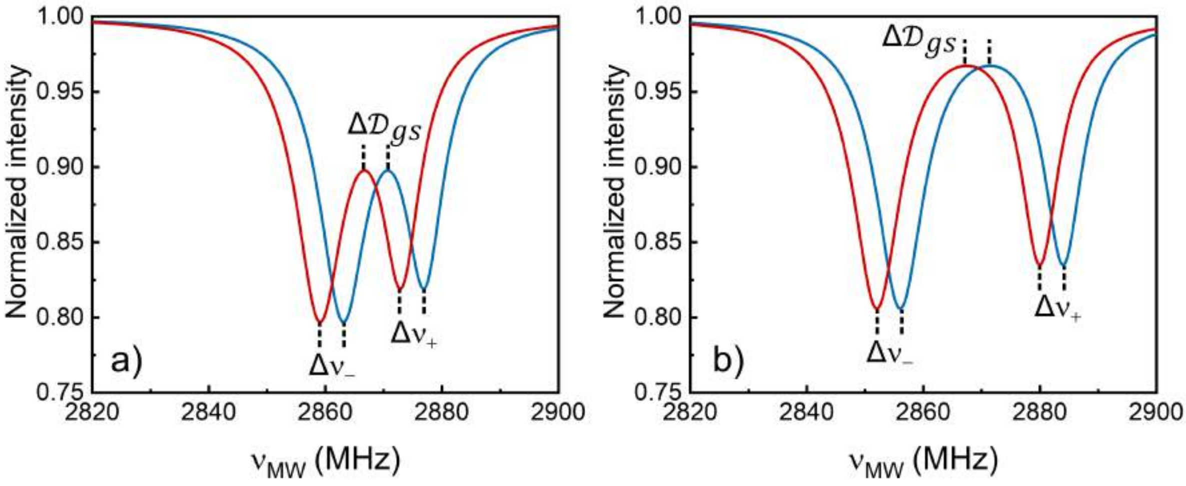

Font: The author (2022).

So far, the experimental techniques and the physical properties necessary to perform luminescence thermometry with the LIR and ODMR techniques have been discussed. Thus, in order to characterize the thermal response of the luminescent nanothermometers by implementing two different optical techniques, we will discuss in the section 2.3 the concepts of thermal sensitivity and thermal resolution that are employed as comparative parameters to quantify the efficiency of luminescent nanothermometers. As will be shown, these thermal parameters allow one to compare thermometric systems based on luminescence even with the use of different experimental techniques.

2.3 RELATIVE SENSITIVITY AND THERMAL RESOLUTION

The figure of merit used to quantify the efficiency of any physical sensing device is the sensitivity of the apparatus relative to the variations of the measured physical quantity. For luminescence-based techniques, the sensing efficiency of a thermometric technique is determined by the sensitivity, S, commonly defined in the literature as [5]

$$S = \frac{\partial Q}{\partial T}. \tag{2.21}$$

The Equation 2.21 above is a general expression for any thermometric technique that measures a temperature related quantity Q and is a measure of the magnitude of the changes in Q for an infinitesimal temperature change. In our case, the measured parameters are the LIR (R) for the lanthanide codoped system and the resonance frequency ν of the spin projection $|m_S = +1\rangle$ for the nitrogen-vacancy defects in nanodiamonds. The sensitivity relation given in Equation 2.21 is given in units of the thermal quantity Q over K. Thus, for LIR-based nanothermometers, the thermal sensitivity is defined with the use of the Equation 2.5 as

$$S^{LIR} = \frac{\partial R}{\partial T} = R\,\frac{\Delta E}{k_B T^2}. \tag{2.22}$$

Meanwhile, for ODMR-based nanothermometry, we can write down the expression for the thermal sensitivity as:

$$S^{ODMR} = \frac{\partial \nu}{\partial T}. \tag{2.23}$$

However, depending on the implemented luminescence-based thermometric technique, the thermal measurement parameter Q can have different orders of magnitude which makes S not suitable for comparison between different sensing methods. Thus, the relative sensitivity, S_R , is used for comparing the sensitivity of different temperature sensing techniques and can be written as

$$S_R = \frac{S}{Q} = \frac{1}{Q}\left|\frac{\partial Q}{\partial T}\right|. \tag{2.24}$$

The S_R parameter is given in units of K^{-1} or $\%$ K^{-1}. Now we can obtain expressions in order to compare the thermal sensitivities for two different temperature sensing techniques, as our case using LIR and ODMR methods. In this sense, one can obtain direct expressions for S_R once implemented the two strategies. The expression for LIR-based systems can be obtained with the use of Equations 2.24 and 2.5 expressed as:

$$S_R^{LIR} = \frac{S}{R} = \frac{1}{R}\left|\frac{\partial Q}{\partial T}\right| = \frac{\Delta E}{k_B T^2}, \tag{2.25}$$

which depends on the LIR parameter ΔE and on the temperature. As can be noticed in Equation 2.25, the relative sensitivity S_R of a system can be improved if the energy gap ΔE between the two thermally coupled levels is increased as long as the conditions necessary to perform the LIR measurements are fulfilled. The S_R values also depend on the temperature at which the measurements are performed.

On the other hand, for thermometric systems based on ODMR, the relative sensitivity is directly obtained through

$$S_R = \frac{S}{\nu} = \frac{1}{\nu}\left|\frac{\partial \nu}{\partial T}\right|. \tag{2.26}$$

The parameter S_R^{LIR} is the most common figure of merit used to characterize LIR-based nanothermometers. For instance, Ln^{3+} codoped nanothermometers typically present S_R^{LIR} values ranging from 0.3 $\%$ K^{-1} [114] up to 9.6 $\%$ K^{-1} [9]. More specifically, LIR nanothermometry performed with Yb^{3+}/Er^{3+}doped results in S_R^{LIR} values between 0.5 $\%$ K^{-1} and 2.88 $\%$ K^{-1} [115]. On the other hand, for ODMR-based nanothermometry with NV^{-} defects, the S^{ODMR} parameter (Equation 2.23) is often employed to characterize nanothermometers. Ensemble measurements with NV^{-} defects on bulk diamond reported S^{ODMR} values of -74 kHz·K^{-1} [116]. However, for temperature measurements with individual NCs, S^{ODMR} varies between -50 kHz·K^{-1} to -100 kHz·K^{-1} [117]. This fluctuation on the thermal response of individual ODMR-based nanothermometers is due to the crystal strains [109], surface states and possibly to thermal calibration difficulties [117]. In order to compare both techniques used in this work, the S_R^{ODMR} value can be obtained for ODMR-based nanothermometers with use of equation 2.26 for the minimum and maximum values reported for individual NCs, which results in $S_R^{ODMR} \simeq 1.7 \times 10^{-3}$ $\%$ K^{-1} and $\simeq 3.5 \times 10^{-3}$ $\%$ K^{-1}, respectively, for a resonance frequency of $\nu = 2.87$ GHz.

It can be noticed that S_R^{ODMR} values found in literature are lower than the measured S_R^{LIR} for Ln^{3+} compounds. Nevertheless, this low relative sensitivity value obtained for NV^{-} -doped nanodiamonds does not condemn their implementation as high accuracy nanothermometers. As discussed in subsection 2.3.1, when dealing with single ODMR-based thermal sensors, there are physical parameters other than S_R^{ODMR} that define the capabilities of an individual nanothermometer. In this sense, besides of measuring S_R with both LIR and ODMR techniques, it is of particular importance to consider another thermal parameter for comparing the nanothermometers: the thermal resolution, whose definition is given as follows.

The thermal resolution of a system, δT , is defined as the minimum temperature interval that can be measured with the temperature sensing device. This parameter is of particular importance because it takes into account some practical limitations of the experimental system, such as signal-to-noise ratio and emission efficiency of the doped crystal. Such practical effects are disregarded when describing thermal performance with S and S_R [15]. The definition of

δT is given by [118]

$$\delta T = \frac{\sigma_Q}{S_R}, \tag{2.27}$$

where σ_Q is the standard deviation of the measured thermal parameter Q over a set of measurements. Equation 2.27 returns the thermal resolution considering the statistical error of the measurements, taking in account the limitations imposed by the experimental apparatus. Besides, δT also depends on the relative sensitivity of a given thermometer in such a way that smaller thermal resolutions are achieved with high sensitivity thermometers [11].

However, equation 2.27 is suitable when working with ensemble measurements or when dealing with statistical errors obtained through averages over a set of measurements with individual particles, as reported in the references [24, 23]. The averages over a set do not take in account the individual characteristics of a particular nanothermometer. Therefore, when thermal measurements are performed with a single thermometer, a new definition of thermal resolution must be used in order to obtain accurate values for δT. In this sense, the measurement errors obtained from the single particle measurements need to be taken into account, along with the individual relative sensitivity values. This is the subject of the next subsection, in which the method of determining the thermal resolution of individual nanothermometers will be discussed.

2.3.1 Thermal resolution of individual NCs

The method used to determine the thermal resolution of individual NCs is not the same as those used for ensembles of NCs. This arises from the fact that for individual NCs, the measured thermal parameters obtained from the LIR or ODMR measurements may be correlated. In the following, the methods used for obtaining δT for the experimental results presented in the chapters 3 and 4 are described.

As mentioned in section 2.3, the thermal resolution of a thermometer δT is defined as the minimum temperature change that the system is able to measure confidently, thus it is a function of the thermometric measured parameter Q. One can expand δT in Taylor's Series and truncate to the first non-vanishing term, which results in

$$\delta T \;=\; \frac{1}{S_R}\frac{\delta Q}{Q}. \tag{2.28}$$

According to Brites *et. al.* [118], the uncertainty in the determination of Q, δQ, can be calculated either by measuring a set of Q values in the same experimental condition, making a histogram and calculating the standard deviation; or by propagating the uncertainties from the signal-to-noise ratio of the detection system. Even though these procedures are well-established, they are not suitable to individual calibration because of the possible correlations of the measured thermal parameters and individual thermal responses of each nanothermometer. A different approach which can also be used to gain more physical intuition about the system is discussed below.

As will be shown in the next chapters, the calibration of the thermometer is made by fitting the Q (LIR or ODMR frequency shift) vs. temperature data and typically obtaining two parameters: α , and β. Thus, for a function fitted with two arbitrary parameters α and β, the fitting is performed by standard linear regression, in which it is also possible to calculate the variance-covariance matrix, defined by [119]

$$\Sigma = \begin{bmatrix} \sigma^2(\beta) & \mathrm{Cov}(\beta,\alpha) \\ \mathrm{Cov}(\alpha,\beta) & \sigma^2(\alpha) \end{bmatrix},$$

where

$$\sigma^{\,2}(\gamma) \;=\; E\left\{[\gamma - E\,(\gamma)]^{\,2}\right\},$$

is the variance of the variable $\gamma = \alpha$ or β, where $E[\gamma]$ is its the expected value, and

$$\mathrm{Cov}(\alpha,\beta) = \mathrm{Cov}(\beta,\alpha) = E\{[\beta - E(\beta)][\alpha - E(\alpha)]\},$$

,

is the covariance of the two variables α and β.

If the two variables are independent random variables, the covariance between them must vanish, and the variance-covariance matrix becomes diagonal. Thus each element of the diagonal completely characterizes the statistical properties of its corresponding parameter. In the opposite situation, where the variables are not independent, the Σ matrix is not diagonal, but still symmetric.

Performing the linear regression via a Least Mean Squares algorithm, it was verified that the covariance matrices for all fittings of the LIR-based thermometers are not diagonal, which means that α and β are correlated. The physical meaning for this correlation relies on the choice of the Boltzmann's Law to model the photophysical dynamics of the system. As discussed in a recent work [23], the authors used the same codopants used in this thesis, but in a $\mathrm{NaYF_4}$ matrix and showed that the dynamics of non-radiative absorption and decay of the Er^{3+} ions leads to a deviation of the Intensity Ratio from the Boltzmann law, for the same thermally coupled levels used in this work.

For instance, a typical LIR measurement R can be rewritten in terms of its logarithm as a new function $R' = ln(R) = \beta - \alpha/T$, where $\beta = ln(A)$ depends on the radiative decay rates and $\alpha = \Delta E/k_B$ is related to the energy gap ΔE (see Equations 2.5 and 2.6). However, experimental results [11] show that the ΔE parameter evaluated by the Boltzmann law may actually not be the spectroscopic value, but an apparent value that depends also on the radiative decay rates. Therefore, α and β must be correlated in experiments. An important consequence is that the error propagation to obtain derived quantities as the thermal resolution for the LIR technique must consider the off-diagonal terms in Σ.

In order to determine δR, it is possible to set that, for a fixed temperature T_0, $X_0 = 1/T_0$ and R as $R(\alpha, \beta)$. Thus, the δR can be written in matrix form [119]

$$(\delta R)^2 = \begin{bmatrix} 1 & X_0 \end{bmatrix} \cdot \begin{bmatrix} \sigma^2(\beta) & \mathrm{Cov}(\beta, \alpha) \\ \mathrm{Cov}(\alpha, \beta) & \sigma^2(\beta) \end{bmatrix} \cdot \begin{bmatrix} 1 \\ X_0 \end{bmatrix},$$

The subsequent calculations of all related quantities presented in the experimental results contained in the next chapter (section 3.5 Table 1) follows from the standard error propagation presented in this section.

For individual ODMR-based nanothermometers, the thermal resolution also depends on a variety of optical parameters that characterize a single nitrogen-vacancy emitter. These parameters determine the minimum frequency changes detectable with the ODMR system, $\delta\nu$, given by [76]

$$\delta\nu = \frac{\Delta f}{2C\sqrt{I_0 t}}, \tag{2.29}$$

in which Δf is the half width at half maximum of the ODMR resonance curve, $C \approx 25\%$ is the optical contrast between $m_s = 0$ and $m_s = \pm 1$, I_0 is the photon count rate and t is the integration time of each measurement. It is worth pointing out that the photon count rate, ODMR contrast and integration time depend on the optical apparatus used to perform the ODMR measurements. Thus, by considering the general formula for the thermal resolution given by Equation 2.27, one can obtain the expression for the thermal sensitivity of individual nitrogen-vacancy nanothermometers

$$\delta T = \frac{1}{S_R}\frac{\delta\nu}{\nu} = \frac{1}{\frac{\partial\nu}{\partial T}}\frac{\Delta f}{2C\sqrt{I_0 t}}. \tag{2.30}$$

With Equation 2.30 it is possible to determine the thermal resolution of the thermometers based on individual nitrogen-vacancy defects and compare it with other thermal sensing techniques. The equation 2.30 will be applied for obtaining δT for NCs with single NV$^-$ defects presented in chapter 4 discussions.

To get a better idea about the thermal resolution of individual nanothermometers compared to ensemble measurements with LIR and ODMR techniques, some results reported in literature can be mentioned. Typical ensemble measurements performed with LIR on Ln^{3+} -doped NCs returns thermal resolutions ranging from $\delta T \sim 1.0$ to 0.1 K at room temperature [44]. Despite only a few works can be found in literature on LIR thermometry with single NCs, similar thermal resolutions were reported for individual ratiometric nanothermometers. For example, LIR measurements performed on individual NCs doped with Yb^{3+}/Er^{3+}[24] and Nd^{3+} [52] were capable of achieving thermal resolutions of $\delta T \simeq$ 0.3 K at 300 K, which are quite close to the ensemble results and are within the range necessary for biological applications [44]. Meanwhile, the big asset of ODMR thermal sensing with individual NCs its definitely its high thermal resolution if compared to ensemble measurements. For instance, Neummann *et al.* reported results on ODMR-based individual nanothermometers with thermal resolution up to 1 mK [120]. In a similar study, by using single nanodiamonds doped with about 200 NV$^-$ centers, Kucsko *et al.* reported thermal resolutions as high as 1.8 mK [85]. In other work, Fujiwara and collaborators reported $\delta T \simeq$ 0.2 K for nanodiamonds doped with $\sim$ 500 NV$^-$ centers used for monitoring the temperature inside living organisms. For comparison, thermal sensing using ensembles of nanodiamonds achieved thermal resolutions of $\simeq$ 2.3 K which is due to possible differences on the thermal responses between the nanodiamonds [117]. This result is an order of magnitude higher than for the individual nanodiamonds and indicate that the individual thermal response of each nanodiamond need to be counted on for their implementation as nanothermometers. It reinforces the assumption that single nanodiamonds can be implemented as high sensitivity nanothermometers even with low relative sensitivity values, as mentioned before. These results found in literature for single ODMR-based sensing devices show that thermal resolutions obtained with this technique are similar and even higher than those obtained with individual Ln^{3+} -doped NCs. However, the main observation that can be made about these results is the high thermal sensing performance of individual NCs if compared to ensemble measurements that, in the case of single nanodiamonds, may present thermal resolutions three orders of magnitude smaller when performed with single NCs (up to the mK scale). Thus, working with single nanothermometers through both optical techniques described in the former sections allows one to perform temperature sensing with high spatial and thermal precision in very similar application scenarios.

Up to now the possibilities of investigating the thermal capabilities of single nanothermometers have been discussed. However, the experimental techniques that allow one to detect the luminescence of individual NCs still haven't been presented. Thus, in order to discuss the detection of single NCs through their emitted luminescence with sub-micrometric spatial resolution, the next section is dedicated to the description of the working principles of a luminescence microscopy setup that allows us to perform the identification of single NCs necessary for the experimental analysis presented in the chapters 3 and 4.

2.4 PRINCIPLES OF HIGH-RESOLUTION LUMINESCENCE MICROSCOPY

As the aim of this Thesis is to perform thermometric measurements with individual nanothermometers, it is essential to introduce the experimental methods used for the detection of single luminescent NCs. The samples used to perform the experimental investigations consist in an amount of single NCs spread over a glass coverslip surrounded by air or liquid environments. Therefore, it is necessary to implement the method of sample scanning microscopy in order to spatially localize a single NC and perform the subsequent acquisition of the emitted light from each selected NC. This technique allows one to work with the same set of single NCs in different experimental situations. For example, a standard sample scanning setup is precise enough to perform experimental measurements on single nanothermometers in different environments (air and liquid media), as will be presented in the chapter 3 for LIR-based Y_2O_3:Yb^{3+}/Er^{3+}nanothermometers. Besides, this section will also present the scanning confocal microscopy method implemented for the detection of $\sim$ 25 nm diameter nanodiamonds, necessary to study the thermal effects with the ODMR technique on single nitrogen-vacancy defects as presented in chapter 4. As discussed in subsection 2.4.1, the confocal microscopy technique is capable of performing luminescence images with better resolution than the standard microscopy, and consequently, is capable of locating individual NCs spatially with high precision. The general aspects of these two optical microscopy techniques along with the definition of optical resolution for both methods are briefly presented.

2.4.1 Sample scanning optical microscopy

In general lines, the sample scanning technique consists in focusing laser light on a diffraction-limited region of a sample and collecting the emitted luminescence from that same spot as a function of the samples' spatial position. In this sense, this technique allows one to construct luminescence profile of the investigated microscopic system with high spatial resolution. A typical experimental setup used for standard scanning optical microscopy is shown in Figure 13a). In this setup, a laser light beam is collimated by a lens and passes though a laser line filter in order to eliminate any wavelength other than that from the laser light source. A beam splitter (typically a dichroic mirror), reflects the excitation light into a high numerical aperture microscope objective. The laser light is tightly focused on a point-like spot and the optical signal (*e. g.* luminescence) and scattered light created at the focus are collected by the same objective and converted into a collimated beam. The dichroic beam splitter transmits light in a restricted spectral range, which is then filtered further by spectral filters and finally reaches the detector. Thus, luminescence images of the sample can be obtained pixel by pixel by scanning the sample relative to the focus and recording the correspondent intensity values (photon counts or generated voltage for avalanche photodiodes and photomultiplier tubes) for each pixel [71].

In order to understand the capabilities of a given microscope, it is interesting for us to discuss the spatial resolution of an optical system. By definition, the resolution of an optical system is given by its Point Spread Function (PSF), which is essentially the diffraction pattern that arise when a point object is imaged through the optical system (aperture, lenses, etc.) [121]. Particularly, for a circular aperture in the paraxial approximation, the PSF has the form of an Airy Disk [122]

$$PSF = \left[\frac{2J_1(\alpha r)}{\alpha r}\right]^2, \tag{2.31}$$

where $\alpha = 2\pi N.A./\lambda$; $J_1(\alpha r)$ is the Bessel function of the first kind; r is the radial distance from the point source; λ is the wavelength of the light and $N.A. = n\sin(\theta)$ is the numerical aperture of the objective. The definition of $N.A.$ depends on the refractive index of the

Figure 13 – Experimental setup of a simple a) scanning optical microscope and b) scanning confocal optical microscope. The arrows indicate the propagation direction of the excitation/luminescence beams. DM, dichroic mirror; F, filters; L, lens; M, mirror; O, objective lens; P, pinhole; SPC, single-photon counting device.

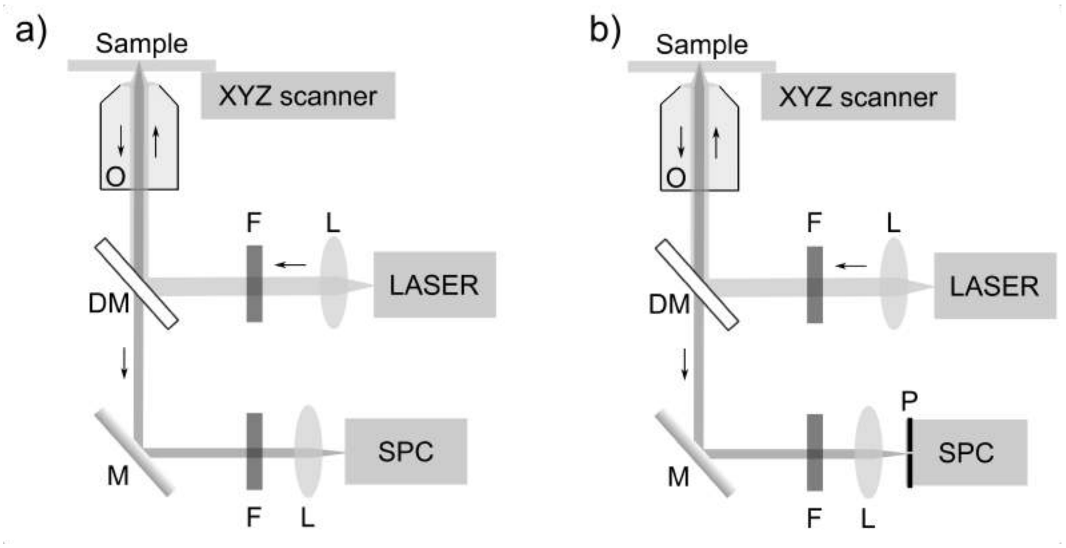

Font: Adapted from [71]

medium, n, and on the half angle of the maximum cone of light converging or diverging from an illuminated spot, θ. The PSF function for a circular aperture is plotted in Figure 14. It can be noticed that the PSF function presents maximum intensity value for $\alpha r = 0$ with relative maximum and minimum points close to the maximum value that define a diffraction pattern. The first minimum of the PSF is obtained at $\alpha r = 3.832$ which corresponds to $r = 0.61\lambda/N.A.$.

A useful way of determine the resolution of an optical system is to measure the width between the half-power points of the most intense lobe of the PSF which is named full-width at half-maximum ($FWHM$) and is defined as [121]

$$FWHM = \frac{0.51\lambda}{n\sin(\theta)} = \frac{0.51\lambda}{N.A.}. \tag{2.32}$$

Equation 2.32 returns the width of the image of a point object and is also called "the single point resolution" of the standard optical microscope. Equation 2.32 also defines the Sparrow resolution limit [71], which is the distance for which a decrease on the intensity of two perfect point light sources with equal intensities becomes immeasurable [123]. The Sparrow resolution criterion is equally applied for optical systems studied with coherent or incoherent light sources.

As mentioned before, the first minimum of the PSF (see Equation 2.31) is given at $r = 0.61\lambda/N.A.$. The PSF circle inside the first minimum is called Airy disk and its radius defines the Rayleigh distance, d_R [71]. The relation between Rayleigh distance and the PSF function is schematically shown in Figure 14, where the spatial distribution of the PSF is plotted according to Equation 2.31 for an ordinary optical system. In Figure 14, the dark color represents the points with non-null intensity, meanwhile the white color represents the minimum intensity points. The central circles have been slightly darkened for better observation of the so-called Airy rings, *i. e.*, the observable concentric circular intensity patterns. From these concepts, one can define a new criterion for the resolution of optical systems, denominated as the Rayleigh resolution limit for two identical points. As the name suggests, this criterion supposes that two point light sources will be distinguished when the central maximum of the PSF of one point is located at the first minimum of the PSF for the other light source [121]. Thus, it means that the two light sources can be distinguished if they are separated by a distance d_R, given by

$$d_R = \frac{0.61\lambda}{n\sin(\theta)} = \frac{0.61\lambda}{N.A.}. \tag{2.33}$$

The intensity profiles of two point-like light sources for different distances between the points are plotted in Figure 15. Both images (top row) and the PSF profiles (bottom row) on Figure 15 were plotted with Equation 2.31. The intensity pattern shown in Figure 15a) presents two points spaced enough to obtain a well resolved image of both light sources. Figure 15b) represents the two points separated by d_R, which is, as mentioned before, the minimum distance for them to be resolved in space, according to the Rayleigh resolution criterion. On Figure 2.33c) the image of the two points is not resolved. The separation between the points, were $\alpha r = 5\lambda/N.A.$ and $\alpha r = 2\lambda/N.A.$ for Figures 15a) and c), respectively.

From the definition of the Sparrow and Rayleigh resolution criteria defined above on Equations 2.32 and 2.33, it can be noticed that there are two ways of improving the resolution of a given optical system. First, one can reduce the excitation wavelength λ used to study the samples. However, when such manipulation of λ is not possible, *e. g.*, when investigating specific absorption/emission lines of given material, it is still possible improve the spatial resolution of the optical system by increasing the refractive index of the medium n, which is done by using immersion objectives. Such objectives work with high refractive index liquids between the objective's pupil and the sample. Two very common immersion fluids are water ($n = 1.33$) and oil ($n = 1.52$) [71] and the latter is used on the experimental arrangements described on chapters 3 and 4.

Figure 14 – Normalized PSF of a simple lens and the correspondent Airy pattern. The gray solid (dashed) lines represent the points of maximum (minimum) of the PSF. The Rayleigh distance, d_R, is given by the separation between the point of maximum intensity ($\alpha r = 0$) and the first intensity minimum ($\alpha r = 3.832$).

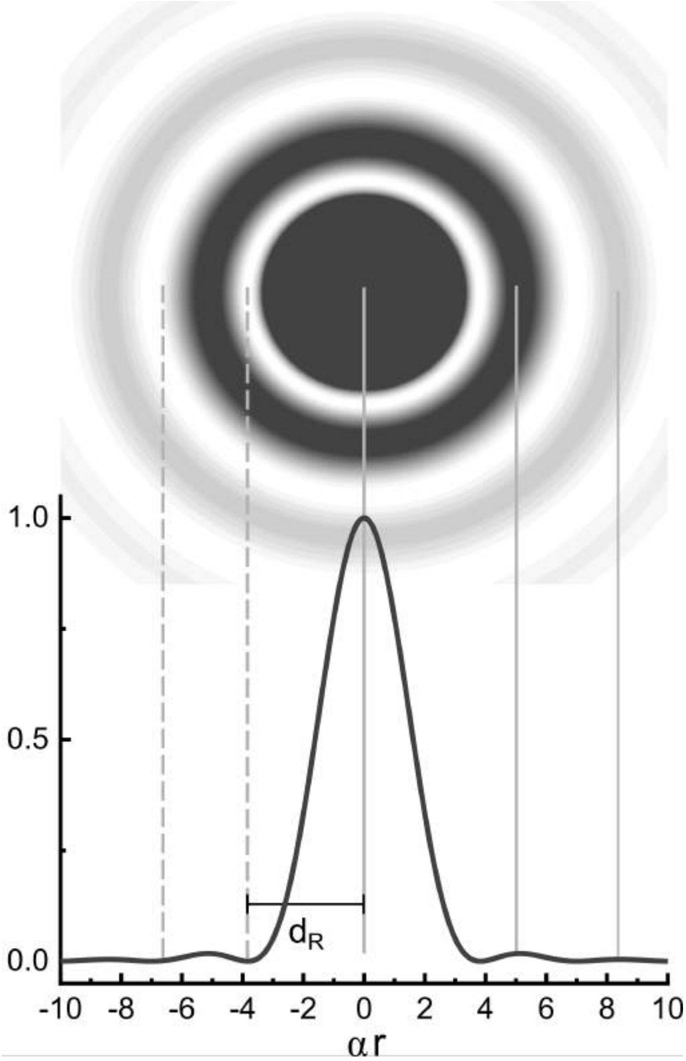

Font: Adapted from [124]

As shown in references [23, 24, 11] and the results presented on the next chapter, the sample scanning microscopy is very suitable to study individual fluorophores, presenting spatial resolution comparable to the emission wavelength of individual NCs. For instance, when working with lanthanide-ion doped on micro- and nano-particles, an individual NC is doped with thousands of optical active ions, which generate intense luminescence bands easily detected by using standard sample scanning microscopy. However, when working with the light detection from fainter particles with a considerably smaller amount of emitters, the detection system may suffer from increased background from out-of-focus planes relative to emission intensity of single NCs. The extreme situation happens when it is necessary to detect the

Figure 15 – Intensity patterns of two identical light sources presenting a) a well resolved image of the two points, b) two points separated by d_R, satisfying the Rayleigh criterion and c) an unresolved image of the light sources.

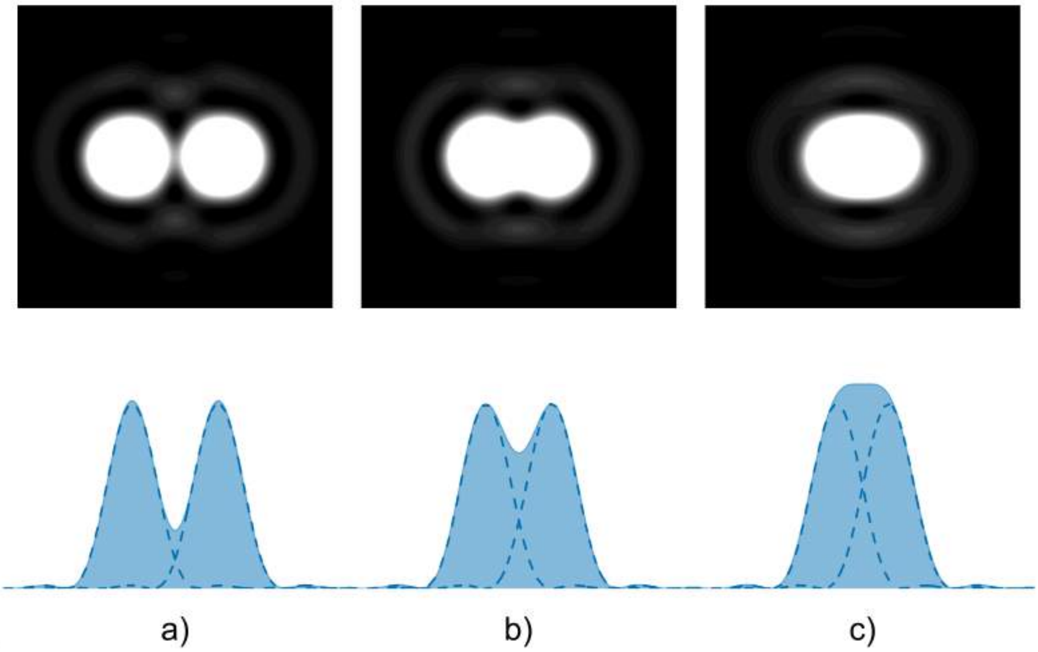

Font: The author (2022).

fluorescence of single emitters, as is the case for individual nanodiamonds containing a single nitrogen-vacancy defect. For studying these fluorophores, as shown in chapter 4, the detection of these NCs can only be performed with the use of confocal microscopy, discussed in subsection 2.4.2.

2.4.2 Scanning optical confocal microscopy

As mentioned in subsection 2.4.1, sometimes the detection of the emitted luminescence from single NCs is not possible due to limited spatial resolution of the system and the high background photon counts. For instance, the study of biological samples with standard optical microscopy may present blurring, loss of contrast and resolution due to the presence of reflective surfaces, imperfections and light arising from different tissue depths [125]. In order to fix these problems, in such cases the standard scanning optical microscopy is improved with the use of spatial filters which in turn enhance the spatial resolution of the optical systems and suppress most of the undesirable light from out-of-focus optical planes.

One particular technique often used is the confocal optical microscopy, which experimental setup is presented on Figure 13b). The main difference between the confocal microscopy and the standard microscopy [see Figure 13a)] is the presence of an aperture, also called a "pinhole", located in front of the detector in a plane conjugated with the focal point of the objective lens. The conjugation of the objective focal plane and the detection point at the pinhole aperture justifies the use of the term "confocal". This technique is then based on the fact that only the light originating from the focal area is able to pass through the detection pinhole and hence reach the detector. It means that light sources which are laterally displaced relative to the focal point will not reach the photon counter, being blocked by the pinhole walls. Besides, light originating from points displaced along the optical axis but that are not located at the focal plane of the objective will be strongly attenuated by the detection pinhole. The confocal principle is depicted on Figure 16. It is possible to see that the light emitted by one object (square), which is located on the optical axis lying in the conjugated focal plane, passes though the pinhole aperture and reaches the detector. The objects that are located on the optical axis but not on the focal plane (circle) have their luminescence strongly attenuated by the detection pinhole. Meanwhile, for objects located at the focal plane but laterally displaced from the objective focus (triangle), their emitted light is completely blocked by the pinhole [71].

Just as in the case of standard microscopy, discussed previously, the resolution of a confocal microscope is defined by the PSF of the optical system. However, in the case of confocal microscopy, the optical resolution of the system depends not only on the PSF of objective lens, but also on the PSF due to the presence of the aperture in front of the detector. This new consideration results in an effective PSF for the confocal setup, PSF_C, given by the square of the PSF for the standard microscope, and can be written as [121]

$$PSF_C = (PSF)^2 = \left\{ \left[\frac{2J_1(\alpha r)}{\alpha r} \right]^2 \right\}^2 , \tag{2.34}$$

in which the parameters were also defined on the equation 2.31. The intensity profile for the confocal microscopy is plotted on Figure 17 where it also can be found the intensity profile for the PSF function of a conventional microscope. It can be readily verified that the spatial intensity profile for a confocal optical system is narrower than the conventional one, which evidences the higher resolution achieved with this technique.

By using the Sparrow resolution criterion (see subsection 2.32), it can be verified that the single point resolution for the confocal optical system is given by

Figure 16 – The confocal principle. Three luminescent objects on a sample are located at different positions. The detection paths of the each object are represented by black solid, red dashed and blue dash-dotted lines for the square, triangle and circle, respectively (colored for better visualization). L, Lens; M, mirror; O, objective; P, pinhole. SPC, single photon counter.

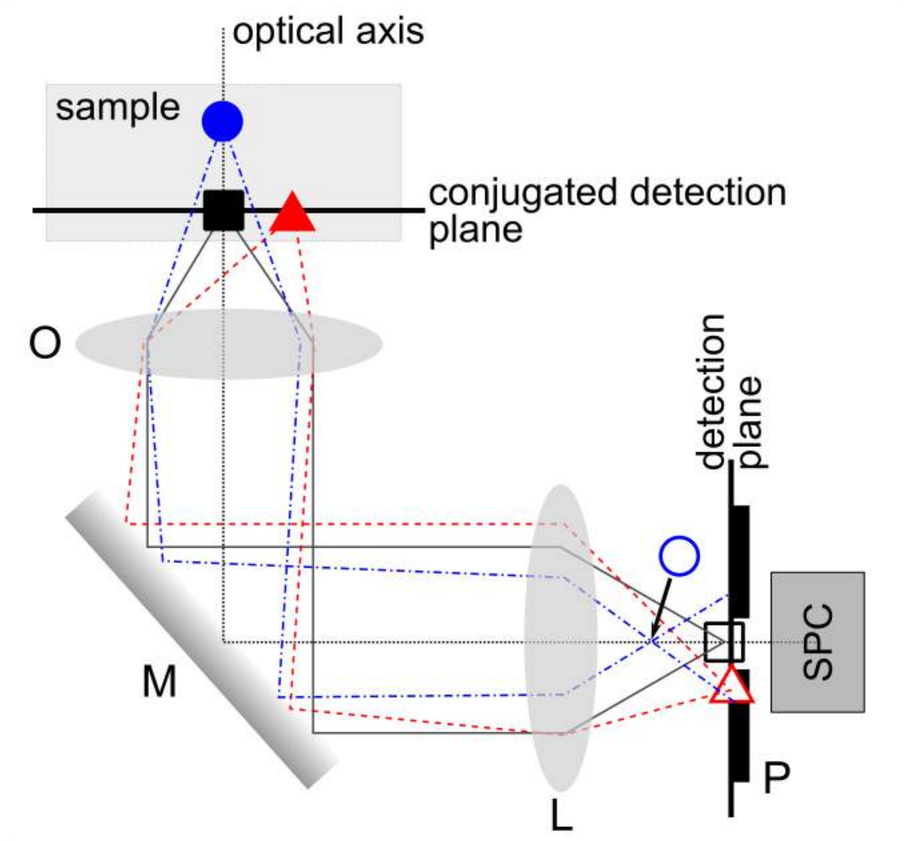

Font: Adapted from [71]

$$FWHM_C = \frac{0.37\lambda}{n\sin(\theta)} = \frac{0.37\lambda}{N.A.}, \tag{2.35}$$

where $FWHM_C$ is the full-width at half maximum of the main lobe of the PSF_C (Equation 17). Thus, $FWHM_C$ defines the single point resolution for the confocal microscopy which is around 28 % better than the resolution of the standard optical microscope. In practical situations, when working with light emitters much smaller than the excitation wavelength, the $FWHM_C$ is often used as the definition of the optical resolution of the implemented optical system [83].

If one returns to the definition of the Rayleigh criterion (subsection 2.4.1), that defines the the minimal distance for which two points can be optically resolved, one can calculate the minimum distance necessary for the two point-like sources be distinguishable with use of a confocal microscopy setup. For excitation light with wavelength λ, the Rayleigh criterion is satisfied for the confocal technique when the two points are apart by a distance d_C given by

Figure 17 – Intensity profile of the PSF for a conventional microscope (blue curve) in comparison to the PSF_C of a confocal microscope (red curve).

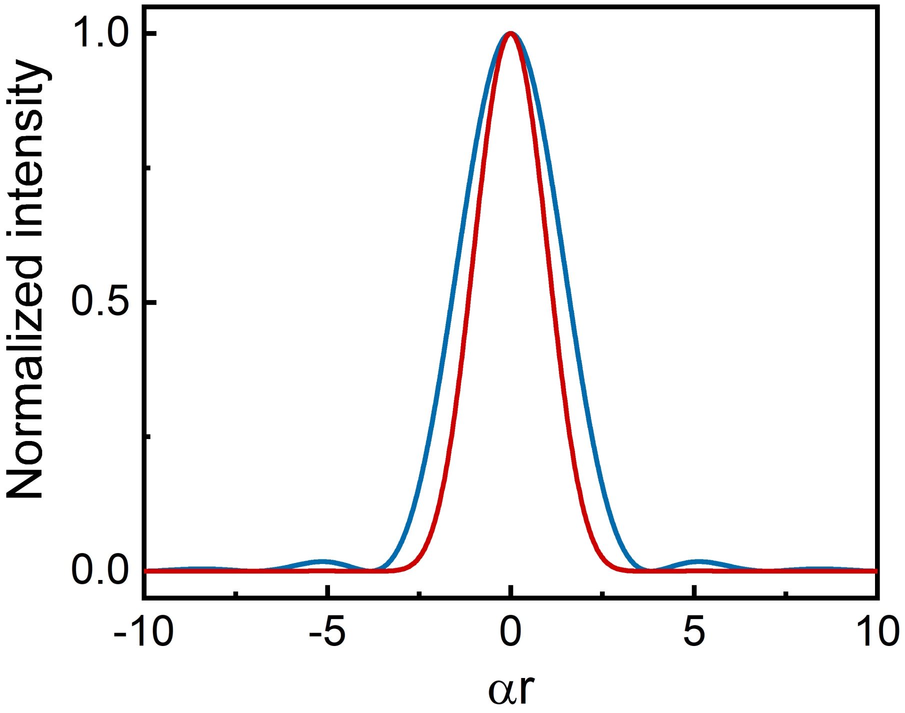

Font: The author (2022).

$$d_C = \frac{0.56\lambda}{n\sin(\theta)} = \frac{0.56\lambda}{N.A.}. \tag{2.36}$$

As can be noticed from the Equation 2.36, the Rayleigh distance for the confocal microscopy returns smaller values if compared to one obtained with the standard confocal microscopy. The concepts discussed in this section conclude the theoretical discussions and are of primary importance for the presentation of the experimental setups described on the next chapters. The determination of the single point resolution by using the Sparrow criterion for the experimental apparatus used to construct this thesis were experimentally measured in previous studies [15, 83] and the results will be used to define other necessary physical magnitudes, such as optical resolution of the microscopes, power density of the excitation beam, etc.

3 INFLUENCE OF THE SURROUNDING MEDIUM ON THE THERMAL RESPONSE OF INDIVIDUAL Yb^{3+}/Er^{3+} CODOPED YTTRIA NCS

In the previous chapter the physical concepts that enable one to perform LIR thermometry with with Yb^{3+}/Er^{3+}codoped systems have been introduced along with the main reasons to apply these fluorophores as luminescent nanothermometers. However, as discussed in subsection 2.1.5, there are some application scenarios in which the interaction of the nanothermometers and the surrounding environment needs to be taken in account in order to obtain reliable temperature measurements *in loco* with luminescent NCs. Thus, aiming at contributing to the current research in this subject, this chapter is dedicated to the experimental investigation on the influence of the circumjacent medium on the thermal response of individual Y_2O_3 NCs codoped with Yb^{3+}/Er^{3+}. The discussion begins with the description of the synthesis protocol and morphology of the luminescent NCs used in this chapter. This topic is followed by the description of the methods used to obtain the experimental results, including the sample preparation, description of the experimental setup and what were the experimental methods implemented to study the thermal response of single nanothermometers in the chosen media. The chapter is concluded with a section containing the respective results and relevant discussions.

3.1 SYNTHESIS AND MORPHOLOGY OF THE Y_2O_3 NCS CODOPED WITH Yb^{3+} AND Er^{3+}

The single Y_2O_3 codoped with Yb^{3+}/Er^{3+}NCs studied in this Thesis were synthesized by the method of homogeneous precipitation synthesis followed by further thermal treatment by the of group of Prof. Rogéria R. Gonçalves from the Chemistry Department of USP - Ribeirão Preto. Details on the technique used to synthesize individual NCs can be found in references [126, 127, 24]. The synthesis routine implemented to obtain the Yb^{3+}/Er^{3+}codoped NCs is briefly described as follows. First of all, homogeneous and fully redispersable spherical hydroxycarbonate nanoparticles, $[Y(OH)CO_3.nH_2O]$, were synthesized by urea thermolysis using yttrium nitrate ($Y(NO_3)_3.6H_2O$ 99.8% purity, Sigma Aldrich) and urea (99 - 100 % purity, Synth). The final concentrations of these precursors are respectively 0.01 mol L^{-1} and 5.00 mol L^{-1} [127]. The next step consists in introducing the Yb^{3+} and Er^{3+} ions as aqueous solutions of ytterbium nitrate and erbium nitrate which is done by dissolving $(Ln^{3+})_2O_3$ (Ln^{3+}

= Yb^{3+} and Er^{3+}) in 0.10 mol L^{-1} of nitric acid (HNO_3) aqueous solution, resulting in acid $Ln^{3+}(NO_3)$ solutions. This step was followed by the reduction of the acid excess of the Ln^{3+} (NO_3) solutions by evaporation, until a pH = 4 was achieved and the volume was adjusted to obtain 0.10 mol L^{-1} solutions. The Yb^{3+} and Er^{3+} concentrations were 0.50 % and 1.50 % relative to the Y^{3+} molar concentration, respectively, which is adequate to avoid concentration quenching [128].

A closed flask containing the solution is then heated at 80°C for 2h in order to carry on a thermolysis reaction on the solution until the nanoparticles precipitated. After a complete reaction, the temperature of the suspension is reduced to room temperature and the colloidal nanoparticles are separated by centrifugation at 4000 rpm in a centrifuge (Centribio: Centrilab 80 - 2B). After that, the wet product was washed five times with distilled water, and dried at 70°C for 6h. The 0.5% Er^{3+} /1.5% Yb^{3+} : Y_2O_3 NCs were obtained after $[Y(OH)(CO_3)_3.nH_2O]$ annealing under air at 900°C for 2h. The heating rate was 5°C min^{-1}. This procedure is carried on in order to eliminate the carbonate and hydroxyl groups, minimizing the luminescence quenching effects [127].

As mentioned in references [127, 24], the adopted reactional and post-reactional conditions results in the formation of pure body-centered Y_2O_3 NCs, with Ia_3 space group according to JCPDS card 01-074-0553 [see Figure 18c)]. Morphology and size dispersion of the synthesized NCs were obtained through transmission electron microscopy (TEM) using a JEOL JEM-100CX II microscope at an accelerating voltage of 100 kV as seen in Figure 18a) and b). For the TEM measurements, the NCs were dispersed into anhydrous ethanol, and a drop of the solution was placed over a carbon coated microscope copper grid [24]. As can be seen on Figure 18a) , the annealed NCs present spherical morphology and high size dispersion, with particle size ranging from 70 nm to 150 nm. The average NC size obtained was (110 ± 20) nm. Raman scattering spectra of the NCs presented no additional peaks related to impurities, indicating a high phase purity and homogeneous dispersion of the RE ions into the Y_2O_3 crystal lattice [24].

Figure 18 – a) Transmission electron microscopy (TEM) image of multiple Y_2O_3:Yb^{3+}/Er^{3+}NCs b) Size distribution of the Yb^{3+}/Er^{3+}codoped NCs. The particles can be found in sizes ranging from ≈ 70 nm to ≈ 150 nm with average value of 120 ± 20 nm. c) R-X diffractogram of the codoped Y_2O_3:Yb^{3+}/$Er^{3+}$and pristine Y_2O_3 confirming the body centered cubic phase structure of the NCs.

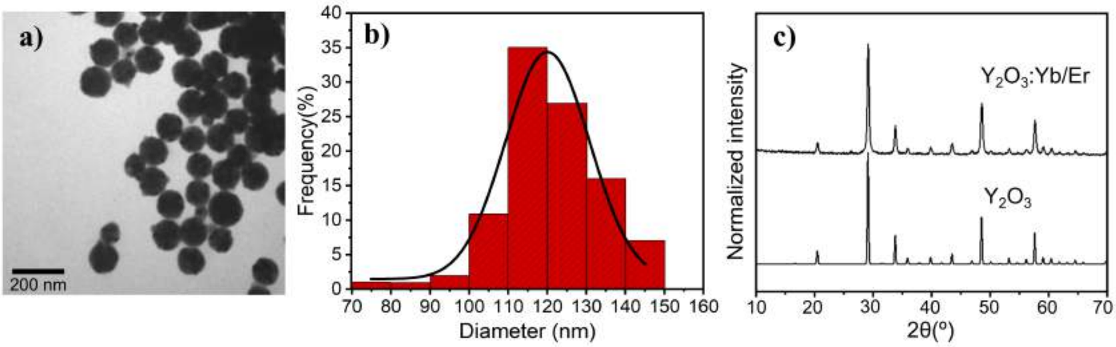

Font: Adapted from [11]

3.2 SAMPLE PREPARATION

In order to carry out LIR measurements on single NCs, it is necessary to produce samples in which individual NCs can be located and identified individually through their luminescence characteristics even after the deposition of liquids over the sample. These requirements are met with the sample preparation method described below.

For the experimental measurements with individual Yb^{3+}/Er^{3+}codoped NCs, individual NCs randomly spread over a glass coverslip surface were used. First of all, a colloidal solution was prepared by suspending 0.01 g of a Yb^{3+}/Er^{3+}:Y_2O_3 NCs powder in 1 mL of isopropyl alcohol. The colloid is then placed in a ultrasonic bath for 15 minutes in order to break eventual large agglomerates. After sonication, the dispersion is stored during 24h for decanting before deposition in a glass coverslip. This procedure is carried out in order to assure the decanting of possible reminiscent agglomerates to the bottom of the vial containing the colloid. It increases the probabilities of taking a superficial droplet of the colloid containing a majority of single NCs. Thus, when the decanting time is achieved, the samples with individual NCs can be prepared.

Clean Borosilicate glass coverslips (Menzel-Gläser $\#1$) were chosen to be the substrate in which the NCs are deposited on. When working with the luminescence detection of individual NCs deposited over a substrate, the cleaning of the glass coverslips before deposition is of great importance. Impurities such as dust grains (with micrometric size), any luminescent or reflective particles (dyes from the coverslip package, tiny glass or metallic particles) or even impurities due the handling of the substrate may prevent the detection of the NCs. Thus, the glass coverslips are treated according the cleaning protocol described in what follows. First, clean beakers are rinsed with deionized water (Milli - Q™ with resistivity of ~ 18 MΩ cm) and used to prepare 60 mL of a washing solution composed by 2% of Hellmanex III™ glass cleaning solution in deionized water. Then, the cleaning solution is placed in a heated ultrasonic bath at a temperature of ~ 40°C. The glass coverslips are then placed in a coverslip holder and put inside the beaker with the cleaning solution during 50 minutes. Obviously, the volume of the solution must be enough to fully cover the coverslips. In order to do the first rinse on the coverslips, after the sonication time, the holder containing the glass coverslips is placed in a beaker filled with deionized water and then again in the ultrasonic bath for another 10 minutes. After this time, the beaker with the glass coverslips is removed from the sonicator. The final cleaning step is to manually rinse the coverslips, one by one, during 2 minutes in a third beaker with deionized water followed by drying the coverslips with a nitrogen flow. This last rinse procedure is performed manually by holding the coverslips with tweezers and performing gentle interspersed circular and zig-zag movements with the coverslip immersed in water. After drying, the clean coverslips are now (finally) ready for the deposition of the NCs colloid.

Once the decanting time is reached and the coverslips are clean, the deposition of the NCs may be done. As said before, the aim is to produce a sample with individual NCs over the glass substrate, thus the well known spin-coating technique was used to perform the NCs deposition. This technique is commonly used to obtain thin films of various substances and to prepare samples with individual micro-nanoparticles [15, 24]. It consists on the rapid rotation of the substrate containing the suspension of particles which makes it evenly distributed over the substrate's surface resulting in a homogeneous spatial distribution of the NCs. In order to do that, 10 μL of the NC colloid are placed over the glass coverslip with the aid of a micropippete. Then, the coverslip is spin-coated in two steps (Chemat Technology inc., KW-4A), for 6 s at 2000 RPM and then 15 s at 3200 RPM. The solvent evaporates during the rotation, resulting, as intended, in NCs scattered across the surface of the coverslip [11]. As can be seen in reference [24], this deposition procedure leads to a good distribution of individual NCs, 2 - 4 μm apart from each other.

3.3 EXPERIMENTAL SETUP

The detection and spectroscopic measurements of individual NCs can be carried out with the implementation of a sample scanning luminescence microscope. The principles of sample scanning microscopy were introduced on subsection 2.4.1 and the scheme of the assembled experimental apparatus used in this work can be seen on Figure 19. In this setup, the excitation light source is a home-assembled CW fiber laser emitting at 977 nm. The excitation beam has its power controlled by a set of neutral density absorptive filters before be directed by a 50:50 beam splitter (Thorlabs BS1) to the home-made inverted optical microscope [11]. Once the excitation light arrives the inverted optical microscope, the laser beam is tightly focused over the coverslip containing the NCs by a high numerical aperture microscope objective (Edmund Optics 43905 100x N.A. = 1.25/oil immersion). The position of the sample is determined by a computer-controlled piezoelectric 3D stage (Piezosystem Jena TRITOR 100 T-403-00) which allows the optimization of the focal plane of the excitation beam along with the possibility of the sample to be scanned. The NCs emitted luminescence and the laser light reflected by the glass coverslip surface are collected by the same objective lens and sent backward to the detection system. After passing though the beam splitter, the luminescence light is filtered by a set of short-pass optical filters (Thorlabs FES0750 and Semrock FF01-842-sp-25) [11].

Figure 19 – (Left) Experimental apparatus scheme representing the inverted sample-scanning optical microscope used in this chapter. OD: optical neutral density; APD: avalanche photodiode; N.A.: numerical aperture. The selected excitation light at 977 nm is blocked by a NIR filter set, which allows detection of luminescence with wavelengths below 750 nm. (Right) Scanning luminescence image of codoped Yb^{3+}/Er^{3+} NCs obtained with the inverted sample-scanning microscope setup. The figure shows a 11×11 μm^2 region with 60 pixels in x and y directions and an integration time of 30 ms per pixel. The colorbar indicates the time averaged intensity. The pump power density used here was 6×10^3 W/cm^2.

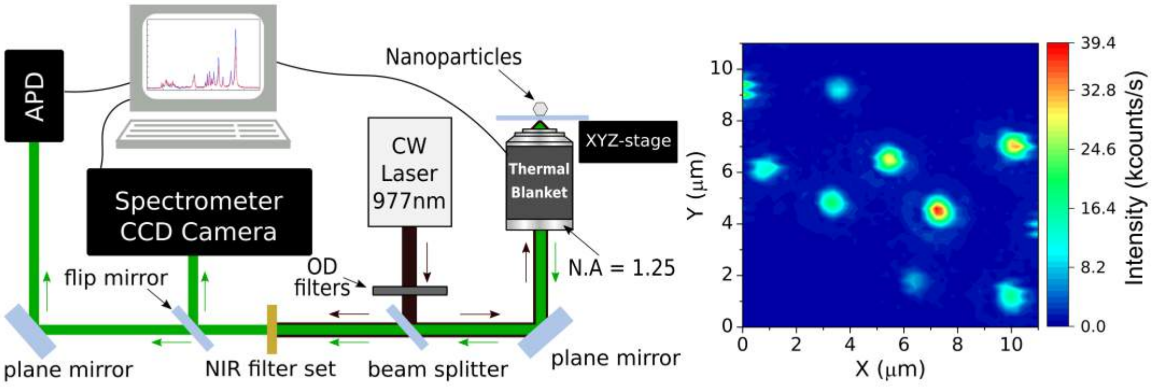

Font: Adapted from [11]

The emitted luminescence from the NCs can be directed to two different detection paths with the use of a flip mirror. With the flip mirror down, the light is sent to an Avalanche Photodiode (APD, idQuantique 100-50) which is capable of performing single photon detection and the necessary luminescence intensity measurements on individual NCs. Besides, by using this detection path, the emission intensity measurements associated with the position control of the sample enable the acquisition of the two-dimensional scanning luminescence images of the NCs. An example of a two-dimensional luminescence image of NCs is shown on the right side of Figure 19. In this Figure, it can be noticed a luminescence pattern obtained by sample scan on a $11{\times}11$ μm region in which at least eight luminescent NCs can be identified with emitted intensity values up to 39.4 kcounts/s. The image was acquired by recording the integrated intensity values during 30 ms pixel by pixel in steps of $\simeq$ 183 nm in x and y axis, resulting in a final image with 60 × 60 pixels. With the flip mirror up, the collected light can be directed to the second detection path, sending the radiation emitted by a single NC to a spectrometer (Princeton Instruments SP2500) coupled to a CCD camera (Andor DU401-BV). By choosing this detection path one can perform the spectral analysis of the luminescence emitted by the individual NCs necessary for the direct LIR measurements [11]. Once the main characteristics of the optical setup were presented, the method used to control the temperature of the sample can be discussed in details. The implemented setup for temperature control of the sample and the necessary thermal calibrations are discussed in detail on the next paragraph.

The investigation of thermal response of individual luminescent nanothermometers can be done by performing the spectral measurements of each NC while controlling the temperature of the sample. In this apparatus, a home-made heating device that consists of a thermal blanket that embraces the microscope objective is responsible for controlling the temperature of the sample. The device is computer-controlled and the local heating of the NCs is indirect, happening via the immersion oil and thus being necessary to calibrate the system by measuring the temperature of the coverslip surface with an external thermometer. It is done by measuring the temperature of the glass coverslip surface with a thermal camera (FLIR i5) placed above the inverted optical microscope, which enables the real time temperature monitoring of the sample. When working with such kind of thermal imaging of a reflective surface as glass, it is important to consider the target's thermal emissivity ϵ and reflectivity. A miscalibrated camera can generate thermal artifacts in the measurements as hotspots and misreadings. For the instrument used here, the ambient temperature and the emissivity value of the coverslip are used as entry parameters for establish the initial configuration of the camera. The room temperature was maintained between 293 - 295 K and the defined emissivity value was that of glass $\epsilon_{glass} = 0.95$. For each LIR measurement these values were checked out and the details of the calibration are described below.

Figure 20 – a) top and b) side view or the thermal camera positioning above the sample holder to do the thermal calibration of the system. c) Temperature of the glass coverslip as a function of the set temperature of the control program. The data points are displayed along with the linear fit used to calibrate the real temperature of the sample. The inset show the temperature profile of the sample obtained with the FLIR camera in which the temperature at the NCs region (center of the sample) is $T =$ 30°C (303 K). This calibration point is indicated in the graph by a black arrow. In d) presents in detail the sample holder with little magnets used for fixing the sample, corresponding to the small dashed square region on b).

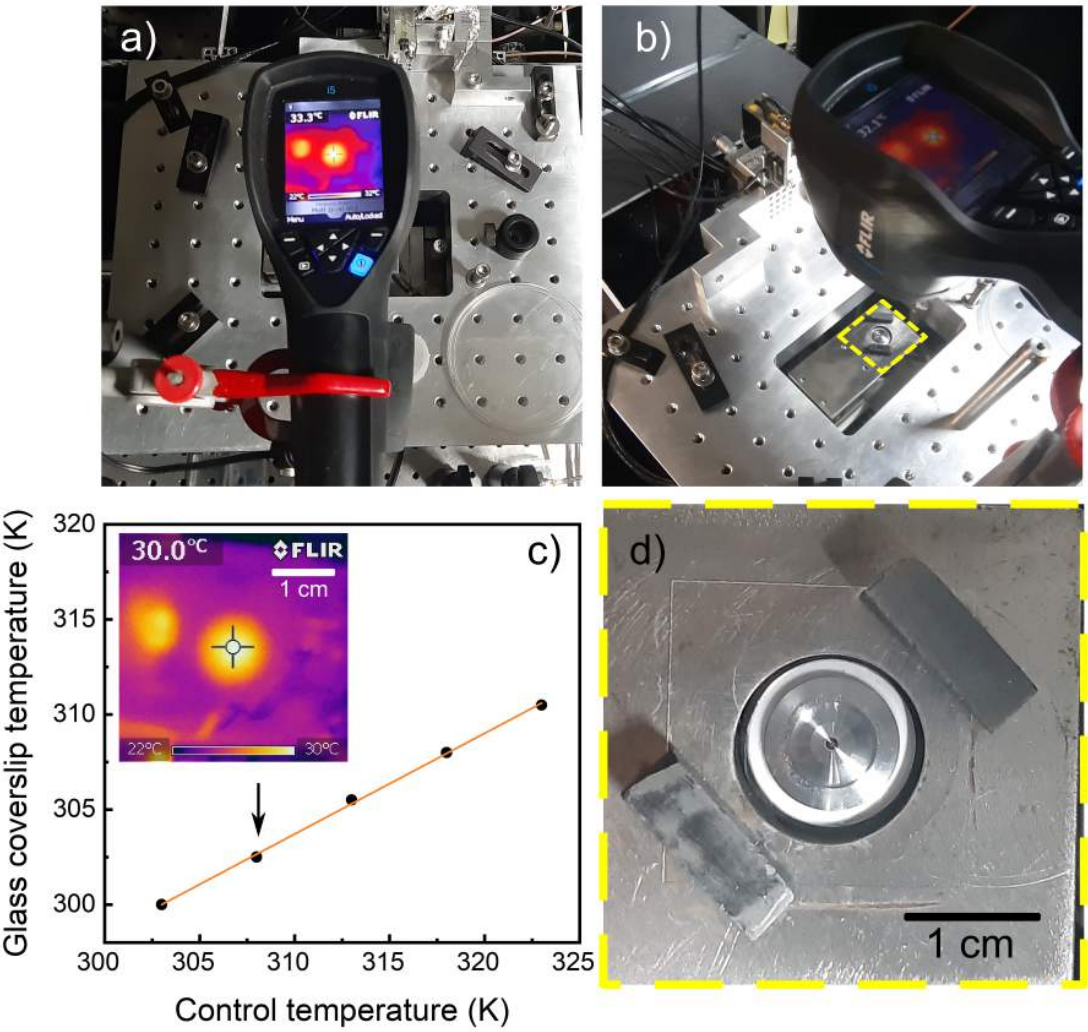

Font: The author (2022)

In Figure 20 are presented the experimental setup and the temperature data obtained with the thermal camera as a function of the temperature set on the control program. As already mentioned, the thermal camera is held above the experimental setup [see Figures 20a), b) and d)] and the indirect heating of the sample is achieved through the heating of the immersion oil in contact with the glass surface. In order to perform the calibration, the temperature of the coverslip was acquired every 5 K raised on the the control program for an input temperature interval of 25 K, ranging from 298 K to 323 K. To assure the thermal equilibrium of the system, every new measurement is performed after 20 minutes of waiting time. The inset on Figure 20c) presents the thermal profile of the sample. The color bar at the bottom of the inset indicates that the temperature over the selected area ranges from 22°C (295 K) to 30°C (303 K) which is the temperature at the center of the sample (crossed spot on inset). The temperature of the central spot was used to acquire the data points in the graph. A thermocouple placed at the surface of the heating blanket is used for monitoring the objective's temperature by the control program. A linear fit of the data was performed according to $T_S = aT_C + b$; with T_S and T_C being the temperature of the sample and the temperature read by the control program, respectively, and a and b the fitting parameters; which returns the fitted values of $a =$ (0.53 $\pm$ 0.01) and $b =$ (139 $\pm$ 3,1) K. This means that for each 1 K temperature change in the control program, there is a raise of 0.53 K on the glass surface. This new parameter is then used to calibrate the temperature control program and to perform the subsequent LIR measurements. Nevertheless, it can also be noticed from the temperature profile [inset 20c)] that the heating is homogeneous in a reasonable area ($\sim$ 1 cm^2), assuring the thermal equilibrium of NCs located at the center of the hot area. It can be noticed a second "hot spot" in the left part of the inset on Figures 20a), b) and c) but it is just the radiation generated by the thermal camera, since its temperature is higher than the room temperature. This radiation is reflected on the metallic surface of the sample holder and then detected by the thermal camera. It is a typical problem when measuring the temperature of reflective surfaces, as polished metal or glass. The detected "hot spot" is displaced relative to the sample center through a slight inclination of the thermal camera because, as said before, this reflected radiation is read by the camera as a thermal artifact and may generate temperature misreadings of the sample.

3.4 OPTICAL CHARACTERIZATION OF INDIVIDUAL NCS

After concluding the temperature calibration, the optical characterization of individual NCs can be performed. The emitted light from the Yb^{3+}/Er^{3+}codoped NCs arises from well established transition mechanisms, as discussed in the section 2.1.4. Due to nonradiative energy UC processes, under excitation laser light at 977 nm, the most intense luminescence emitted from the codoped NCs arises from the electronic transitions of Er^{3+}, presenting emission bands around 528 nm, 550 nm and 660 nm, in the green and red spectral regions, respectively. The set of NIR filters allows for the detection of luminescence below 750 nm. Thus, all the scanning luminescence images presented in this chapter were constructed from the detection of the emitted luminescence from the NCs in the visible with wavelengths smaller than 750 nm.

Figure 21 – Scanning luminescence image of a 11 × 11 μm^2 region of the sample. The white arrows designate the selected NCs for which the nanothermometry experiments were made. The pump power density used here was 6×10^3 W/cm^2 at the sample.

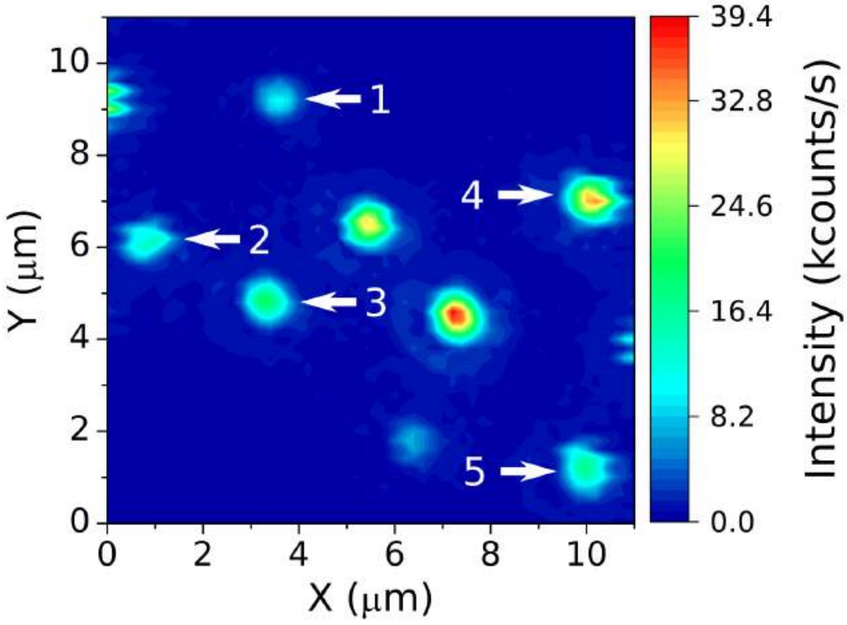

Font: Adapted from [11]

As the main goal of the experimental studies contained in this chapter is to investigate the same NCs in different surrounding media, it is necessary to identify regions with a convenient spatial distribution of single NCs. A few scanning luminescence images similar to the one shown on Figure 19 were acquired until a region with an adequate distribution of NCs was found. As discussed in the subsection 3.2 and is shown on the scanning electron microscopy images reported on reference [24], the sample preparation protocol used here leads to a suitable spatial distribution of individual NCs. Thus, as the NCs possess spherical shapes and their diameter sizes of the NCs vary between 70 nm and 150 nm, the individual NCs are selected according to a simple principle: as the number of emitting ions is proportional to the NC volume, the luminescence intensity variation between the smaller and the larger NC sizes should be around 2× in the detected luminescence signal [11]. This principle is useful to avoid the selection of possible agglomerates of NCs based on their luminescence. A good spatial distribution of NCs can be seen on the right panel of Figure 19, where at least 8 NCs can be seen in a 11 × 11 μm^2 area. To identify which particles are individual, it was considered the emission of the dimmer particle, labeled as particle 1 with around 12 kcounts/s, as the reference luminescence intensity; and twice of this value, *i. e.* around 25 kcounts/s, as being the maximum detected intensity from a single NC. The particles identified as single NCs were labeled as NC1 to NC5 and are shown on Figure 21. As will be presented in the next section, all the experimental results performed on the five selected particles follow similar trend, which is another indicative that the selected particles are indeed individual NCs [11].

Once the particles were identified, excitation power dependence studies were carried out in order to check for saturation effects. This analysis is generally performed to assure that the thermometric experiments will be performed in a non-saturated regime, *i.e.*, in a situation where the nonradiative transitions rule over the radiative ones, being one of the requirements to perform LIR thermometry with high thermal sensitivity (see subsection 2.1.3). However, in order to do that, one needs to estimate the pump intensity of the excitation beam at the objective's focal spot. In the present experiment this is done by relating power density of the focused excitation beam with the focal spot size and the average power measured right after the sample's surface. It is done by measuring the average power of the laser light $\sim$ 5 mm above the coverslip surface with a power meter (Thorlabs PM100A equipped with S120VC Si photodiode, 9.5 mm aperture). Hence, the power density of the focused beam at the sample is estimated by taking into account the spatial resolution of the optical system according to the Sparrow criterion, Equation 2.32, which was experimentally obtained by measuring the $FWHM$ on x and y directions for a single light emitter, as shown on Figure 22. Figure 22a) presents the intensity profile of the selected particles, the same shown previously. The crossed yellow dashed lines on this figure represent the selected cross sections for which the $FWHM$ were obtained through a Gaussian fitting for both x and y axis. The results are shown in Figures 22b) and c). The measured $FWHM$ is indicated by the double headed arrows and result in $FWHM_x =$ 677 nm and $FWHM_y =$ 704 nm, respectively, for x and y axis. The data points are well adjusted with Gaussian curves resulting in a fitting factor of $\chi^2 \simeq$ 0.99 for both directions. These values result in an average transverse resolution of $\simeq$ 691 nm. One can consider the theoretical value for a perfect point source (Equation 2.32) and compare it to the measured optical resolution of the system. The excitation laser light at 977 nm is the chosen wavelength used in the theoretical estimate, due to the fact that the NCs only emit light if they are excited by the laser beam, *i.e.* the size of the NC measured through its emitted

Figure 22 – a) Scanning luminescence image of a 11 × 11 μm^2 region of the sample. The dashed yellow crossed lines are centered on the position of NC3 and represent the selected data for obtaining the spatial resolution of the optical setup in the x and y directions. Gaussian fitting of the intensity profiles from NC3 for b) x-axis and b) y-axis resulting on $FWHM_x =$ 677 nm and $FWHM_y =$ 704 nm, respectively, as represented by the double headed arrows.

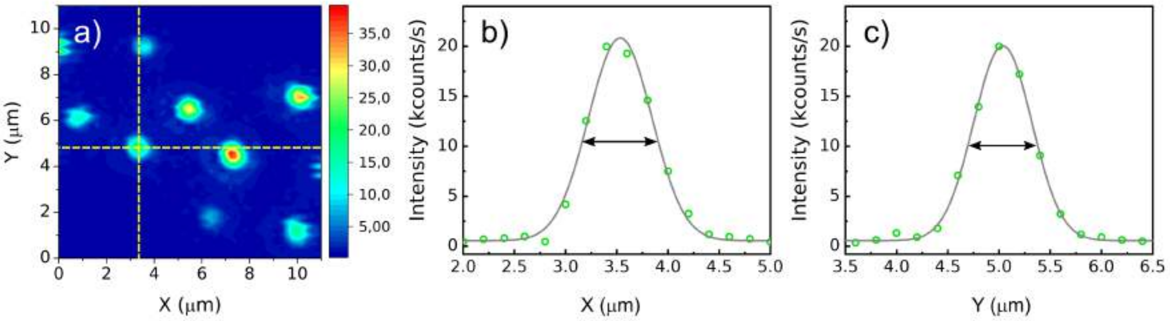

Font: The author (2022)

luminescence is at least the same of the collimated laser beam at the focal spot. Thus, by considering the Equation 2.32, with $N.A. =$ 1.25 and $\lambda =$ 977 nm, a theoretical estimate results in $FWHM \simeq$ 400 nm. This theoretical transverse resolution is 57 $\%$ smaller than the experimentally measured value. This difference may be due to the fact that the theoretical calculations performed with Equation 2.32 consider a perfectly punctual light source, which is not our case since the laser light is emitted from an optical fiber with diameter of 7 μm. Besides, the size of the investigated NCs are on the order of the theoretical estimates, which means that in a sample scan over a given particle, the luminescence from an individual NC is detected over the whole NC diameter plus the diameter of the focused excitation beam. In other words, even if the real diameter of the focused beam was given by the theoretical calculated value, say 400 nm, a 150 nm particle would be detected as having at least 550 nm in diameter.

The difference between the measured optical resolution and the theoretical estimate may also be influenced by the use of a finite corrected objective lens. In this optical design, the light from a source is collected by the objective and focused down to a spot, being projected onto an eyepiece or optical sensor (camera, APD, photomultiplier, *etc.*) at a given distance. In other words, the light collected by a finite conjugate objective is not collimated at the output. For the specific objective used in this chapter, the optimal distance between the objective lens and the eyepiece or detector is of 150 mm. As the optical path between the objective and the detection system is of about 1.2 m, there is a divergence of the luminescence beam before it is focused by an ordinary lens and projected into the sensitive area of the APD or spectrometer. It leads to a non ideal focusing of the luminescence beam on the detectors, causing a degradation of the measured optical resolution of the optical system. In addition, the alignment of the system is very critical for such experiments and the theoretical model does not consider any optical aberration produced by other optical components, such as lenses, color filters, *etc.*. Thus, from now on, the experimentally obtained value for $FWHM$ will be defined as the spatial resolution of the optical system, being fundamental for obtaining the excitation power density used in the experiments, discussed next.

The spatial resolution of the optical setup is correspondent to the diameter of the laser spot size at the focal plane, which can be used to obtain the power density at the sample through the equation

$$\mathcal{P} = P/A = P/[\pi \times (FWHM/2)^2], \tag{3.1}$$

where P is the average power of the excitation beam and A is the area of the focal point assumed here to have a circular symmetry [15]. For instance, the pump power density used to obtain the scanning luminescence image shown on Figure 19 was $\mathcal{P} = 6\times10^3$ W/cm^2 at the sample and was obtained by measuring an average power of $P \simeq 21$ μW above the sample.

This method of determining the pump power density was used to perform the saturation studies on an individual NC. The emission spectrum of the green transitions of the NC4 was obtained and can be seen on Figure 23a). It can be noticed the presence of several peaks around 525 nm, 540 nm, 550 nm and 565 nm. As reported by Galvão *et al.* on their study with the same nanoparticles [24], it can be verified that the main peaks at 525 nm and 540 nm are correlated when the temperature of the system arises. The same result was obtained by analyzing the correlation between the multiple peaks around 550 nm and at 565 nm upon temperature changes [24]. Thus, the emission bands ranging from 518 nm to 543 nm, labeled on Figure 23a) as the interval between λ_1 and λ_2, respectively, were assigned as being related to the ^{2}H$_{11/2}$ $\rightarrow$ ^{4}I$_{15/2}$ transition of the Er^{3+} ion; while the emission bands ranging from 543 nm to 570 nm, labeled as λ_2 and λ_3, respectively, were associated to the ^{4}S$_{3/2}$ $\rightarrow$ ^{4}I$_{15/2}$ transition. The two vertical lines on Figure 23 indicate the center wavelengths for both sets of transitions and are located at 528 nm and 559 nm [11].

The luminescence intensity I of each electronic transition is related to the pumping power density by

Figure 23 – Luminescence spectra of the green emissions for a single $Yb^{3+}/Er^{3+}:Y_2O_3$ NC at 298 K (blue line) and 323 K (red line). On a), the vertical dashed lines represents the wavelength intervals given by $\lambda_1 = 518$ nm, $\lambda_2 = 543$ nm and $\lambda_3 = 570$ nm and the green solid lines represents the center wavelengths at 528 nm and 559 nm to indicate the set of transitions $^2H_{11/2} \rightarrow {}^4I_{15/2}$ and $^4S_{3/2} \rightarrow {}^4I_{15/2}$, respectively. Both spectra were obtained under an excitation power density of 64.2 W/cm^2 . On b), the integrated emission intensity of the transitions $^2H_{11/2} \rightarrow {}^4I_{15/2}$ (λ_1 to λ_2, circles) and $^4S_{3/2} \rightarrow {}^4I_{15/2}$ (λ_2 to λ_3, triangles) is shown for various pump powers in a bilogarithmic scale. The slopes of the fitted curve are given by $n = 1.8 \pm 0.1$ indicating that the transitions are excited via a non-saturated two-photon process.

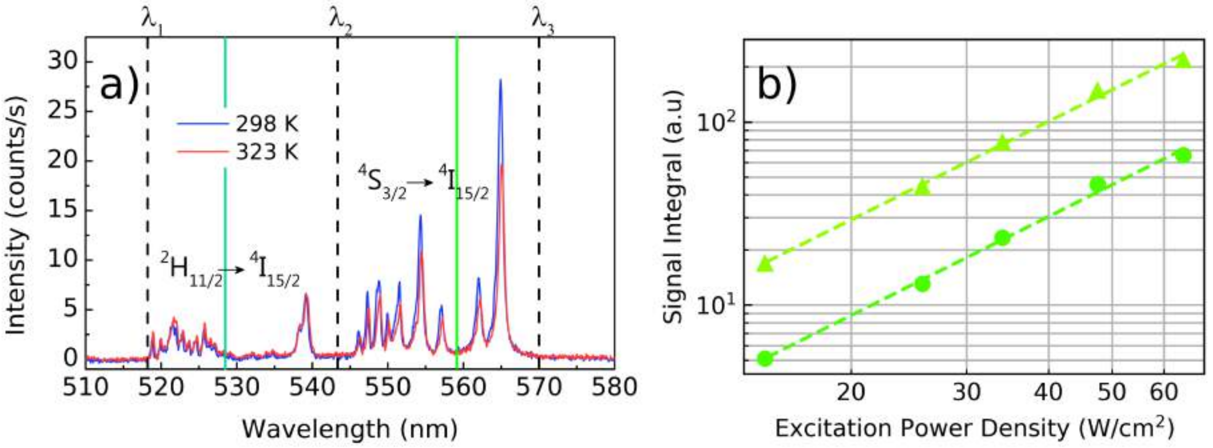

Font: Adapted from [11]

$$I \propto \mathcal{P}^n, \tag{3.2}$$

where n is defined as being the number of photons involved in the UC process. The method used for measuring the $\mathcal{P}$ values was detailed in the previous paragraph and $I(\mathcal{P})$ was obtained by integrating the emission spectrum of the NC4 over the intervals λ_1 to λ_2 and λ_2 to λ_3, which corresponds to the two aforementioned green transitions of Er^{3+}. A bilogarithmic fitting function is then used on $I(\mathcal{P})$, returning the value of n. The saturation measurements correspondent to the $^2H_{11/2} \rightarrow {}^4I_{15/2}$ and $^4S_{3/2} \rightarrow {}^4I_{15/2}$ transitions were performed for the NC4 and can be seen on Figure 23b) for pumping powers ranging from 12.0 W/cm^2 to 64.2 W/cm^2. The fitted function for both transitions returned a value of $n = 1.8 \pm 0.1$, indicating that the radiative decay from the $^2H_{11/2}$ and $^4S_{3/2}$ states arise from two-photon absorption processes, as expected for energy UC involving these specific transitions of Er^{3+} . The measured n indicates that saturation effects can be neglected in this excitation power range, *i.e.*, the thermal characterization of the system should be not compromised by performing the LIR measurements within the chosen power density regime [11]. Thus, a power density of 64.2 W/cm^2 was chosen to carry on the thermometric measurements, with a total integration time of 60 s for the data acquisition of each emission spectrum. Despite being less intense due to the presence of thermal effects (see Equation 2.3), the $^2H_{11/2} \rightarrow {}^4I_{15/2}$ transition becomes more prominent as the temperature of the system rises, allowing LIR measurements to be made even in the chosen pumping regime, as shown on Figure 23a) for the measured spectra of a single NC at 298 K and 323 K.

3.5 THERMAL RESPONSE OF INDIVIDUAL NCS IN DIFFERENT MEDIA

As discussed in the previous section, the saturation study performed on the NC4 allows to work in a non-saturated pumping power regime. Hence, in this regime, it is possible to characterize the four selected NCs through LIR technique and investigate the thermal response of the selected nanothermometers in different media. The main purpose here is to perform the LIR measurements over the same luminescent NCs on three different environments: air, water and ethylene glycol. The reasons to choose these specific surrounding media will be clear soon. As one can imagine, the task of working with the single nanothermometers on liquid environments in a situation where the NCs are not bonded to the surface is not a simple task. Thus, in order to carry on the experiments it was established a protocol to deposit liquids in a controlled manner over the coverslip and is described as follows. As mentioned before, the sample containing the nanothermometers is basically composed by a coverslip in which a set of NCs are deposited over the glass surface. The experimental apparatus makes it possible to identify a region with a convenient spatial distribution of five individual NCs embedded in air, as discussed previously. Then, a droplet of 100 μL of distilled water is carefully deposited over the sample with a micropippete. Before performing the thermal measurements on water, it is assured that the NC constellation has the same pattern observed in air which must, for instance, remain the same regarding the relative emitted intensities of each particle and the average distance between them. It can be verified on the luminescence scanning images shown on Figure 24a) and b) in which are presented the same selected NCs presented on Figure 21. Only when the particles are identified and confirmed to be the same ones than those on air, the LIR measurements of the selected NCs on water are started. As the temperature raises, the water droplet evaporates. This effect is even fast for temperatures higher than 305 K [11]. It is thus necessary to refill the main droplet with additional 30 μL of water and wait for a thermal stabilization for every measurement at each new temperature value. A big problem arises when the main water droplet dries, generating a "coffee sludge" effect that may agglomerate the NCs, making it impossible to distinguish the individual NCs from larger agglomerates.

Once the LIR measurements are finished in water, the samples temperature is reduced to the room temperature (between 293 K - 295 K) and the water is left to evaporate naturally. This method avoids the agglomeration effect caused by fast water evaporation and allows one to find the same spatial distribution of single NCs in air again, which is confirmed by subsequent luminescence scanning images as shown on Figure 24a). After the water evaporates, the LIR measurements are performed in air. Once the measurements are performed in air, a droplet of 100 μL of ethylene glycol is carefully deposited over the sample. After the liquid deposition, a scanning luminescence image of the NCs is obtained and when the luminescent pattern is retrieved, the LIR measurements are performed again on each NC in this medium. Due to the slow evaporation of the ethylene glycol the sample does not need to be refilled [11].

Figure 24 – Emission patterns of the five selected NCs, indicated by the white arrows and their corresponding numbers, in three media: a) air (but after the evaporation of the water, from the thermometric LIR measurements with the NCs embedded in this medium), b) water and c) ethylene glycol. Notice that the NC spatial profile keeps its distribution in each medium, in such a way that the data collected always refer to the same NCs.

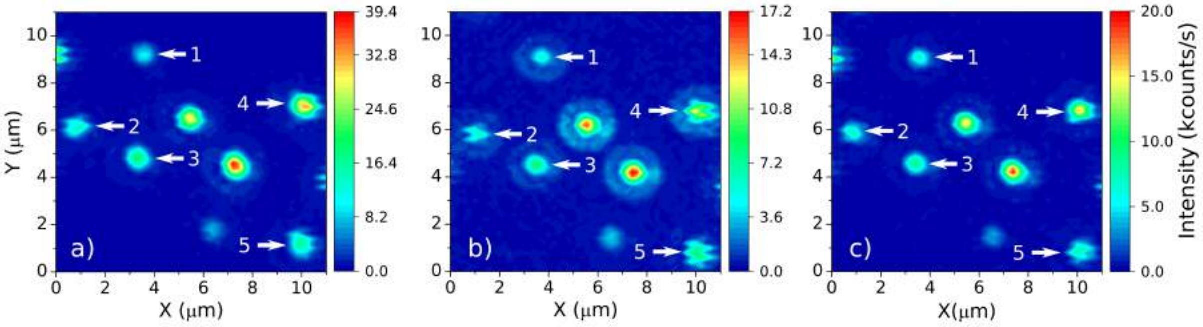

Font: Adapted from [11]

Having discussed how the steps necessary for performing the thermal calibration of the system, along with the description of the methods that allow the LIR measurements to be carried on over the same single NCs on different environments, now we can turn our attention to the obtained LIR results and present the correspondent relevant discussions, as will be shown on the next section.

As discussed in the subsection 2.1.4, the two Er^{3+} energy levels ^{2}H$_{11/2}$ and ^{4}S$_{3/2}$ are close enough in energy for the thermal coupling between them be relevant. Therefore, as the occupation probability distribution for the two thermally coupled states follows the Maxwell-Boltzmann statistics, the LIR defined on Equation 2.5 can be rewritten as

$$ln(R) = \beta - \frac{\alpha}{T}, \tag{3.3}$$

in which $\beta = ln(A)$ and $\alpha = \Delta E/k_B$. Here, α is given in units of temperature, while β is a dimensionless parameter. With the definition of these two new parameters, the efficiency of each ratiometric luminescent nanothermometer, given by the relative sensitivity S_R^{LIR}, can be written as (see Equation 2.25)

$$S_R^{LIR} = \frac{\alpha}{T^2}, \tag{3.4}$$

where S_R^{LIR} has dimension of $\%$ K^{-1} and is useful to compare the thermal sensitivity of each NC on the different media.

For the three aforementioned environments, the LIR measurements were performed in a temperature range from 293 K to 323 K. This temperature interval was spanned in 10 steps, according to the temperature monitoring procedure discussed on the previous paragraphs. For each temperature value, the emission spectra was acquired for one particle at a time until the five particles be characterized. The LIR values are then obtained as the ratio between the numerical integrated intensities of the spectra in the wavelength intervals [λ_1,λ_2] and [λ_2,λ_3] [see Figure 23a)], in the form

$$R = \frac{I_1}{I_2} = \frac{\int_{\lambda_1}^{\lambda_2} I(\lambda)d\lambda}{\int_{\lambda_2}^{\lambda_3} I(\lambda)d\lambda}, \tag{3.5}$$

where $I(\lambda)$ is the numerical emission intensity value as a function of the wavelength λ. Equation 3.5 is then used to acquire the raw data for the LIR values at each temperature. Equation 3.3 is subsequently applied to obtain the α and β parameters by fitting the LIR data as a function of temperature .

The LIR results for the five particles in air, water and ethylene glycol can be seen on Figures 25a), b) and c), respectively. For the sake of simplicity, the results are summarized in Table 1 along with the average values measured over the set of five NCs. By using the method discussed on section 2.3.1, the error values for the individual particles were directly extracted from the data fits and the average errors over the set of NCs were taken as being the standard deviation of the measured quantities [11].

When considering the central wavelengths of the two investigated transitions, at 528 nm and 559 nm from the absorption spectrum or diffuse reflectance of the samples one can measure the spectroscopic energy gap ΔE_{spec} between the two coupled energy levels and obtain a value of $\Delta E_{spec} = 1050$ cm^{-1} [24]. It can be noticed that the effective gap energy $\Delta E = \alpha k_B$ measured with the particles in air return values larger than ΔE_{spec} for individual

Figure 25 – LIR thermometry measurements performed in a) air, b) water and c) ethylene glycol as a function of inverse of the temperature. The solid lines are the linear fits used to determine α and β from the data corresponding to the particles 1 (blue circles), 2 (orange stars), 3 (green triangles), 4 (pink diamonds) and 5 (brown squares).

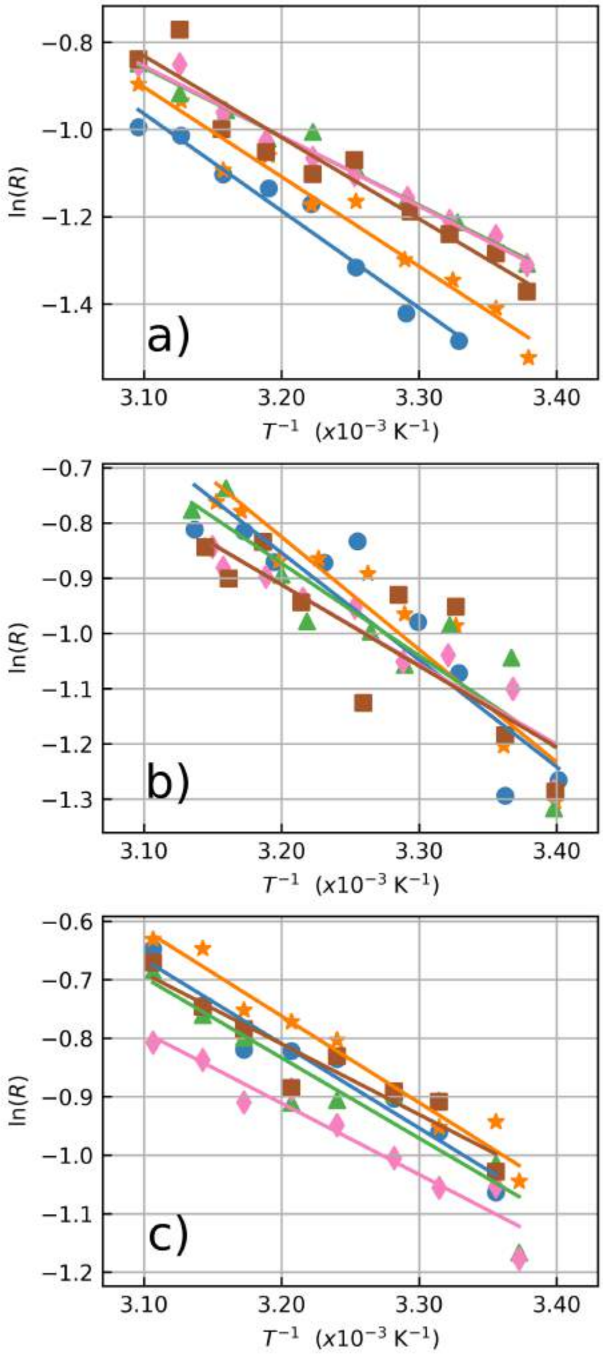

Font: Adapted from [11]

particles and for the average values over the five NCs. It is remarkable the difference between ΔE_{spec} and the measured energy gap for the individual particles, as can be seen on the results obtained for the NC1 in air, given by $\Delta E =$ (1550 ± 120) cm^{-1}. Besides, the values presented here are greater than the measured values reported on reference [24] for the same

Table 1 – Measured parameters for the five selected particles extracted from linear fittings to experimental data by using Eq. 3.3. Here $\Delta E = k_B\alpha$. The S_R and δT values are given at 310 K.

NP	Air				Water				Ethylene Glycol			
	ΔE (cm^{-1})	β	S_R ($\%$ K^{-1})	δT	ΔE (cm^{-1})	β	S_R ($\%$ K^{-1})	δT	ΔE (cm^{-1})	β	S_R ($\%$ K^{-1})	$\delta T(K)$
1	1550 ± 120	5.9 ± 0.6	2.3 ± 0.2	0.6	1350 ± 220	5.3 ± 1.1	2.0 ± 0.3	1.4	1001 ± 97	3.8 ± 0.5	1.5 ± 0.2	0.8
2	1427 ± 95	5.5 ± 0.4	2.1 ± 0.1	0.6	1420 ± 180	5.7 ± 0.8	2.1 ± 0.3	1.1	1028 ± 77	4.0 ± 0.4	1.6 ± 0.1	0.6
3	1095 ± 48	4.0 ± 0.2	1.6 ± 0.1	0.4	1160 ± 220	4.5 ± 1.0	1.7 ± 0.3	1.7	950 ± 160	3.6 ± 0.7	1.4 ± 0.2	1.4
4	1116 ± 52	4.1 ± 0.2	1.7 ± 0.1	0.4	1000 ± 130	3.7 ± 0.6	1.5 ± 0.2	1.2	846 ± 86	3.0 ± 0.4	1.3 ± 0.1	0.9
5	1300 ± 130	5.0 ± 0.6	1.9 ± 0.2	0.9	1020 ± 260	3.8 ± 1.2	1.6 ± 0.4	2.3	840 ± 120	3.1 ± 0.5	1.3 ± 0.2	1.1
Average	1300 ± 150	4.9 ± 0.7	2.1 ± 0.2	2.5	1190 ± 156	4.6 ± 0.7	1.9 ± 0.2	4.3	934 ± 72	3.5 ± 0.4	1.5 ± 0.1	2.7

Font: Adapted from [11]

kind of particles. This difference can be associated to the different excitation scheme used in their work, like the two orders of magnitude difference in pumping power and the very different bandwidths of the excitation lasers used, which influences the number of ion classes excited within the inhomogeneous broadened absorption line [11]. Meanwhile, other works argue that the thermometer accuracy and performance may also depend on the way that the thermally coupled energy levels are populated, which could lead to inaccurate temperature measurements [24, 23]. In addition, the smaller ΔE at high pumping power densities are usually related to the heating induced by the absorption on NIR photons [26]. As an example, Marciniak *et al.* reported differences on the measured sensitivity values of Er^{3+} -doped NCs by an order of magnitude from low to high pumping regimes with sensitivity values of $S_R^{LIR} = 2.66$ $\%$ K^{-1} to $= 0.28$ $\%$ K^{-1} , respectively [115]. This argumentation is corroborated by the fact that nonradiative transitions for low lying energy levels increase as the energy difference between them decreases, which could lead to a deviation from the Boltzmann's distribution of thermal population between the two coupled states [129]. Pickel and collaborators assume that this deviation from the Maxwell-Boltzmann statistics is the reason for the "apparent" self-heating effects induced by high excitation power densities (above 10^4 W/cm^2) [26]. Their argument is that the temperature artifacts are not result of poor heat dissipation from the nanothermometer to its surroundings, but instead, is induced by the distortion from the thermal population distribution between the ^{2}H$_{11/2}$ energy level due to the MP decay processes from high lying levels. These effects may lead to significant changes in the measured LIR values when dealing with single nanothermometers. In this work, these thermal effects induced by high pumping regimes were avoided by working in a constant power density of 64.2 W/cm^2 as mentioned in the previous section, far below the necessary for the manifestation of the "apparent" self-heating effects [11].

At low power excitation densities, however, the observed effects are the opposite to those previously described. In this regime, the nonradiative absorption rates responsible for populating the high lying energy level due to thermalization are dominant. As mentioned above, Marciniak *et al.* achieved relative sensitivities as high as $S_R^{LIR} = 2.66~\%$ K^{-1} for a power density regime of 25 W/cm^2 [115] which is quite close to the power density regime used in this work. Despite the high sensitivity values obtained in this pumping power regime, it leads to a poor signal to noise ratio and longer integration times when working with single particles which increase the measurement uncertainties. As presented in the subsection 2.3.1, the errors of the measured parameters for individual NCs depend directly on the uncertainties from the signal-to-noise ratio of the detection system. This fact is better seen when discussing the results for the NCs on water and ethylene glycol.

As can be seen in Table 1, the average of the measured values for ΔE in water agrees with the parameters obtained for the particles on air within a standard deviation. These results are in consonance with other reports found in literature [130, 77, 131, 132]. As a matter of comparison, relative sensitivity values up to $S_R^{LIR} = 2.3\%$ K^{-1} at 310 K were obtained. The reported values found on literature for the relative sensitivity obtained with Yb^{3+}/Er^{3+}codoped complexes ranges from 0.3 $\%$ K^{-1} to 2.88 $\%$ K^{-1} at $\approx$ 300 K [115] which makes the NCs investigated here as one of the most sensitive nanothermometers with this combination of Ln^{3+} ions. It can also be noticed larger error values for the NCs embedded in water and ethylene glycol, due to the the larger measurement uncertainties by working with the chosen exciting power regime.

The luminescence signal from the NCs drops to approximately half of its value in air when the liquids are deposited over the sample [compare Figures 19a), b) and c)] which is caused by the increase in the refractive index of the medium surrounding the NCs. This enhances the probability of photon emission through the medium with higher refractive index, reducing the amount of emitted photons that can be collected by the detection system [133]. The measured average decrease in the detected luminescence intensity from NCs in the liquid media were approximately $I_{water}/I_{air} = 0.51$ and $I_{ethylene~glycol}/I_{air} = 0.46$. Thus, a high dispersion of the LIR measurements on each NC can be seen in the presence of liquids [see Figures 25b) and c)]. However, even with larger errors, the thermal response of the NCs in water reinforces the assumption that these NCs are suited for performing nanothermometry on aqueous systems such as biological media which consist in approximately 70 $\%$ of water [11]. This argument is endorsed by other authors [27, 25].

There is a change in aspect when one looks at the measured values of ΔE and S_R^{LIR} for

Figure 26 – Raman scattering spectra of a) water and b) ethylene glycol. The gray shaded regions represents the ranges in which the ΔE were obtained on both environments with the selected NCs. The presence of C - O stretching modes of ethylene glycol ranging from 805 cm^{-1} to 1093 cm^{-1} matches the measured ΔE in this media.

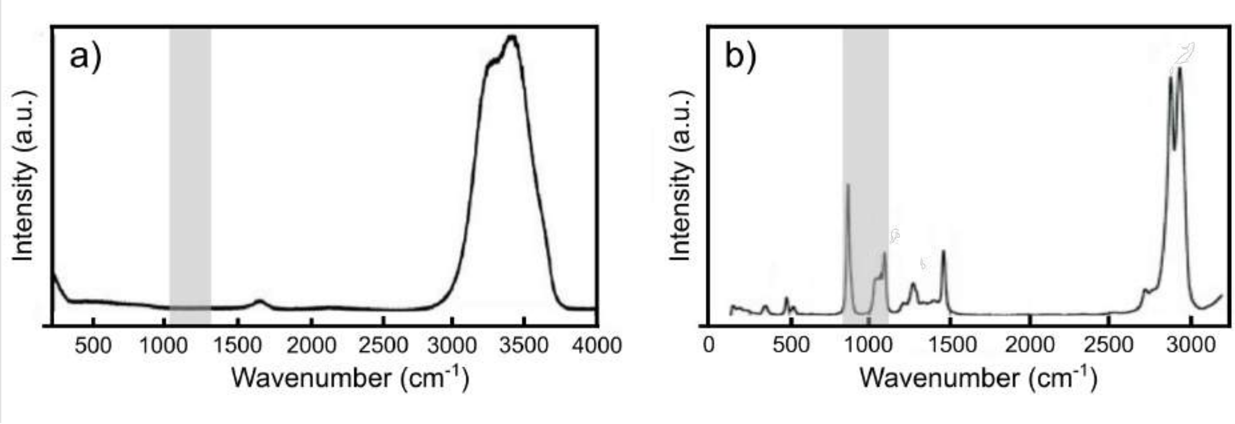

Font: Figure a) adapted from [135] and b) from [134]

the NCs embedded in ethylene glycol. As can be noticed in Table 1 and on Figure 25c), the ΔE measurements for the NCs in this medium are consistently smaller than the obtained for the measurements carried on in air and water. Here, the reduction in ΔE is associated with the influence of strong vibrational modes around 1044 cm^{-1} related to the C - O stretching bond of the ethylene glycol molecules [134]. As presented in subection 2.1.5, when the NCs are embedded in a solvent that presents vibrational modes with energies that are almost resonant with the energy gap between the two thermally coupled states, it leads to a nonradiative decay rate Γ_Q (see Equation 2.9) due to energy transfer from the NC to the solvent. This nonradiative quenching effect is responsible for the depopulation of the higher lying state ^{2}H$_{11/2}$ and changes the population distribution of the thermally coupled states, inducing small ΔE values and consequently, small measured relative sensitivities. This assumption is reinforced by looking at the vibrational Raman spectra for water and ethylene glycol shown on Figure 26. It can be noticed the absence of any vibrational modes of water molecules with energies close to the measured values of ΔE on this medium, represented by the dashed gray area on Figure 26a). The same does not apply for the ethylene glycol, Figure 26b), where there is an overlap of the measured ΔE values in this medium and strong vibrational modes with energies between 805 cm^{-1} to 1093 cm^{-1}.

From the results reported on Table 1, it can be noticed that the averages for ΔE , S_R^{LIR} and δT present larger error values than the measured parameters obtained for the individual NCs. It may lead to a series of consequences when performing measurements with ensembles of nanoparticles. For instance, depending on the synthesis procedure, the NCs can possess high dispersion over several parameters as dopant concentrations, shape, size, surface defects, etc.[46] As will be shown below, intensity luminescence measurements can relate the size of an individual NCs to the distinct measured values for ΔE , which cause a significant difference on the relative sensitivity values for each NC. A consequence of this can be exemplified in an simple application scenario: a sample scanning thermal image performed with an ensemble of NCs can present different temperature readings between adjacent nanothermometers due to the different thermal responses between them. Therefore, the error bars for individual nanothermometers do not contain variations in the thermal response due to dimensional, dopant concentration or defect inhomogeneities which is present in the ensemble average [11].

3.5.1 Individual aspects of the nanothermometrs

Having presented the general features about the measured thermal responses of the nanothermometers embedded in the three different media, it is time to turn our attention to the individual aspects of each NC. At first sight, it can be noticed that each NC presents a distinct thermal response from each other (see Table 1). The differences between the thermal parameters as ΔE and β, for example, are justified as being consequence of the variations in the NC's size [10, 61] caused by micro-strain effects [10] or surface quenching sites [136]. In order to analyze the first possibility, it is possible to make an estimate based on the intrinsic micro-strain in Y_2O_3 microparticles [137] and nanoparticles [138]. The maximum experimentally obtained value for the intrinsic bulk strain, $\varepsilon = \delta V/V$, where V is the volume of the Y_2O_3 crystal, is on the order of $\varepsilon \approx 5 \times 10^{-3}$ [138, 137]. The tensile strain is related to the stress $\sigma =$ force/area by $\sigma =$ elastic modulus $\times\ \varepsilon$. By considering that the elastic modulus (Young, Bulk and Shear) possess a maximum value of $\sim$ 160 GPa [139], one can obtain an estimate of $\sigma \simeq 1.0$ GPa for the inner stress caused by the micro-strain on NCs. Thus, one can compare the stress caused by the intrinsic micro-strain with experimental investigations on microparticles and NCs under high pressure regimes. Despite no specific studies relating the intrinsic stress and emissions in our system can be found in the literature, there are a few reports on other yttrium-based systems codoped with Yb^{3+}/Er^{3+}. For instance, recent published studies performed on YVO_4:Yb^{3+}/Er^{3+} NCs [140] and YF_3:Yb^{3+}/Er^{3+}microparticles [141] reported no significant changes on the LIR of the green emission bands under external stress up to 10.0 GPa. This result is one order of magnitude higher than the micro-strain estimate for the NCs studied in this work, which indicates that the micro-strain effects does not play an important role in our LIR signal and, thus, have no significant contributions to the differences between the thermal parameters of single NCs.

The second possible explanation for the distinct thermal responses between the individual nanothermometers is the size-dependent quenching effects. The dependence of LIR on the size of Ln^{3+} -doped emitting NCs were already reported in several works [29, 10, 25, 61]. For instance, NCs composed by $LiLaP_4O_{12}$ codoped with $Yb^{3+}/Er^{3+}$and Cr^{3+}/Nd^{3+} present changes in their relative sensitivities from 1.1 $\%$ K^{-1} to 2.1 $\%$ K^{-1} for the first compound [10] and from 1 $\%$ K^{-1} to 5 $\%$ K^{-1} for the last one [61] by varying the NCs' size. Both works investigated the sensitivities of NCs with sizes ranging from 20 nm to 240 nm, with the higher sensitivities obtained for the smaller particles. The physical mechanisms responsible for this dependence on size rely on the optical quenching caused by the energy adsorbed by ions located at the surface of the NC and its fast nonradiative decaying rates. The participation of the surface ions relative to those located within the NC is inversely proportional to the radius of the NC [10]. These surface sites have different spectroscopic features when compared to those "bulk" ions such as the presence of absorption bands and lack of emission for some selected sites [142, 143]. Therefore, it is assumed that beyond the already known decay processes in small NCs as nonradiative phonon assisted quenching and cross relaxations processes, the surface-related nonradiative quenching can occur. Further evidence for the relevance of these surface-related mechanisms in our nanothermometers is given below.

Specifically looking at the relative sensitivity values in air reported on Table 1, it can be noticed that the more and less sensitive nanothermometers were the NC1 and NC3 with $S^{LIR}_{R(1)} = (2.3 \pm 0.2)$ $\%$ K^{-1} and $S^{LIR}_{R(3)} = (1.6 \pm 0.1)$ $\%$ K^{-1}, where the subscript (i) denotes the NC number. In water, these extreme values are given by $S^{LIR}_{R(2)} = (2.1 \pm 0.3)$ $\%$ K^{-1} and $S^{LIR}_{R(4)} = (1.5 \pm 0.2)$ $\%$ K^{-1} being, as said before, equivalent to those obtained in air within the experimental error. In ethylene glycol, the maximum and minimum sensitivity values are given by $S^{LIR}_{R(1)} = (1.6 \pm 0.2)$ $\%$ K^{-1} and $S^{LIR}_{R(5)} = (1.3 \pm 0.1)$ $\%$ K^{-1}. The values of relative sensitivity are very similar for all nanothermometers in this last medium considering the measured uncertainties. The small variation of sensitivity values in ethylene glycol among all studied NCs should be associated with the surface effects associated with the molecular vibrational modes of this solvent, which were not present in the two other studied media (air and water) [11].

The thermal resolution δT for the individual nanothermometers (see section 2.3) for the

Figure 27 – Bilogarithmic plots for a) ΔE , b) β and S_R for particles 1 (blue circles), 2 (orange stars), 3 (green triangles), 4 (pink diamonds) and 5 (brown squares) in air as function of the total NC luminescence intensity under 6 × 10^3 W/cm^2 of excitation power density at the NC. The red lines have a slope of ≈ -0.3 for all three parameters. Since $I \propto$ volume $\propto$ r^3 , the slope of -0.3 indicates that these parameters vary according to $1/r$, which is proportional to the surface/volume ratio

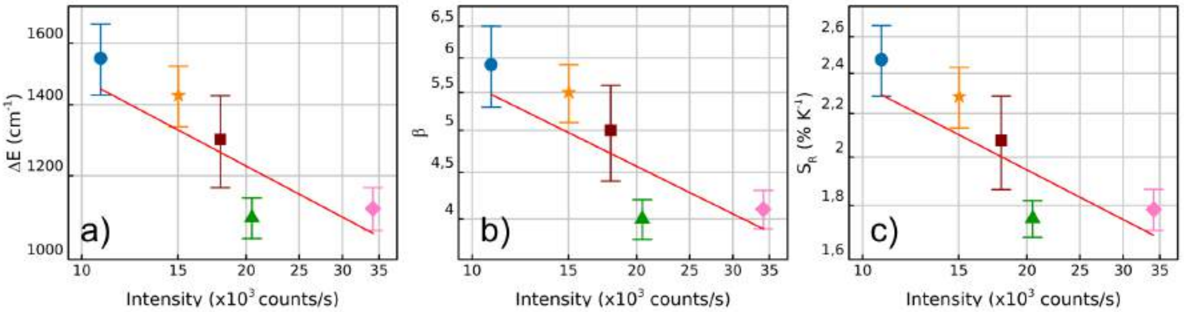

Font: Adapted from [11]

five NCs at 310 K are given on Table 1 and determine the minimum change in temperature the sensor is able to reliably detect. The most precise nanothermometers in air were the NC3 and NC4, with $\delta T \sim$ 0.4 K. On water and ethylene glycol, the smaller thermal resolutions were measured for the NC2 and are given by $\delta T =$ 1.1 K and $\delta T =$ 0.6 K, respectively. As discussed in the subection 2.3.1, the thermal resolution depends not only on the relative sensitivity values, but also on the measured uncertainties of α and β extracted from the fitting of the LIR data which are higher for the two liquid environments, leading to high δT values. The thermal resolution defined for the ensemble measurements, that considers the standard deviation from the average value of the averaged parameters, results in worse thermal resolutions, as poor as 4.3 K. This difference can be explained by the large distribution of measured values for ΔE and β parameters for the five NCs, which lead to high standard deviations calculated from the experimental data [11]. The typical values of thermal resolution for ensembles of UC Ln^{3+} -based NCs ranges from $\delta T \sim$ 1.0 K to 0.1 K [44]. It means that the measured δT values obtained for the individual NCs reported here are in agreement with the recent advances on LIR-based nanothermometry.

It is curious that in the three investigated environments, the most sensitive nanothermometers, *i.e.* the nanothermometers with higher S_R^{LIR} and smaller δT were the NCs 1 and 2 which in turn are the emitters with the less intense detected luminescence. We associate this result to the manifestation of surface effects as a function of the NC size. The reason for this relies on the similar trend obtained for the dependence of the measured values ΔE , β and S_R^{LIR} with the detected luminescence intensity I in air for each NC, as shown on Figure 27. The relation of this dependence of I on the NC's size is explained as follows. Here, it is a fact of great importance that the particles used in this experiment have diameters ranging from 70 nm to 150 nm. As shown on section 3.1, the synthesis route used to incorporate the Ln^{3+} ions into the NCs leads to a homogeneous dispersion of the fluorescent sites over the crystal volume. Since the number of luminescent ions grow with the NC volume, it is expected that $I \propto r^3$, where r is the NC radius. In this sense, the luminescence intensity is a proxy for an *in situ* NC radius measurement. By plotting the measured results in a bilogarithmic scale, it can be noticed that the results present a linear dependence of all measured parameters on the luminescence intensity with a slope of -0.3. This behavior is associated to surface quenching effects which depend on the number of the quenching sites relative to the ions inside the volume, named "bulk" ions. This ratio is given by the surface/volume ratio that, for a spherical particle, is proportional to $1/r \propto I^{-1/3}$. Therefore, the larger surface-to-volume ratio, the higher will be the measured ΔE between the thermally coupled levels and consequently the S_R^{LIR} values.

The interpretation of the dependence of the β parameter can be discussed by looking at its definition as $ln(A)$, where A was defined on Equation 2.7 and can be written in the form

$$\beta = ln(A) = ln\left(\frac{\tau_1^{rad}\lambda_1}{\tau_2^{rad}\lambda_2}\right), \tag{3.6}$$

where τ_i^{rad} and λ_i are the radiative decay lifetimes and the wavelengths of the two thermally coupled states and $i = 1, 2$ for the high and low lying energy states, respectively. Hence, the dependence of β on I can be related to the dependence of the $^4S_{3/2}$ lifetime with size in this kind of codoped systems as reported on references [136, 144]. Both works report on experimental measurements on Yb^{3+}/Er^{3+}codoped NCs and show that the $^4S_{3/2}$ mean lifetimes become shorter with the reduction of the NCs diameter. Zhao and collaborators [136] justify the size dependency of the lifetimes due to the presence of surface quenching effects with the mean decay rates presenting a linear dependence on the surface/volume ratio [136]. However, the size dependency of the surface quenching discussed on the last two paragraphs is still a matter of debate. Further investigation needs to be carried on in order to better understand this phenomenon. Therefore, these results indicate that the individual characteristics of these luminescent nanothermometers are particularly important when working with NCs at an individual level and bring up some effects which are not considered so far when working with ensemble measurements.

A possible application of the simple relation extracted from the dependencies between the thermal parameters and the luminescence intensity presented on Figure 27 is that, in principle, the thermal calibration of several NCs can be done through the calibration of just one nanothermometer. This could be done by measuring ΔE , β and S_R^{LIR} values for one NC and then interpolate these values with the information about its luminescence intensity to other particles with the general dependence of $I^{-1/3}$. This result could reduce significantly the amount of work needed for the characterization of several individual NCs on a sample [11].

In this chapter, the experimental investigations on the influence of the environment on the thermal response of individual LIR-based nanothermometers were presented and discussed. The results show that the different Yb^{3+}/Er^{3+}-codoped NCs have distinct thermal responses, as confirmed through the measurements of their effective energy gap, relative sensitivity and thermal resolution. These individual features remain even when analyzing the thermal responses of the same NCs in three different media. However, despite the experiments indicate that the measured thermal parameters ΔE , S_R^{LIR} in air and water are similar within the experimental error (up to $S_R^{LIR} = 2.3$ % K^{-1}), the parameters obtained for the NCs in ethylene glycol are smaller than for the other two environments (with maximum $S_R^{LIR} = 1.6$ % K^{-1}). This is explained through the energy transfer from the thermally coupled energy levels of the Yb^{3+}/Er^{3+}ions to vibrational modes of the ethylene glycol, a typical characteristic of NC-solvent interaction. Another interesting point about the presented results was the relation between the emission intensity from the NCs and the measured values for ΔE , S_R^{LIR} and β which indicates a dependence of these parameters with the surface/volume ratio of the NCs. These results reinforces the assumption that the individual characteristics of Ln^{3+} -doped LIR nanothermometers, as size and interactions with the surrounding medium, must be taken in account for the implementation of these NCs in realistic application scenarios.

4 NANOTHERMOMETRY WITH SINGLE NV$^-$ DEFECTS ON NANODIAMONDS

The precedent chapter was focused on reporting the results and relevant discussions about the individual thermal responses of single lanthanide ion doped nanothermometers and consequences of their interaction with the surrounding medium. All measurements reported there were based on the so-called LIR technique, commonly applied for luminescence nanothermometry. However, as introduced on section 2.2, there is another possibility for performing high-precision luminescence nanothermometry: the ODMR technique with NV$^-$ defects on diamond. Therefore, the current chapter is dedicated to reporting the experimental study on real-time ODMR-based nanothermometry with single nitrogen-vacancy defects on nanodiamonds. The chapter begins by presenting the main characteristics of the studied nanodiamonds along with the details on sample preparation, followed by the description of the experimental setup used for detecting single light emitters. In the sequence, the necessary methods for performing real-time ODMR-based temperature measurements are introduced. Then, the characterization of individual nanothermometers are presented. The chapter is concluded with the results presenting the temperature monitoring of a sample performed with a single NV$^-$ defect on a nanodiamond. Until the date of submission of this Thesis, this is first time that experiments on nanothermometry with individual NV$^-$ defects are reported.

4.1 NANOPARTICLES AND SAMPLE PREPARATION

The nanoparticles (Microdiamant AG, quantum particles QP25) chosen for performing the thermal studies reported in this chapter have an average diameter of 25 nm and contain zero, one or two NV$^-$ defects. The nanodiamonds were deposited over an antenna, as depicted on Figure 28. The antenna was manufactured using photolithography to pattern a photoresist on a 18×18 mm^2 glass coverslip by sputtering 5 nm of chromium, 180 nm of gold, followed by the deposition of a cover layer with 5 nm of chromium [145]. The details on the deposition of nanodiamonds over the antenna surface are described below.

Similar to the experiments described in the previous chapter, the studies reported here on nanothermometry were performed with individual NCs. Again, a careful cleaning of the surface where the diamonds are deposited is of fundamental importance. Unlike the sample preparation method described previously, in this case the glass coverslip contains a metallic structure deposited on and just a small area where the diamonds can be detected [see Figure 28a)]. Thus, the use of piranha solution was adopted as being the method for cleaning the antennas and is described as follows. This solution is a mixture of concentrated sulfuric acid (H_2SO_4) and hydrogen peroxide (H_2O_2) in a ratio of 7:3. It must be prepared in a glass beaker because the reaction involving the two liquids is highly exothermic. Care must be taken to mix the liquids and place the antenna in the solution. The solution used for cleaning the antennas was composed by 140 mL of H_2SO_4 and 60 mL of H_2O_2. First of all, the mixture is done by slowly placing the hydrogen peroxide on a beaker containing sulfuric acid. The antennas must be placed inside the mixture immediately after preparing the solution to profit from the reaction. Ten minutes are enough to remove any organic impurities. After this, the antennas were rinsed with deionized water (Milli - Q™ with resistivity of ~ 18 MΩ cm) in three different beakers, during about 3 minutes on each. The subsequent drying of the antennas with a nitrogen flow concludes the cleaning method and the nanodiamonds can finally be deposited over the antenna's surface.

Figure 28 – a) Schematics of the antenna used in the experiment. The golden region indicates the region where the chromium and gold layers were deposited; the white trails indicates the location where the nanodiamonds (red hexagon) can be detected. The dimensions of this scheme are out of scale. The antenna was made by photolithography to pattern a photoresist on a glass coverslip. b) Close photograph of the antenna holder. The image shows the deposited metallic pattern and the contacts soldered to the antenna terminals. Two SMA connectors are welded on the holder for in and out coupling the microwave signal necessary for performing the ODMR measurements.

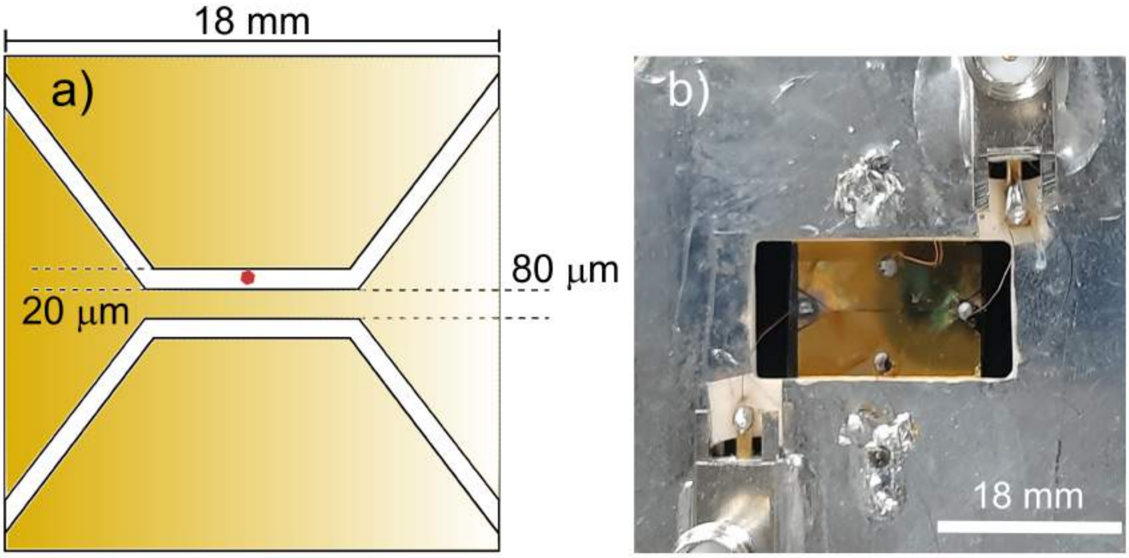

Font: The author (2022)

The deposition of the nanodiamonds over the surface is is done *via* spin-coating method. The nanodiamonds come in a suspension with unknown concentration. After placing a vial containing the nanodiamond suspension in a ultrasonic bath for at least 10 minutes - in order to avoid the formation of agglomerates - a droplet containing 10 μL is held with a micropippete and deposited over the antenna. Then, the antenna is placed on the spin coater (Chemat Technology inc., KW-4A) and rotated in two steps, for 6 s at 2000 RPM and then 15 s at 3200 RPM. This process finish the sample preparation. All the procedures mentioned in this section are of fundamental importance for obtaining samples with a good distribution of nanodiamonds, as shown on section 4.3.

4.2 EXPERIMENTAL SETUP

The experimental setup assembled for the nanothermometry experiments, based on the detection of individual defects on nanodiamonds, consists of a confocal scanning microscope, whose details are described in section 2.4.2; associated with a HBT interferometer which allows to detect the individual emitters. In this setup, the excitation light source is a polarized CW laser emitting at 532 nm (Shanghai Laser & Optics Century, GL532T3-200). A half-wave plate and a polarizer control the laser power. The laser beam is then reflected by a dichroic mirror (Semrock FF562 DI03) and reaches the inverted microscope. The light is tightly focused in a diffraction limited spot on the sample's surface by a high numerical aperture lens (Olympus, UPlanSapo 100×/1.4) which is also used to collect the emitted luminescence from the NV$^-$ defects. Once a nanodiamond is detected, its emitted luminescence (between 600 nm to 800 nm wavelength) is collected through the objective and sent to the detection path after being filtered by the dichroic mirror and a longpass filter (Semrock, FF01-593/LP), used here to ensure the elimination of any laser light. A spatial filter, characteristic of the confocal scheme, is placed in the detection path. It is composed by two lenses and pinhole with 25 μm diameter responsible for blocking the light coming from perifocal regions of the sample. This filter is the key piece for obtaining the high resolution images of the nanodiamonds with low background, as discussed on subsection 2.4.2. The luminescence light can be directed to a high sensitivity CCD camera for alignment and calibration purposes [145].

In order to determine which emitters are individual, the detection system can be configured as a HBT interferometer that allows one to record the second order correlation function $g^{(2)}(\tau)$ of the detected luminescence by means of a Time-Correlated Single Photon Counter (TCSPC) module (PicoQuant, TimeHarp200). This device is responsible for measuring the temporal difference between one arrival photon in one APD and another photon detected by a

Figure 29 – Representation of the experimental setup depicting the inverted sample-scanning confocal optical microscope used in this chapter. P: polarizer; $\lambda/2$: half-wave plate; FBS: flip 50:50 beam splitter; APD: avalanche photodiode; N.A.: high numerical aperture lens; MW: microwave. TCSPC: time-correlating single-photon counter; The selected excitation source is a polarized CW laser with 532 nm wavelength. The emitted luminescence at wavelengths between 600 nm to 800 nm is collected by the same objective lens and separate form the excitation light by a longpass filter with cutoff wavelength of 59. After the light is spatially filtered by a pinhole, the luminescence is sent to the detection apparatus.

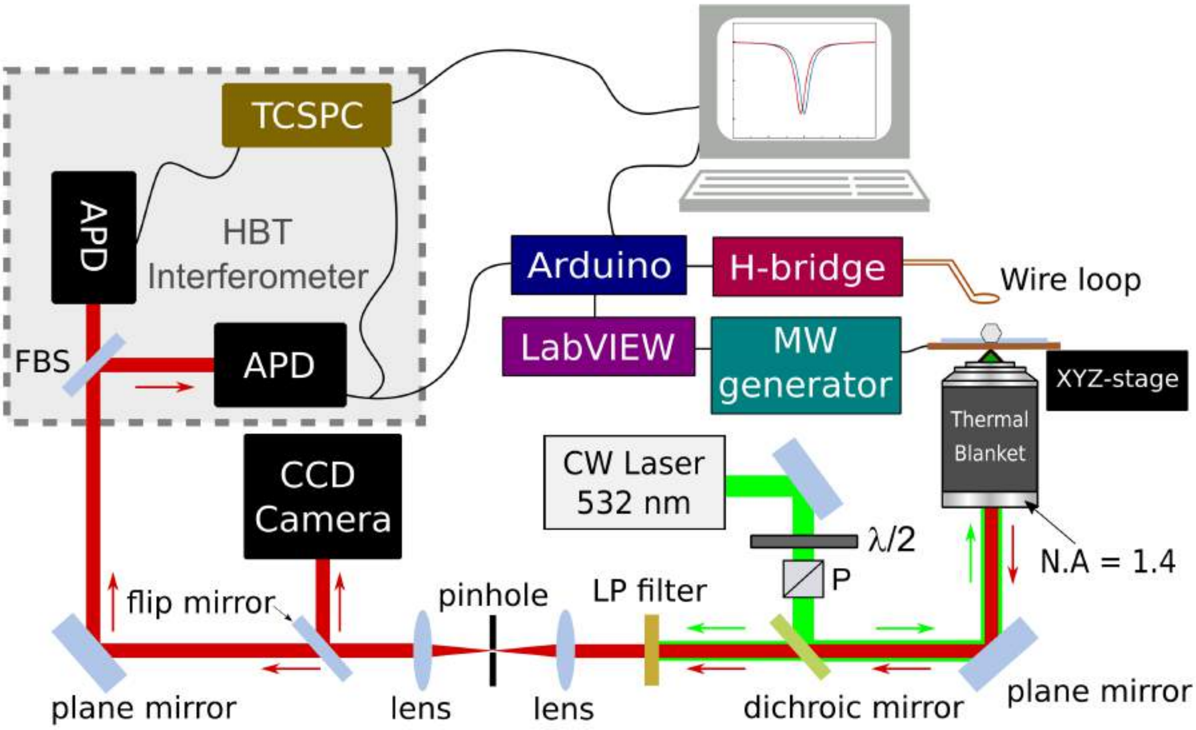

Font: The author (2022)

second APD. The HBT interferometer can be chosen by lifting the flip mounted 50:50 beam splitter. With the flip beam splitter down, the light is directed to a single APD, allowing the construction of scanning luminescence images, in the same way described on section 3.3. In this configuration, the Transistor-Transistor-Logic (TTL) electrical signal from the output of APD is sent to an Arduino board that has a microcontroller, programmed to perform different tasks that makes it possible to use the system for nanothermometry purposes. This system was already used for nanomagnetometry experiments and is described in detail on references [83, 87]. In summary, the microcontroller implements an Arduino Duo board as the control device and its operation is based on the recognition of the TTL pulses coming from the APDs whereby an analog circuit was designed to adequate the pulse width and intensity to the TTL standard. This microcontroller is associated to another Arduino-controlled device that incorporates a bipolar home-made current source (H-Bridge), a device that feeds a wire loop allowing the generation of magnetic field square pulses in alternating senses, which is

Figure 30 – a) Photograph of the experimental apparatus showing the system used for monitoring the ESR frequencies of NV$^-$ defects. Four coils are responsible for generating bias magnetic fields in x and y directions with amplitudes up to 15 mT. The xy-piezo stage necessary for the spatial control of the sample is shown along with the SMA connectors that drive the MW signal through the antenna. b) Zoom of the dashed square in the central area from a) depicting the wire loop used to drive the square wave current $I(A)$, responsible for generating the ESA modulation field and the MW antenna containing the nanodiamonds.

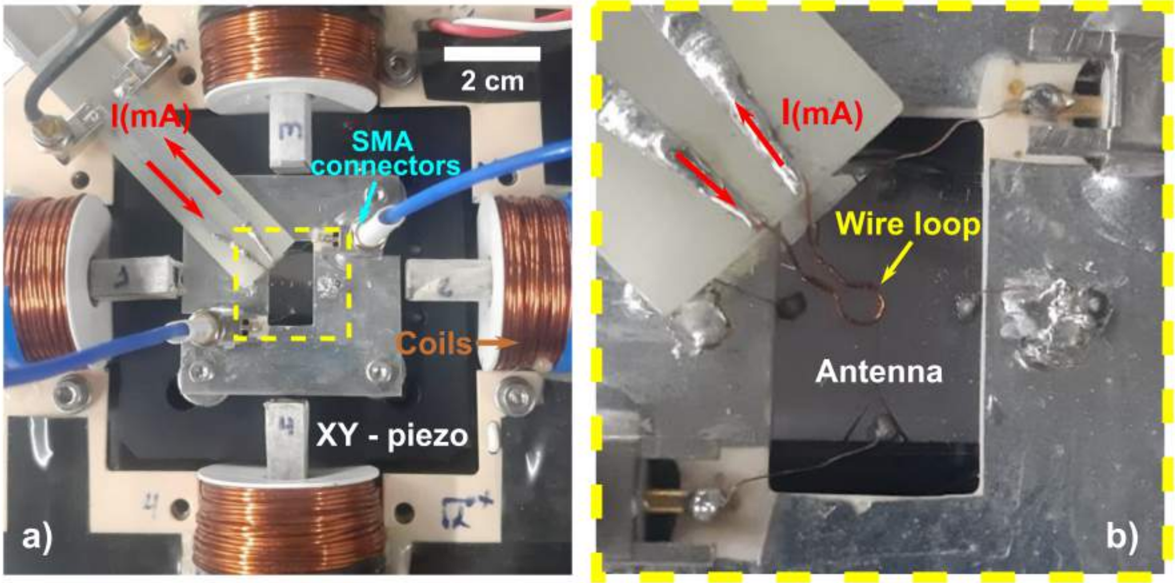

Font: The author (2022)

used for ESR modulation, as will be discussed on section 4.4. A photograph of the sample holder showing the wire loop and antenna can be seen on Figure 30. The main task of the microcontroller is to acquire data, synchronize the APD pulses and MW generator signal, control the modulation field and allocate the data (APD counts) in different variables of the control program for further analysis [83]. The data recording is performed through an arduino-LabVIEW interface which allows one to perform the posterior analysis.

For controlling the temperature of the sample, the same computer-controlled heating device and calibration method presented on the section 3.3 were used. The calibration method was performed on a clean glass coverslip over the objective lens. The emissivity of glass was again used as entry parameter for the FLIR camera ($\epsilon_{glass} = 0.95$) and returned similar results to those presented in the previous chapter, with the temperature of the sample given by $T_S = aT_C + b$; where T_S and T_C are the temperatures of the sample and control, respectively, a and b are the fitting parameters. For the antenna, the calibration returned the fitted values of a = 0.54 ± 0.008 and b = (137 ± 4.0) K as shown on Figure 31. The calibration with the sample containing the deposited antenna over the coverslip was not possible to be carried out since the high reflectivity and low emissivity of the chromium surface ($\epsilon_{chromium} = 0.08$

at 312 K) made it impossible to acquire precise temperature measurements with the FLIR camera. Thus, it is assumed here that the temperature distribution of the sample containing the antenna is equivalent to a glass coverslip with thickness of 130 - 170 μm, orders of magnitude larger than the metallic layers of the antenna ($\simeq$ 100 nm).

Figure 31 – Temperature of the antenna containing the nanodiamonds as a function of the set temperature of the control program. The data points are displayed along with the linear fit used to calibrate the real temperature of the sample.

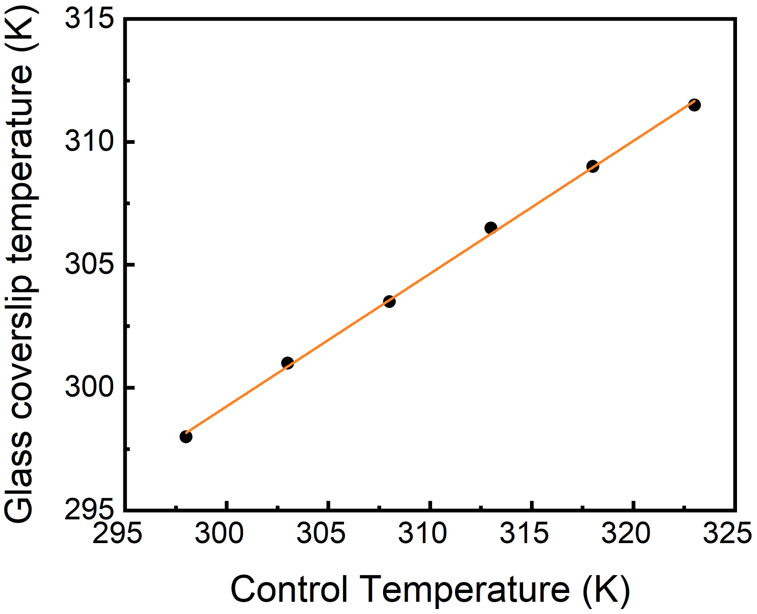

Font: The author (2022)

4.3 DETECTION OF INDIVIDUAL EMITTERS AND THERMAL RESPONSE OF NV$^-$ DEFECTS

Once concluded the thermal calibration of the system, it is necessary to detect and characterize the individual NV$^-$ defects and determine which of them are suitable for being implemented as nanothermometers. The location of the nanodiamonds can be determined through a confocal scanning luminescence image, as shown on Figure 32a), where several emitting nanodiamonds can be identified in a 8 $\times$ 8 μm^2 region of the sample, constructed pixel by pixel and resulting in a 80 $\times$ 80 pixels image. The emission intensity of the detected fluorophores reaches values of 47.8 kcounts/s, under a pump power density of 3.3 $\times$ 10^4 W/cm^2, estimated with use of equation 3.1 for an measured average power of P = 21 μW after the sample. This pump power density was defined in the same manner reported on section 3.4, for a $FWHM_C$ = 287 nm. The $FWHM_C$ value was measured by Sanchez [145] for the same confocal microscope used in this Thesis and was defined as being the optical resolution of the system according to the Sparrow criterion for confocal microscopy (see Equation 2.35).

Among all detected nanodiamonds presented on Figure 32a), only three of them were identified as possessing an individual NV^{-} defect. The single emitters were labeled as NV1, NV2 and NV3, as indicated by the white arrows on Figure 32a). The implementation of a HBT interferometer [146] allows one to confirm the single photon character of these fluorophores through the measurement of $g^{(2)}(\tau)$, as shown on Figures 32a), b) and c) for NV1, NV2 and NV3, respectively. In general words, $g^{(2)}(\tau)$ is a normalized function that measures the number of coincidences between the detection of two single-photons by different APDs as a function of the delay time τ between the single-photon counts. The second order correlation function for n quantum emitters at $\tau = 0$ is given by [146]

$$g^{(2)}(0) = 1 - \frac{1}{n}, \tag{4.1}$$

which means that a single emitter ($n = 1$) must present an antibunching behavior at $\tau = 0$, resulting in values of $g^{(2)}(0) \leq 0.5$. Thus, in this chapter, it is assumed that all the emitters that present $g^{(2)}(0) < 0.5$ are identified as single emitters. As can be seen from the Figures 32b), c) and d), the measured $g^{(2)}(0) < 0.5$ indicates that the three selected nanodiamonds satisfy this criterion, a necessary feature to assign these emitters as single-photon sources [147]. Besides, the selected nanodiamonds presented high photostability even under several hours of optical pumping which is critical for the thermal sensing experiments, shown next.

Designated the single emitters, the detected luminescence of from NV^{-} defect is sent to a single APD in order to perform the ODMR measurements, according to the following steps: first, the TTL electrical signal generated for each photon detection is counted by the Arduino microcontroller with a temporal resolution of 12 ns. Then, a MW generator (Aim $\&$ Thurlby Thandar Instruments TGR6000) feeds the photolithographed antenna. The ODMR spectra are obtained by recording the luminescence intensity as a function of the MW frequency ν_{MW}. As discussed on subsection 2.2, the detected luminescence intensity decreases when ν_{MW} matches the ESR frequency for the NV^{-} spin transitions $m_s = 0 \rightarrow m_s = \pm 1$.

The ODMR measurements for the three selected NV^{-} defects are plotted on Figure 33 where the blue circles and red squares represent, respectively, the acquired data in the absence and in the presence of a 10 mT external magnetic field in x direction, as seen in the laboratory reference frame. The magnetic field is generated by a pair of coils previously calibrated, capable

Figure 32 – a) Typical scanning luminescence image of a 8 × 8 μm^2 region of the sample. The white arrows designate the selected nanodiamonds containing a single NV$^-$ defect with which the nanothermometry experiments were made. The pump power density used here was 3.3 × 10^4 W/cm^2 at the sample. The antibunching dip below the dashed black line indicates $g^{(2)}(0) < 0.5$, which is enough to ensure the single photon character of the emitted light for the b) NV1, c) NV2 and d) NV3.

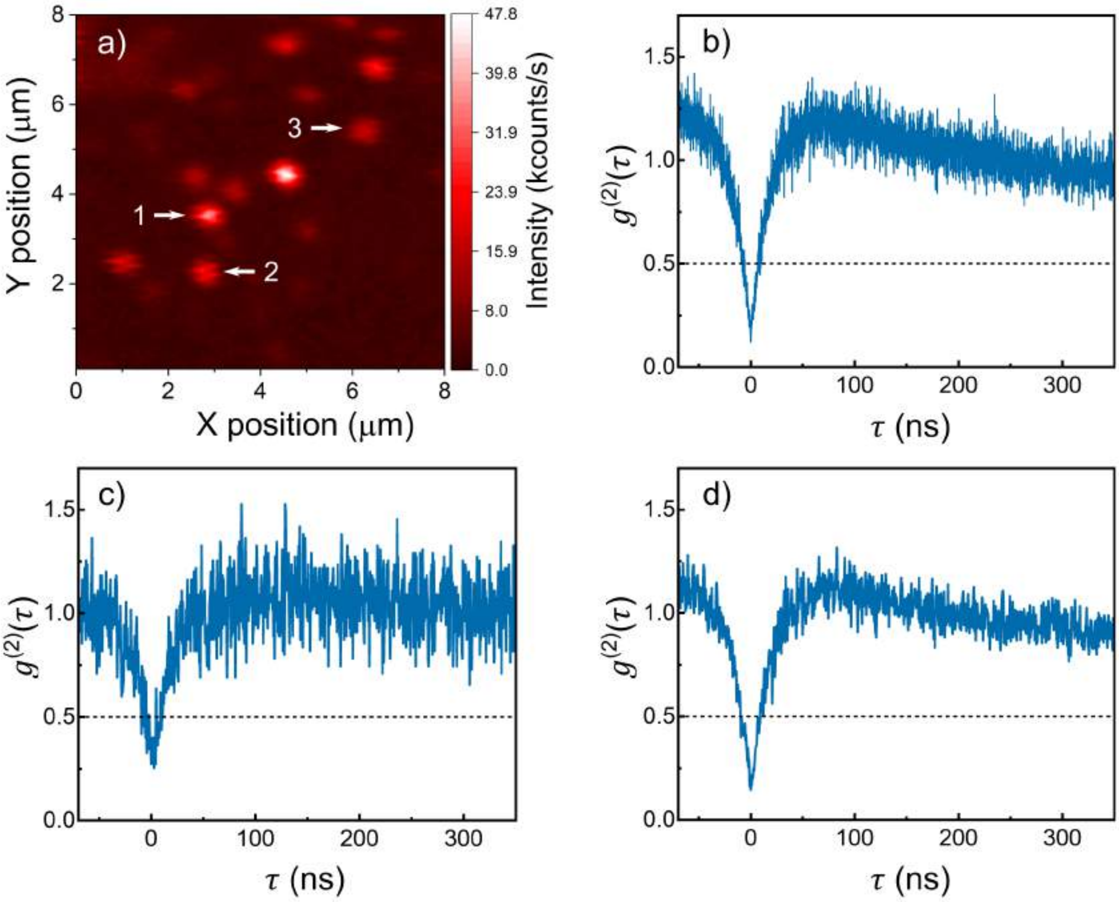

Font: The author (2022)

of generating 18.7 mT/A of applied electric current [see Figure 28a) and reference [83]]. From Figure 33, it can be noticed that the ODMR contrast varies between 25 % [Figure 33a)] for the NV1 and 10 % for the NV3 [Figure 33c)]. Besides, in the absence of any external field, it is possible to measure the piezoelectric coupling constant $2\mathcal{E}$ due to the natural ESR splitting for the three defects resulting in values of 14.4 MHz, 8.7 MHz and 20.0 MHz for NV1, NV2 and NV3, respectively. These values were obtained by fitting the ODMR dips with Lorentzian curves, not exhibited on Figure 33 for the sake of simplicity. As mentioned in subsection 2.2.4, this splitting at zero field is due to the presence of surface strain present in nanodiamond which in turn is associated with the piezoelectric properties of the diamond matrix. When

Figure 33 – Normalized ODMR spectra for the individual NV$^-$ defects a), d) NV1; b), e) NV2; c), f) NV3 in the absence (blue circles) and in the presence (red squares) of an external magnetic field with magnitude of 10 mT in the x direction. The contrasts are in a range from 25% (NV1) to 10 % (NV2). The spectrum in the absence of any external field allows to determine the piezoelectric coupling constant $2\mathcal{E}$ = 14.4 MHz, 8.7 MHz and 20.0 MHz for NV1, NV2 and NV3, respectively.

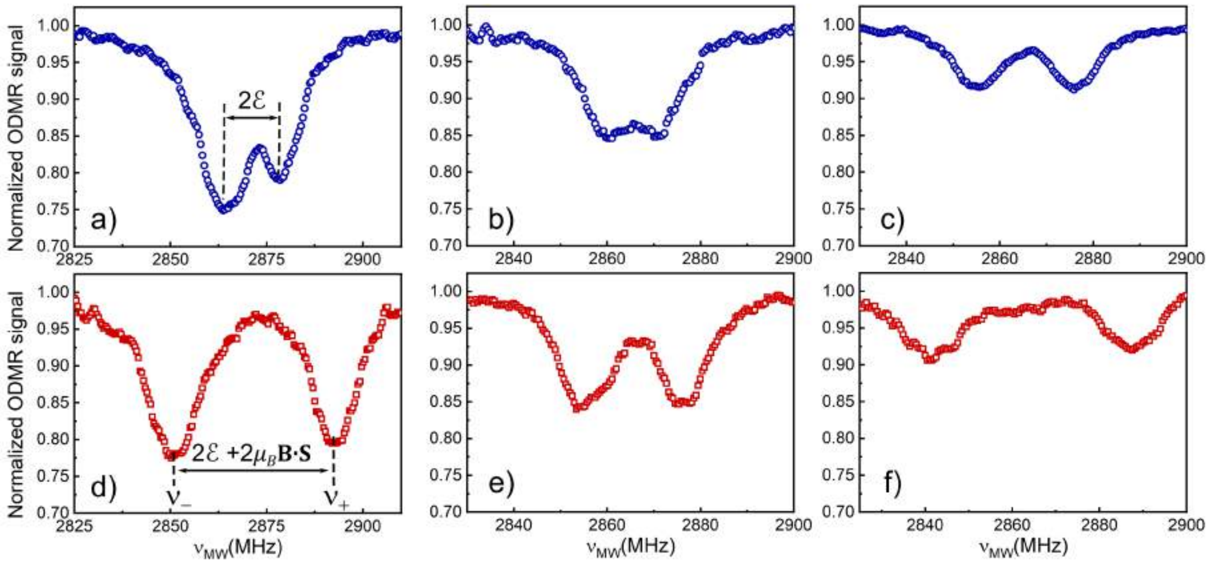

Font: The author (2022)

an external magnetic field interacts with the system, as shown on Figures 33d) to 33f), it is possible to notice the manifestation of the Zeeman effect accounting for further splitting of the ESR frequencies. As will be discussed below, the presence of an external magnetic field is of fundamental importance when monitoring the ESR frequencies of a NV$^-$ defect.

Once performed the ODMR measurements on the selected NV$^-$ centers, the temperature dependence of the ESR frequencies can be measured for each emitter. In order to do that, the frequency of the ν_- resonance is monitored as a function of temperature in the presence of a constant external magnetic field, as discussed on subsection 2.2.4. The ν_- resonance frequencies were recorded for temperature values ranging from 294.7 K to 313.2 K in 2.5 K steps. In order to assure the thermal equilibrium of the sample, the ODMR measurements were performed only after 20 minutes for each new temperature value. The ODMR spectra measured for the NV1 at minimum (blue) and maximum (red) temperatures are plotted on Figure 34a) where the data points, represented by open circles, were adjusted with Lorentzian curves, plotted as solid lines. In this figure, the extreme ν_- frequencies for the NV1 were 2850.3 MHz and 2848.5 MHz at 294.7 K and 313.2 K, respectively, which exemplifies the thermally induced frequency shift of the ESR resonances. The measurements on the temperature dependence for each NV$^-$ defect are presented on Figure 34b) and the main results are summarized on Table 2.

Figure 34 – a) ODMR spectra obtained at 294.7 K (blue) and 313.2 K (red) for the NV1. The circles represents the measured data and the solid lines the Lorentzian fitting curves. The measured ν_- frequencies were 2850.3 MHz and 2848.5 MHz at 294.7 K and 313.2 K, respectively, resulting in $S^{ODMR} = \partial\nu_-/\partial T =$ -(100 ± 10) kHz K^{-1} for the NV1. b) Frequency shift as a function of temperature for the selected nanoparticles. The blue squares, orange dots and green diamonds correspond to the NV1, NV2 and NV3, respectively. The linear fits from the measured data return $\partial\nu_-/\partial T$ for NV2 and NV3 given by $-$(88 ± 8) kHz K^{-1} and $-$(110 ± 14) kHz K^{-1}.

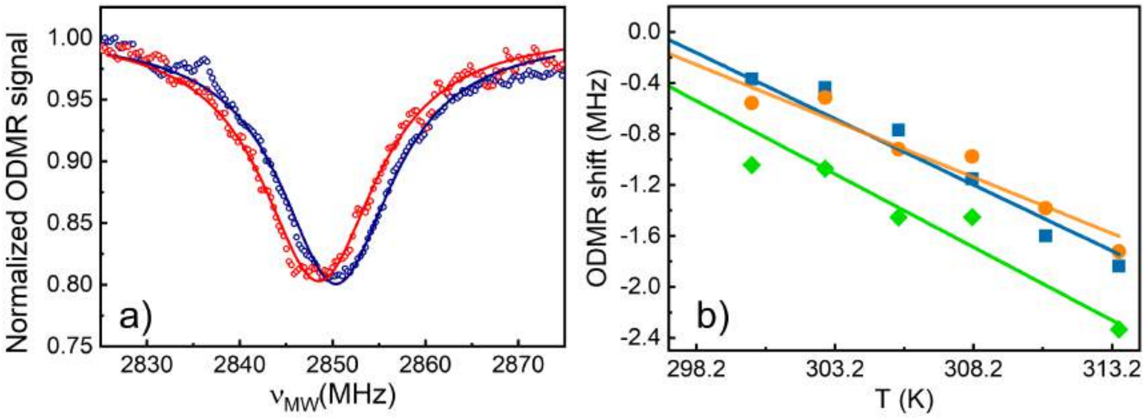

Font: The author (2022)

The ν frequencies for the NV1 (blue squares), NV2 (orange dots) and NV3 (green diamonds) present a linear dependence on temperature, returning S^{ODMR} (Equation 2.23) values of $-$(100 ± 10) kHz K^{-1}, $-$(88 ± 8) kHz K^{-1} and $-$(110 ± 14) kHz K^{-1} for NV1, NV2 and NV3, respectively. The experimental errors were extracted from the uncertainties of the fitted parameters. Although the results of S^{ODMR} obtained for the selected emitters are quite similar, taking into account the experimental uncertainties, there are noticeable differences between them. As argued by Doherty *et al.* [109] this difference may be due to different structural defects, impurities, surface morphology and inner strain of each nanodiamond which can lead to distinct contributions of the thermal expansion to the frequency shift of ν_- with T (see Equation 2.16). This argument is reinforced by the obtained results for 2$\mathcal{E}$ (see Table 2), related to the nanodiamond inner strain. It can be noticed a direct correspondence between the measured $2\mathcal{E}$ values and S^{ODMR} indicating that the different inner strains may contribute to the dependence of ν_- with temperature. The obtained S^{ODMR} values are in accordance to those reported in other studies performed on nanodiamonds [117, 120, 85, 113] with corresponding values ranging from -50 KHz K^{-1} to -100 KHz K^{-1}.

On table 2 are also presented the obtained values for S_R^{ODMR} with use of Equation 2.26. For the NV1, NV2 and NV3 values of (3.6 ± 0.3) × 10^{-3} $\%$ K^{-1}, (3.1 ± 0.3) × 10^{-3} $\%$ K^{-1} and (4.0 ± 0.4) × 10^{-3} $\%$ K^{-1}, respectively. The experimental uncertainties were calculated

Table 2 – Measured parameters for the three selected NV$^-$ defects extracted from linear fittings to experimental data by using Equations 2.29, 2.30 and 2.23.

NV$^-$	$\mathcal{D}_{gs}$ (MHz)	$2\mathcal{E}$ (MHz)	S (kHz K^{-1})	S_R (10^{-3} % K^{-1})	δT (K)
1	2871.6 ± 0.4	14.4 ± 0.4	-100 ± 10	3.6 ± 0.3	0.7
2	2865.5 ± 0.1	8.7 ± 0.1	-88 ± 8	3.1 ± 0.3	1.0
3	2865.7 ± 0.1	20.0 ± 0.1	-110 ± 14	4.0 ± 0.4	2.8

Font: The author (2022)

through standard error propagation. The measured values for the relative sensitivity of the selected single defects are higher than those obtained for ensemble measurements. For instance, Acosta *et al.* reported relative sensitivities of $\simeq$ 2.6 × 10^{-3} % K^{-1} for an ensemble of nanodiamonds embedded in a bulk sample and recently, Fujiwara and collaborators [113] reported relative sensitivities of $\simeq$ 2.3 × 10^{-3} % K^{-1} for nanodiamonds containing around 200 NV$^-$ defects. The S_R^{ODMR} results for the three selected particles are at least 25 % higher than those reported for ensembles. The differences on S_R^{ODMR} between the nanodiamonds follow the behavior presented by the measured S^{ODMR} values, whose reasons were discussed above.

The thermal resolution was also measured for each single emitter through the use of Equation 2.30. In order to do this, it is necessary to take into account the parameters Δf and C obtained from the ODMR measurements at $T =$ 294.7 K (see Figure 33); the photon count rate I_0 and the integration time t used for the ODMR data acquisition. Thus, by indicating the respective defect by the subscript in parenthesis, the measured parameters were $\Delta f_{(1)} =$ 7.5 MHz, $\Delta f_{(2)} =$ 6.5 MHz and $\Delta f_{(3)} =$ 11.5 MHz; $C_{(1)} =$ 0.2, $C_{(2)} =$ 0.15 and $C_{(3)} =$ 0.1 and $I_{0(1)} =$ 60 kcounts/s, $I_{0(2)} =$ 40 kcounts/s and $I_{0(3)} =$ 35 kcounts/s, obtained under $\mathcal{P} =$ 6 × 10^4 W/cm^2 with integration time of 1 s. The measured thermal sensitivities were 0.7 K, 1.0 K and 2.8 K for NV1, NV2 and NV3, respectively. As δT depends not only on the thermal sensitivity but also on the ODMR contrast C and on the photon count rate I_0, the best thermal resolution was obtained for the NV1. It is clearly noticed when considering δT for the NV3 that, despite presenting a higher S^{ODMR} value, the low measured C and I_0 along with a high Δf value result in a worse thermal sensitivity if compared to the other two NV$^-$ centers. As mentioned on subsection 2.3.1, the thermal resolutions reported on literature for this kind of luminescent nanothermometers used for direct temperature measurements usually ranges from $\sim$ 0.2 K [113] to $\sim$ 2.3 K [117] and in exceptional cases can present δT on the order of mK [85, 120]. However, to the best of our knowledge, all the mentioned references carry out the thermometry measurements by implementing bulk samples or nanodiamonds doped with hundreds of NV$^-$ defects as sensing devices. The use of several emitters by definition (Equation 2.30) improves the thermal resolution of the system by a factor of $1/\sqrt{N}$, where N is the number of emitters [76]. Thus, by considering as a reference the thermal resolution of the NV1, for a nanothermometer with about 200 emitters, the measured δT value would be on the order of 50 mK. Therefore, the main feature of this study is indeed the use of a single defect whose thermal characterization resulted in thermal resolutions comparable and even better than other systems using ensembles of NV$^-$ defects on nanodiamond.

The results discussed above show that the nanothermometers present distinct thermal responses, measured through S^{ODMR} and S_R^{ODMR} and are caused by inner strains and/or structural defects on each nanodiamond. Besides, the discrepant results obtained for δT indicates that a balance between S^{ODMR} and other parameters, such as C, Δf and I_0 must be taken in account to perform precise temperature measurements with individual NV$^-$ defects just as in the case with the codoped Yb^{3+}/Er^{3+}NCs reported in the previous chapter. Therefore, in order to perform the temperature monitoring measurements with an individual defect, it is advantageous to assign the nanodiamond that presented the best thermal resolution as the selected nanothermometer which, in this case, is given by the NV1. The obtained results on real-time nanothermometry carried out by using the NV1 as a nanoprobe are reported on the next section. The experimental method used for tracking the ESR frequencies will be shown along with the evaluation of the system thermal sensing capabilities.

4.4 TEMPERATURE MONITORING WITH A SINGLE NV$^-$ DEFECT

Measurements of the sample's temperature are performed with previous characterization of a NV$^-$ defect S^{ODMR} , as described in the previous section. Thereby, by defining the NV1 as the selected nanothermometer, one gets the system ready for performing the temperature measurements. As shown on section 4.2, an Arduino Duo-based device is used to control the polarity of a H-Bridge implemented here to generate a square wave current that feeds a wire loop antenna. It results in the generation of an AC magnetic field whose interaction with the NV$^-$ defect causes a modulation on the ESR frequency which can be used to generate an error signal from the detected NV$^-$ luminescence. It is done as follows: once the the MW frequency is resonant to a ESR frequency, the symmetric modulation of the AC magnetic field by $\pm\delta B_{mod}$ makes the luminescence counts to present the same value regardless of modulation magnetic field orientation, as depicted on Figure 35. Hence, a differential measurement of the detected luminescence results in zero counts when the MW frequency is resonant with the electronic spin transition. A shift from the ESR frequency caused by temperature changes implies in an imbalance in the luminescence differential counts. This generates a non-zero error signal that can be used to correct the MW frequency until the ESR frequency be achieved, once the balance in counts is reached [83].

Figure 35 – Representation of the ESR frequency tracking strategy used for nanothermometry measurements. The ODMR signal (solid red line) returns the resonance frequency ν which is shifted by $\delta\nu$ due to an increase in the temperature of the system. A square wave current induces an alternating magnetic field that modulates the ESR frequency (red dashed lines). The error signal ΔS is then obtained trough the difference between the photon counts during positive $C(\text{i}_+)$ and negative $C(\text{i}_-)$ values for the current responsible for generating the modulated magnetic field. A frequency shift induced by temperature variation results in a measured $\Delta S \neq 0$. Once $\nu_0 = \nu_{MW}$, $\Delta S = 0$. Then, by processing the error signal, it is possible to track the ESR frequency and determine the frequency shift induced by temperature variations of the system.

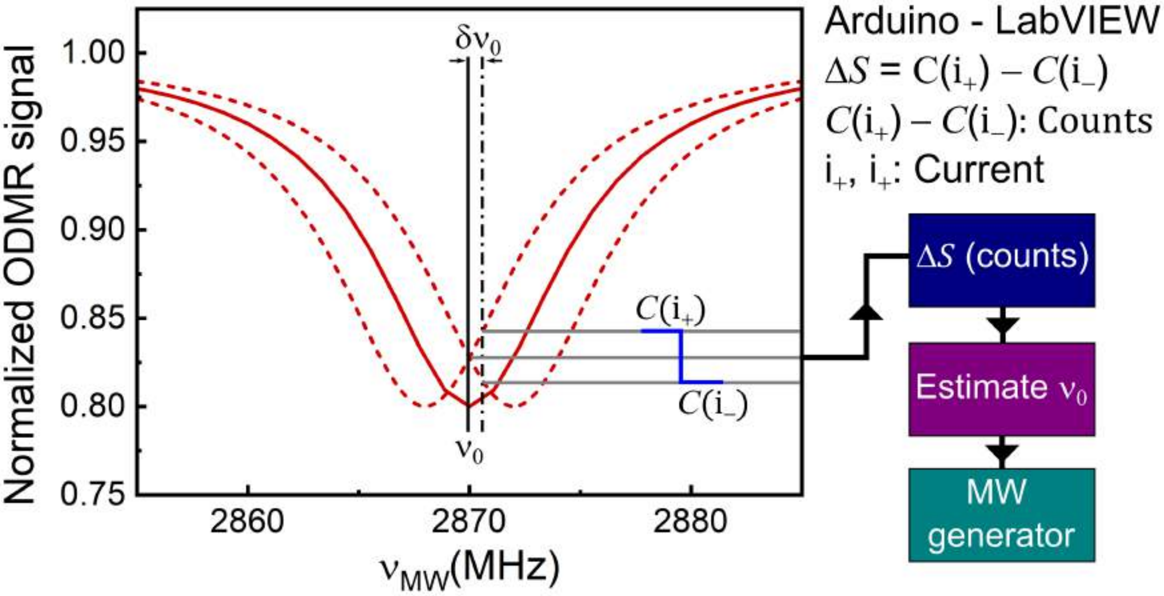

Font: Adapted from [83]

In practice, the lock-in procedure used here assumes that the splitting between the $m_s = \pm 1$ spin sublevels is large enough in such a way that only the ODMR spectrum of a single Zeeman sublevel is considered. By considering the ESR resonance frequency as ν_0 (either ν_+ or ν_-), the quantity $S(\nu_{MW} - \nu_0)$ can be defined as the luminescence signal when the chosen ESR frequency is monitored in real-time. Due to the Zeeman effect, the external magnetic field modulates the ESR frequency by $\pm\Delta\nu_0$ through a square wave, allowing one to measure $S(\nu_{MW}-\nu_0+\Delta\nu_0)$ and $S(\nu_{MW}-\nu_0-\Delta\nu_0)$ through the detection of luminescence synchronized with the current modulation, obtaining a first-order difference on the signals defined as

$$\Delta S(\nu_{MW} - \nu_0) = 2\frac{dS(\nu_{MW} - \nu_0)}{d\nu_{MW}}\frac{d\nu_0}{dB_{mod}}\delta B_{mod}, \tag{4.2}$$

where $\Delta\nu_0 = d\nu_0/dB_{mod}$ is the resonance frequency shift induced by the modulation field. It can be noticed that $\frac{d\nu_0}{dB_{mod}} = \pm g\mu_B/h$ when the Zeeman splitting of the $m_s = \pm$ 1 sublevels is much larger than the natural split $2\mathcal{E}$. This condition is satisfied with the application of an bias field that, as mentioned before, is generated by a pair of coils and is strictly necessary for the temperature measurements. Furthermore, $\frac{dS(\nu_{MW}-\nu_0)}{d\nu_{MW}}$ can be determined from the ODMR curve and the modulation amplitude δB_{mod} can be calibrated by measuring the peak to peak variation as a function of ν_{MW}. Thus, all terms on Equation 4.2 can be determined [83].

Experimentally, the ΔS value is measured by the microcontroller by counting the number of detected photons synchronously to the applied square wave modulated current. Then, if $\nu_{MW} = \nu_0$, then $\frac{dS(\nu_{MW}-\nu_0)}{d\nu_{MW}} = 0$ which represents a minimum on the ODMR curve resulting in $\Delta S = 0$. A variation on the temperature of the system causes a slight shift of ν_{MW} relative to the value of ν_0 leading to $\Delta S \neq 0$. Therefore, for a calibrated nanothermometer, *i.e.*, by knowing $\partial\nu_0/\partial T$, a small ESR frequency shift $\delta\nu_-$ caused by a change in temperature can be compensated by a shift on the MW frequency by $\delta\nu_{MW} = -\delta\nu_0$ in order to obtain $\Delta S \approx$ 0. It allows the tracking of ν_0 and consequently, enables the measurement of the local temperature through the knowledge of $\partial\nu_0/\partial T$.

In the limit case of small $\Delta\nu$, Equation 4.2 can be written as [83]

$$\Delta S(\nu_{MW} - \nu_0) = \frac{dS(\nu_{MW} - \nu_0)}{d\nu_{MW}}\bigg|_{\nu_{MW}=\nu_0} 2\Delta\nu_0, \tag{4.3}$$

and the slope of $\Delta S(\nu_{MW} - \nu_0)$ close to $\nu_{MW} \approx \nu_0$ as a function of ν_{MW} can be used to calibrate the system response to the modulation magnetic field. Thus, before performing the ESR tracking, the Arduino-based microcontroller is used to acquire the slope of the error signal for frequencies close to ν_0. As mentioned before, the nanodiamond containing the NV1 defect was selected as a nanothermometer. Therefore, it is necessary to measure ΔS for this emitter to calibrate the tracking system. In order to do that, the microcontroller records number of photon counts during 100 ms synchronized with the square wave modulation of B_{mod} at a frequency of 10 kHz. Figure 36a) shows the pulse sequence implemented to modulate the ESR frequency ν_- which spin manipulation protocol is described in the following. First, by keeping the excitation light at 532 nm ON, the NV$^-$ defect is initialized in the $m_s = 0$ spin sublevel via optical pumping. Then, the modulation field B_{mod} is activated at 50 $\%$ duty cycle

Figure 36 – a) Pulse sequence implemented to modulate the ESR frequency of the NV1 through a modulation field B_{mod}. b) Measured $\Delta S(\nu_{MW} - \nu_{-})$ (blue circles) for B_{mod} switching at 10 kHz for frequencies in the vicinity of the ESR. The dashed green line indicates a slope of 24.6 counts/MHz and is used for the calibration of the ESR tracking system. The data is adjusted with the derivative of a Lorentzian lineshape (solid red line).

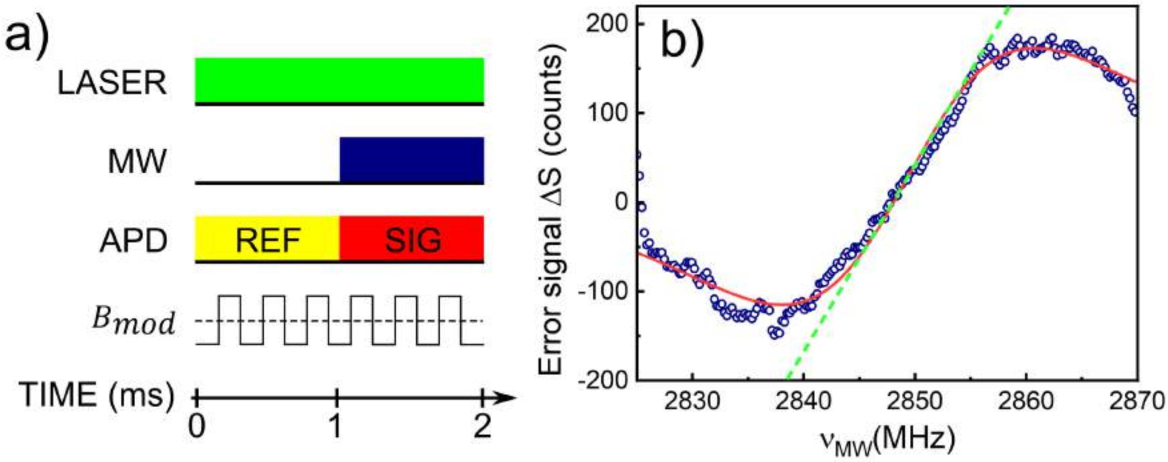

Font: a) adapted from [83] and b) the author (2022)

in order to symmetrically modulate the spin transition line. Meanwhile, the APD is counting the NV$^-$ luminescence photons all the time while a routine programmed in Arduino software sets an intensity reference [REF signal on Figure 36a)] by recording the photon counts during the first ms when the MW is OFF and a signal by recording the counts during the last ms when the MW is set ON [REF signal on Figure 36b)] [83]. This sequence is repeated for every MW value in steps of 225 kHz. The obtained data for ΔS are proportional to the ODMR signal for NV1 shown on Figure 34a) (at 294.7 K) and is shown on Figure 36b). It can be noticed that the error signal is centered on the ν_{-} resonance, as it should be. The dashed green line on Figure 36 indicates the linear fitting used for obtaining the slope of ΔS close to the ESR frequency, resulting in 24.6 counts/MHz. This value is then used to calibrate the system response to B_{mod}. To carry out the experiments, the generated MW signal with a power output of -20 dBm or 10 μW is amplified by 45 dB (Mini-circuits ZHL-16W-43-S+). The MW signal amplification results in a MW power of $P_{MW} \simeq 320$ μW passing through the antenna. An alternating current of 400 mA was used to modulate the magnetic field. As shown on reference [83], the data obtained by tracking the ESR frequency presents a typical noise floor of ± 2 MHz whose minimum fluctuation is obtained for sampling times above 100 ms. From equation 2.30 it can be noticed the inversely proportional relation between δT and the integration time t. Thus, as the temperature changes in this experimental setup are slower than $\sim$ 1 min due to the indirect heating of the sample, a sampling time of 1 s was defined as a suitable value for performing the nanothermometry measurements.

The first temperature measurement was performed to investigate the responsiveness of the tracking system under temperature changes. For doing this, the ESR frequency of the NV1 was monitored while the temperature of the system is continuously increased from the room temperature ($\sim$ 295 K) to the system maximum temperature ($\sim$ 313 K). The result of the ESR tracking performed over 80 minutes can be seen on Figure 37. The acquired data are represented by the gray line. It is possible to notice that even with an integration time of 1 s, there is a typical noise floor of around 2 MHz. As the temperature induced frequency shifts are on the same magnitude of the detected noise, it is necessary to post-process the acquired data to determine the average temperature of the sample. Hence, to obtain a more precise temperature measurement with the nanothermometer, a 150 point adjacent-average filter was used on the obtained data. This filtering method was already used in other experiments, as reported in reference [113]. The post-processed result is represented as the red solid line on Figure 37. From the figure, it can be noticed that the ESR frequency of the ν_- resonance at the starting point was 2854.5 MHz and decreased to 2852.8 MHz at final temperature. This shift in frequency corresponds to a measured temperature shift of $\Delta T \simeq$ 17 K that, considering the fluctuation of the filtered signal of about $\pm$ 250 kHz, the experimental error is of $\sim$ 2.5 K. The obtained result for ΔT agrees with the temperature interval determined on the control program ($\simeq$ 18 K). A linear fit of the averaged data returned a slope of 300 kHz/min which results in a temperature increasing rate of $\sim$ 0.3 K/min. This temporal response of the nanothermometer is way below the maximum capacity of the tracking system, which is capable of detecting frequency changes at rates of 0.8 MHz/s [83] corresponding to temperature change rates of 8 K/s. Hence, the temporal resolution of the temperature tracking is mainly determined by the slow rate of sample heating. Due to the spatial displacement of the sample and fluctuations of the objective oil under heating, the main difficulty of this experiment was to keep the high photon count rate during all the acquisition time. Despite the ESR frequency measured by the tracking program depends on the relative counts recorded synchronously with the modulation field, the low count level may be a reason for the presence of some acute fluctuations shown on the data points. However, it is important to point out that the responsiveness of the system is quite satisfactory and the $\pm$ 2.5 K error on the temperature data may be due to some experimental limitations, such as the manual control of the nanodiamond position which may lead to low photon-count rates at some moments. The continuous temperature monitoring on

Figure 37 – ESR frequency tracking of ν_{-} for the NV1 under continuous temperature increase up to 313.4 K as a function of time. The data is represented by the gray line. An adjacent-average filter using 150 points was used to process the data. The right-hand y axis is plotted considering the $S^{ODMR} = -100$ kHz/K for the NV1 defect. The average resonance frequency diminishes from 2854.5 MHz to 2852.8 MHz corresponding to temperature increase of (17 ± 2.5) K.

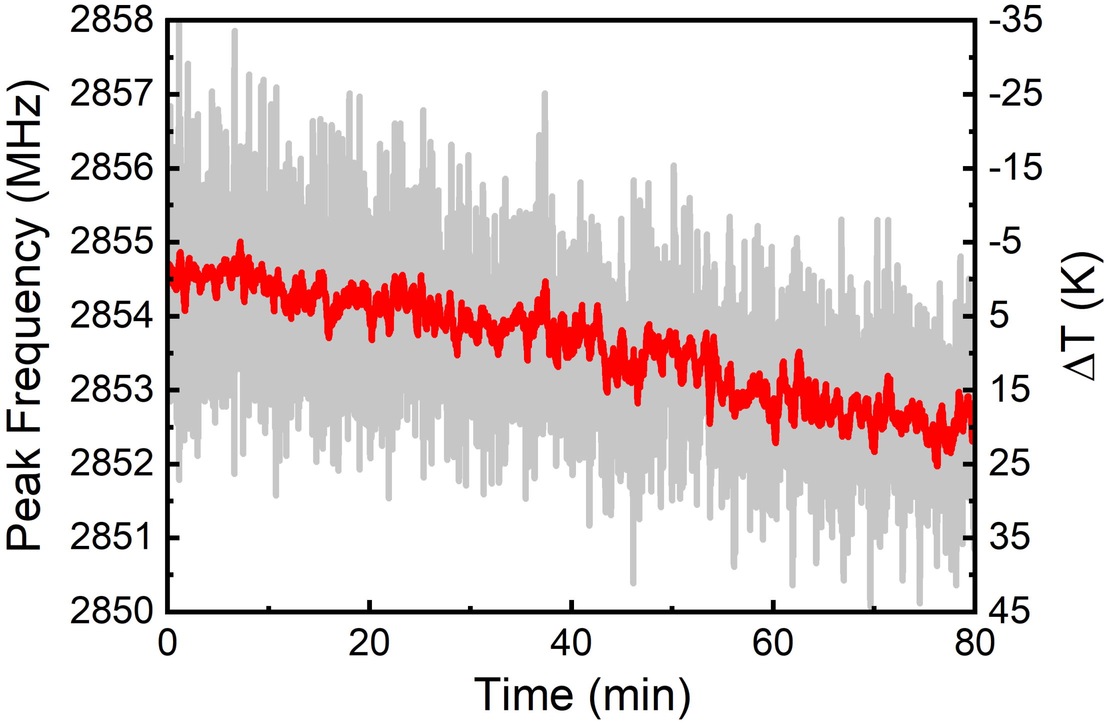

Font: The author (2022)

the cooling cycle was impossible to obtain since the fast cooling of the sample imply in fast deviations from the optimized position of the nanoparticle, leading to a complete loss of the detected luminescence.

The temperature monitoring with a single nanodiamond, as presented on Figure 37, can be applied for investigating temperature distributions of sub-micrometric systems with spatial resolutions limited only by the dimension of the nanothermometer which, in this case, is of about 25 nm. The spatial resolution achieved with the nanodiamonds reported in this chapter are at least 50% better than those reported on other studies on nanothermometry with NV^{-} defects on nanodiamonds [120, 113, 148], reinforcing the implementation of the single defect-based nanothermometers presented in this chapter for ultra-high resolution purposes. Furthermore, as shown by Plakhotnik and collaborators [110], the thermal dependent behavior of NV^{-} defects on nanodiamonds is observed even for temperatures as high as 700 K. Similar results were reported by Toyli *et al.* [149] for temperatures above 600 K. These studies indicates that the nanothermometry technique presented here can be used not only on the biological

Figure 38 – Time profile of ΔT over the stepwise temperature variation of the control program in steps of 5 K. The gray line represents the data while the red line is the filtered data. It was used a 100 point adjacent-average to process the results. The blue line is the average temperature of the plateaus obtained through an average on the processed data.

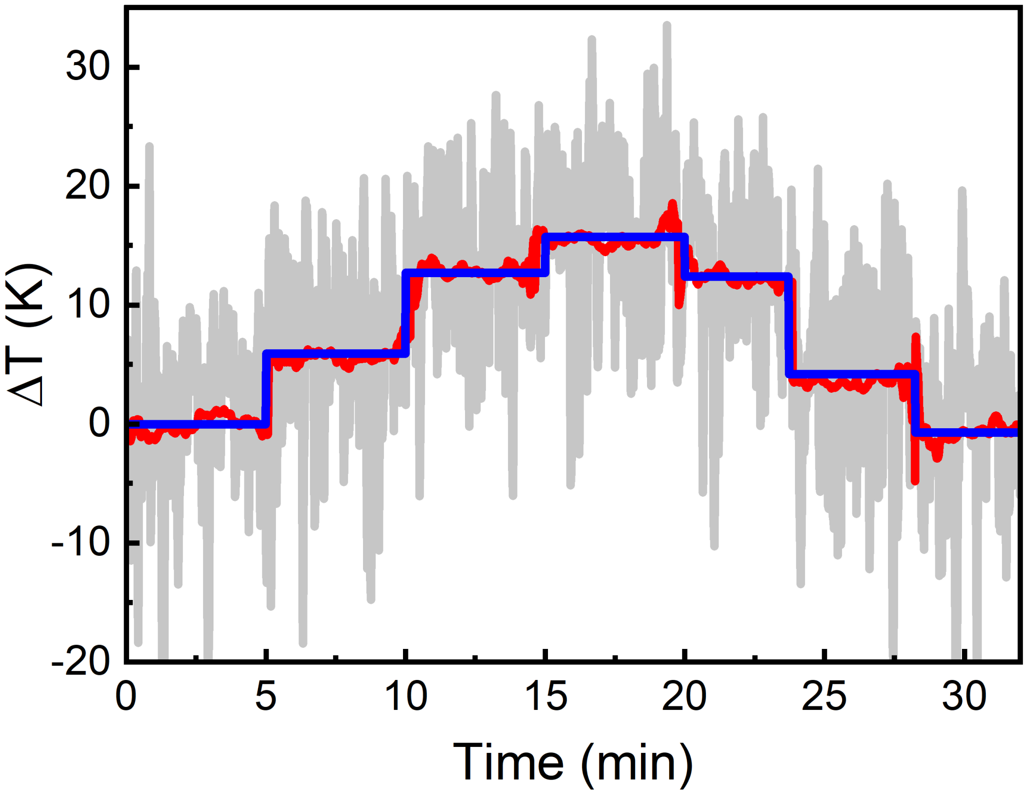

Font: The author (2022)

temperature range, but also for high temperatures indicating its possible industrial/chemical applications. As an example, Laraoui *et al.* reported results on the imaging of thermal conductivity using a single spin probe as a thermometer, which is clearly possible to be performed with the detection system described in this chapter which may also be implemented on several areas, from the investigation of phonon dynamics in nanostructures to the characterization of heterogeneous phase transitions and chemical reactions in various solid-state systems [90]

After the control experiment described above investigated the thermal responsiveness of the selected nanothermometer under continuous temperature changes, a more precise measurement was carried out. Now the temperature of the system is set at $\sim$ 298 K and measured by the tracking system during $\sim$4 to 5 minutes. Elapsed that time, the temperature of the system is increased in 5 K and after 20 minutes of waiting - for assuring the thermal equilibrium of the sample - the temperature is monitored again during a few minutes. This process is repeated until the temperature of the sample reaches $\sim$ 313 K, leading to a difference between the initial and final temperature of $\Delta T = 15$ K. Then, the inverted process begins until the sample reaches the initial temperature. The result of this experiment is shown on Figure 38. The obtained data are represented by the gray line and the average-filtered result is plotted as a red line. The average was performed over 100 adjacent points for each fixed temperature value. The blue solid line is the measured average of the filtered data, used here to obtain the standard deviation for the temperature readings, resulting in a uncertainty value of $\pm$ 1.7 K. The temperature profile presents a step-like behavior as it should be. The temperature plateaus agree with the control temperature considering the measured experimental error. The uncertainties for the temperature averages are higher than the obtained thermal resolution for the NV1, as presented on Table 2. It is mainly due to the high noise level of the tracking measurements that may jeopardize the data averaging and possible temperature miscalibration of the system.

The MW antenna also may increase the local temperature of the sample by about 2 K after several minutes, which may explain the differences between the measured temperature by the nanothermometer and the calibrated temperature control. The spatial drift of the nanodiamond can be corrected by implementing a real-time spatial tracking of the single emitters, as reported on reference [113]. It should avoid a series of problems encountered while developing this study, such as the sudden loss of the nanodiamond due to fast sample deviations at high temperatures. Nevertheless, it is worth remembering that temperature changes of this system occur in time intervals of the order of minutes and the ESR tracking system is capable of monitoring frequencies corresponding to changes on external fields oscillating at 0.1 Hz [145]. Thus, due to the limited temperature range allowed by this experimental setup, it is reasonable to assume that a more sophisticated heating system may allow the execution of experiments under high temperature intervals and acquisition rates at least 10 times faster than the used in the herein reported experiments.

So far in this chapter, the characterization of three individual NV^- defects as individual nanothermometers was reported. The nanosensors presented relative sensitivities up to 4.0×10^{-3} % and best thermal resolutions of 0.7 K. It was also noticed that the individual nanothermometers show distinct thermal responses which reinforces the assumption of the individual characterization of nanothermometers discussed in the previous chapter. The presentation of these results was followed by the description of how these nanosensors can be used for monitoring the temperature of a system. A proof-of-concept was carried out in an experiment where a previously characterized nanodiamond was used to monitor the temperature of the system which was able to detect temperature changes with precision of 1.7 K. This finishes the discussions about the obtained results presented on this Thesis and the next chapter will bring the conclusions and perspectives from the presented results.

5 CONCLUSIONS AND PERSPECTIVES

In this Thesis, after introducing the concepts of luminescence nanothermometry with individual NCs, the physical bases for performing LIR- and ODMR-based thermometry were discussed in detail. In the sequence, the concepts of relative sensitivity and thermal resolution were presented along with the methods used to determine these parameters for single nanothermometers, followed by the fundamentals about the experimental optical microscopy techniques that allows the detection of single emitting NCs with sub-micrometric precision.

Then, by implementing a combination of scanning optical microscopy and spectroscopy techniques, the first experimental study in this Thesis consisted on measuring the thermal responses of five nanothermometers composed by individual Y_2O_3:Yb^{3+}/Er^{3+}NCs in three different media, in a temperature range from 293 K to 323 K. The experiments investigated the influence of the surrounding medium (air, water and ethylene glycol) on the NCs relative sensitivity of each nanothermometer. This thermal parameter was obtained through LIR measurements under CW laser excitation at 977 nm by analyzing the UC emission of the $^2H_{11/2}$ and $^4S_{3/2}$ excited states of Er^{3+}.

The LIR results show that the relative sensitivities obtained for the five individual NCs presented distinct values between each other in the three investigated media, presenting discrepancies up to 29 $\%$. The maximum measured relative sensitivities at 310 K in air, water and ethylene glycol are given by (2.5 ± 0.2) $\%$ K^{-1}, (2.3 ± 0.4) $\%$ K^{-1} and (1.6 ± 0.1) $\%$ K^{-1}, respectively.

The best thermal resolutions presented by the NCs were 0.4 K, 1.1 K and 0.6 K in air, water and ethylene glycol, respectively. It was also shown that the thermal resolution depends on the measured errors for ΔE and β, found to be systematically higher on water if compared to the other two environments. The thermal sensitivity of the NCs in ethylene glycol is smaller than the measured values in water and air. It could be explained through the NC-solvent interaction which leads to the nonradiative decay from the $^2H_{11/2}$ to the vibrational C - O stretching modes of ethylene glycol molecules. This observation indicates that the use of such luminescent nanothermometers can be strongly affected by its interaction with the surrounding medium. Besides, The presence of a liquid environment around the nanothermometers assures the thermal equilibrium as well as mimics the conditions encountered in biological systems.

It was also interesting to notice that the lower relative sensitivities were presented by the brightest particles and the inverse is also true. Thus, by considering the emitted intensity as proportional to the volume of the particle, it was assumed that the smaller particles have an enhanced sensitivity. Such dependence was also found for the thermometric parameters ΔE , β and S_R^{LIR} , where all depend on the mean NC emitted intensity I as $I^{-0.3}$. This proportionality suggests that the exponent of I may be directly related to the surface/volume ratio. Thus, in summary, the individual thermal sensitivities should be related to surface-related non-radiative quenching effects such as energy transfer to nearby molecules or the presence of surface defects.

The second study was concentrated on performing real-time ODMR-based nanothermometry measurements with single NV$^-$ defects. The detection and identification of individual emitters were carried out by using a home-assembled confocal scanning luminescence microscope associated with a HBT interferometer. Through interferometry measurements, three nanodiamonds were confirmed as being single NV$^-$ defects by measuring $g^{(2)}(\tau)$ <0.5 for each center. These nanodiamonds were selected as the subjects of the nanothermometry experiments.

The deposition of the nanodiamonds on a coverslip containing a photolithographed MW antenna in the surroundings of the single emitters enabled the execution of ODMR. The obtained ODMR spectra for the selected NV$^-$ centers resulted in typical behaviors, with the defects presenting two ESR frequencies around the central frequency of 2.87 GHz. The two resonance frequencies at zero external field were separated by 2$\mathcal{E}$ given by 14.4 MHz, 8.7 MHz and 20.0 MHz for NV1, NV2 and NV3, respectively.

In the presence of an external magnetic field with magnitude of 10 mT, the ν_- ESR frequencies for each selected NV$^-$ defect were measured for temperatures ranging from 298.7 to 313.3 K in steps of 2.5 K, resulting in thermal sensitivities of $-$(100 $\pm$ 10) kHz K^{-1}, $-$(88 $\pm$ 8) kHz K^{-1} and $-$(110 $\pm$ 14) kHz K^{-1} for NV1, NV2 and NV3, respectively. The obtained relative sensitivities for NV1, NV2 and NV3, respectively, were (3.6 $\pm$ 0.3) $\times$ 10^{-3} $\%$ K^{-1}, (3.1 $\pm$ 0.3) $\times$ 10^{-3} $\%$ K^{-1} and (4.0 $\pm$ 0.4) $\times$ 10^{-3} $\%$ K^{-1}. The differences in the thermal sensitivity between the chosen nanodiamonds can be related to structural defects, morphology and distinct inner strains. This conclusion was reinforced by the measurements of 2$\mathcal{E}$, which is related to the intrinsic inner strain of the particles and show a correspondence with the thermal sensitivities presented by each emitter. The measured thermal resolutions for each nanothermometer were 0.7 K, 1.0 K and 2.8 K for NV1, NV2 and NV3, respectively, being related to characteristics of the ODMR spectrum and emission of each nanodiamond.

The temperature monitoring of the sample was carried out by using the nanothermometer that presented the best thermal resolution. This experiment was carried out by using a ESR frequency tracking system based on the modulation of the spin resonances by a 10 kHz switched external magnetic field. The continuous monitoring of the sample's temperature raise from 295 K to 313 K was performed with a temperature resolution of 2.3 K. A second measurement of a step-like temperature profile was also performed, resulting in a temperature accuracy of 1.7 K. The higher uncertainty obtained with the temperature tracking system may be due to the high noise floor on the obtained data, to experimental limitations and possible heating of the MW antenna. To the best of our knowledge, it was the first time that nanothermometry measurements were performed with a single NV^- defect on nanodiamond and the obtained results on relative sensitivity and thermal resolution are comparable and even better than those obtained with ensemble measurements. Besides, based on previous works with the ESR tracking system, the results presented here confirms the possibility of performing nanomagnetometry and nanothermometry with individual NV^- defects, depicting the multi-sensing possibilities of these emitters and the outstanding capabilities of the ESR monitoring system.

The next step on nanothermometry with individual NV^- defects is to perform temperature gradient measurements of the heat inhomogeneities generated by sub-micrometric structures, as metallic tips and microcircuits. Such experiments could imply in direct applications in failure diagnosis and thermal distribution on micro/nano-electronics.

All the results discussed in this thesis reinforces the implementation of Ln^{3+} -based systems and NV^- defects on nanodiamonds as luminescent nanothermometers. However, the results also point out to the importance of the individual thermal responses of each nanothermometer, feature often overlooked in ensemble measurements regardless of the technique used to perform nanothermometry.

REFERENCES

[1] E. L. Wright, *Brief History of the Universe*. UCLA, Jul 2004.

[2] C. Deppner, W. Herr, M. Cornelius, P. Stromberger, T. Sternke, C. Grzeschik, A. Grote, J. Rudolph, S. Herrmann, M. Krutzik, A. Wenzlawski, R. Corgier, E. Charron, D. Guéry-Odelin, N. Gaaloul, C. Lämmerzahl, A. Peters, P. Windpassinger, and E. M. Rasel, “Collective-mode enhanced matter-wave optics,” *Phys. Rev. Lett.*, vol. 127, p. 100401, Aug 2021.

[3] F. S. Taylor, “The origin of the thermometer,” *Ann. Sci.*, vol. 5, no. 2, pp. 129–156, 1942.

[4] D. Jaque and F. Vetrone, “Luminescence nanothermometry,” *Nanoscale*, vol. 4, no. 15, pp. 4301–4326, 2012.

[5] J. Zhou, B. Del Rosal, D. Jaque, S. Uchiyama, and D. Jin, “Advances and challenges for fluorescence nanothermometry,” *Nat. Methods*, vol. 17, no. 10, pp. 967–980, 2020.

[6] S. Sotoma, C. Zhong, J. C. Y. Kah, H. Yamashita, T. Plakhotnik, Y. Harada, and M. Suzuki, “In situ measurements of intracellular thermal conductivity using heater-thermometer hybrid diamond nanosensors,” *Science Adv.*, vol. 7, no. 3, p. eabd7888, 2021.

[7] K. Okabe, N. Inada, C. Gota, Y. Harada, T. Funatsu, and S. Uchiyama, “Intracellular temperature mapping with a fluorescent polymeric thermometer and fluorescence lifetime imaging microscopy,” *Nat. Commun.*, vol. 3, no. 1, pp. 1–9, 2012.

[8] S. Kiyonaka, T. Kajimoto, R. Sakaguchi, D. Shinmi, M. Omatsu-Kanbe, H. Matsuura, H. Imamura, T. Yoshizaki, I. Hamachi, T. Morii, *et al.*, “Genetically encoded fluorescent thermosensors visualize subcellular thermoregulation in living cells,” *Nat. Methods*, vol. 10, no. 12, pp. 1232–1238, 2013.

[9] C. Mi, J. Zhou, F. Wang, G. Lin, and D. Jin, “Ultrasensitive ratiometric nanothermometer with large dynamic range and photostability,” *Chem. Mat.*, vol. 31, no. 22, pp. 9480–9487, 2019.

[10] L. Marciniak, K. Prorok, and A. Bednarkiewicz, "Size dependent sensitivity of Yb^{3+}, Er^{3+} up-converting luminescent nano-thermometers," *J. Mater. Chem. C*, vol. 5, no. 31, pp. 7890–7897, 2017.

[11] J. A. O. Galindo, A. R. Pessoa, L. F. dos Santos, A. M. Amaral, R. R. Gonçalves, and L. de S. Menezes, "Influence of the surrounding medium on the luminescence-based thermometric properties of single Yb^{3+}/Er^{3+} codoped yttria nanocrystals," *Nanoscale Adv.*, vol. 3, no. 21, pp. 6231–6241, 2021.

[12] F. Wang, J. Wang, and X. Liu, "Direct evidence of a surface quenching effect on size-dependent luminescence of upconversion nanoparticles," *Angew. Chem., Int. Ed.*, vol. 49, no. 41, pp. 7456–7460, 2010.

[13] F. T. Rabouw, P. T. Prins, P. Villanueva-Delgado, M. Castelijns, R. G. Geitenbeek, and A. Meijerink, "Quenching pathways in $NaYF_4$:Er^{3+},Yb^{3+} upconversion nanocrystals," *ACS Nano*, vol. 12, no. 5, pp. 4812–4823, 2018. PMID: 29648802.

[14] L. de S. Menezes and C. B. de Araújo, "Optically detected thermal effects in rare-earth doped materials for host characterization, thermometric devices, nanothermometry and biothermometry," *J. Braz. Chem. Soc.*, vol. 26, no. 12, pp. 2405–2417, 2015.

[15] I. M. Gonçalves, "Termometria por conversão ascendente de energia em microcristais individuais de $NaYF_4$ codopados com Yb^{3+} e Er^{3+}," Master's thesis, UFPE, maio 2019.

[16] M. Kardar, *Statistical physics of particles*. Cambridge University Press, 2007.

[17] F. Auzel, "Multiphonon processes, cross-relaxation and up-conversion in ion-activated solids, exemplified by minilaser materials," in *Radiationless processes*, pp. 213–286, Springer, 1980.

[18] B. di Bartolo, *Luminescence of inorganic solids*. Springer Science & Business Media, 2012.

[19] M. Weber, "Multiphonon relaxation of rare-earth ions in yttrium orthoaluminate," *Phys. Rev. B*, vol. 8, no. 1, p. 54, 1973.

[20] M. D. Dramićanin, "Sensing temperature via downshifting emissions of lanthanide-doped metal oxides and salts. A review," *Methods Appl. Fluoresc*, vol. 4, no. 4, p. 042001, 2016.

[21] F. Auzel, "Multiphonon-assisted anti-stokes and stokes fluorescence of triply ionized rare-earth ions," *Phys. Rev. B*, vol. 13, no. 7, p. 2809, 1976.

[22] L. de S. Menezes, G. S. Maciel, C. B. de Araújo, and Y. Messaddeq, "Phonon-assisted cooperative energy transfer and frequency upconversion in a Yb^{3+}/Tb^{3+} codoped fluoroindate glass," *J. Appl. Phys.*, vol. 94, no. 2, pp. 863–866, 2003.

[23] I. M. Gonçalves, A. R. Pessoa, C. Hazra, Y. S. Correales, S. J. L. Ribeiro, and L. de S. Menezes, "Phonon-assisted NIR-to-visible upconversion in single β-$NaYF_4$ microcrystals codoped with Er^{3+} and Yb^{3+} for microthermometry applications: Experiment and theory," *J. Lumin.*, vol. 231, p. 117801, 2021.

[24] R. Galvão, L. F. dos Santos, K. de O. Lima, R. R. Gonçalves, and L. de S. Menezes, "Single Er^{3+}/Yb^{3+}-codoped yttria nanocrystals for temperature sensing: Experimental characterization and theoretical modeling," *J. Phys. Chem. C*, vol. 125, no. 27, pp. 14807–14817, 2021.

[25] G. S. Maciel, M. A. R. C. Alencar, C. B. de Araújo, and A. Patra, "Upconversion emission of $BaTiO_3$: Er^{3+} nanocrystals: Influence of temperature and surrounding medium," *J. Nanosci. Nanotechnol.*, vol. 10, no. 3, pp. 2143–2148, 2010.

[26] A. D. Pickel, A. Teitelboim, E. M. Chan, N. J. Borys, P. J. Schuck, and C. Dames, "Apparent self-heating of individual upconverting nanoparticle thermometers," *Nat. Commun.*, vol. 9, no. 1, pp. 1–12, 2018.

[27] A. Skripka, A. Benayas, R. Marin, P. Canton, E. Hemmer, and F. Vetrone, "Double rare-earth nanothermometer in aqueous media: opening the third optical transparency window to temperature sensing," *Nanoscale*, vol. 9, no. 9, pp. 3079–3085, 2017.

[28] M. Xu, X. Zou, Q. Su, W. Yuan, C. Cao, Q. Wang, X. Zhu, W. Feng, and F. Li, "Ratiometric nanothermometer in vivo based on triplet sensitized upconversion," *Nat. Commun.*, vol. 9, no. 1, pp. 1–7, 2018.

[29] M. A. R. C. Alencar, G. S. Maciel, C. B. de Araújo, and A. Patra, "Er^{3+}-doped $BaTiO_3$ nanocrystals for thermometry: influence of nanoenvironment on the sensitivity of a fluorescence based temperature sensor," *Appl. Phys. Lett.*, vol. 84, no. 23, pp. 4753–4755, 2004.

[30] M. Quintanilla, A. Benayas, and R. Naccache, *Thermometry at the nanoscale: techniques and selected applications*, vol. 38, ch. Luminescent nanothermometry with lanthanide-doped nanoparticles, p. 124. 2015.

[31] L. de S. Menezes, “Conversão ascendente de energia em vidros fluoroindatos dopados com neodímio,” Master’s thesis, UFPE, 1996.

[32] V. K. Rai, “Temperature sensors and optical sensors,” *Appl. Phys. B*, vol. 88, no. 2, pp. 297–303, 2007.

[33] S. Kiyonaka, T. Kajimoto, R. Sakaguchi, D. Shinmi, M. Omatsu-Kanbe, H. Matsuura, H. Imamura, T. Yoshizaki, I. Hamachi, T. Morii, *et al.*, “Genetically encoded fluorescent thermosensors visualize subcellular thermoregulation in living cells,” *Nat. Methods*, vol. 10, no. 12, pp. 1232–1238, 2013.

[34] M. Nakano, Y. Arai, I. Kotera, K. Okabe, Y. Kamei, and T. Nagai, “Genetically encoded ratiometric fluorescent thermometer with wide range and rapid response,” *PloS One*, vol. 12, no. 2, p. e0172344, 2017.

[35] T. Barilero, T. Le Saux, C. Gosse, and L. Jullien, “Fluorescent thermometers for dual-emission-wavelength measurements: Molecular engineering and application to thermal imaging in a microsystem,” *Anal. Chem.*, vol. 81, no. 19, pp. 7988–8000, 2009. PMID: 19711963.

[36] W. Jung, Y. W. Kim, D. Yim, and J. Y. Yoo, “Microscale surface thermometry using SU8/Rhodamine-B thin layer,” *Sens. Actuator A Phys.*, vol. 171, no. 2, pp. 228–232, 2011.

[37] T.-R. Xie, C.-F. Liu, and J.-S. Kang, “Dye-based mito-thermometry and its application in thermogenesis of brown adipocytes,” *Biophys. Rep.*, vol. 3, no. 4, pp. 85–91, 2017.

[38] J. Qiao, Y.-H. Hwang, C.-F. Chen, L. Qi, P. Dong, X.-Y. Mu, and D.-P. Kim, “Ratiometric fluorescent polymeric thermometer for thermogenesis investigation in living cells,” *Anal. Chem.*, vol. 87, no. 20, pp. 10535–10541, 2015.

[39] J. Qiao, C. Chen, D. Shangguan, X. Mu, S. Wang, L. Jiang, and L. Qi, “Simultaneous monitoring of mitochondrial temperature and ATP fluctuation using fluorescent probes in living cells,” *Anal. Chem.*, vol. 90, no. 21, pp. 12553–12558, 2018.

[40] R. Tanimoto, T. Hiraiwa, Y. Nakai, Y. Shindo, K. Oka, N. Hiroi, and A. Funahashi, "Detection of temperature difference in neuronal cells," *Sci. Rep.*, vol. 6, no. 1, pp. 1–10, 2016.

[41] H. Zhao, A. Vomiero, and F. Rosei, "Tailoring the heterostructure of colloidal quantum dots for ratiometric optical nanothermometry," *Small*, vol. 16, no. 28, p. 2000804, 2020.

[42] Y. Han, Y. Liu, H. Zhao, A. Vomiero, and R. Li, "Highly efficient ratiometric nanothermometers based on colloidal carbon quantum dots," *J. Mater. Chem. B*, vol. 9, no. 20, pp. 4111–4119, 2021.

[43] Y. Takei, S. Arai, A. Murata, M. Takabayashi, K. Oyama, S. Ishiwata, S. Takeoka, and M. Suzuki, "A nanoparticle-based ratiometric and self-calibrated fluorescent thermometer for single living cells," *ACS Nano*, vol. 8, no. 1, pp. 198–206, 2014.

[44] C. D. S. Brites, S. Balabhadra, and L. D. Carlos, "Lanthanide-based thermometers: at the cutting-edge of luminescence thermometry," *Adv. Opt. Mater.*, vol. 7, no. 5, p. 1801239, 2019.

[45] S. Huang, S. Liu, K. Wang, C. Yang, Y. Luo, Y. Zhang, B. Cao, Y. Kang, and M. Wang, "Highly fluorescent and bioresorbable polymeric nanoparticles with enhanced photostability for cell imaging," *Nanoscale*, vol. 7, no. 3, pp. 889–895, 2015.

[46] H. Dong, L.-D. Sun, and C.-H. Yan, "Upconversion emission studies of single particles," *Nano Today*, vol. 35, p. 100956, 2020.

[47] O. A. Savchuk, J. J. Carvajal, J. Massons, C. Cascales, M. Aguiló, and F. Díaz, "Novel low-cost, compact and fast signal processing sensor for ratiometric luminescent nanothermometry," *Sens. Actuators, A*, vol. 250, pp. 87–95, 2016.

[48] R. G. Geitenbeek, B. B. Salzmann, A.-E. Nieuwelink, A. Meijerink, and B. M. Weckhuysen, "Chemically and thermally stable lanthanide-doped Y_2O_3 nanoparticles for remote temperature sensing in catalytic environments," *Chem. Eng. Sci.*, vol. 198, pp. 235–240, 2019.

[49] G. Liu and B. Jacquier, *Spectroscopic properties of rare earths in optical materials*, vol. 83. Springer Science & Business Media, 2006.

[50] F. Auzel, "Up-conversions in RE-doped solids," in *Spectroscopic properties of rare earths in optical materials*, pp. 266–319, Springer, 2005.

[51] G. H. Dieke, "Spectra and energy levels of rare earth ions in crystals.," 1968.

[52] R. Galvão, L. F. d. Santos, R. R. Gonçalves, and L. de S. Menezes, "Fluorescence intensity ratio-based temperature sensor with single Nd^{3+}: Y_2O_3 nanoparticles: Experiment and theoretical modeling," *Nano Select*, vol. 2, no. 2, pp. 346–356, 2021.

[53] D. A. Gálico, I. O. Mazali, and F. A. Sigoli, "Nanothermometer based on intensity variation and emission lifetime of europium (III) benzoylacetonate complex," *J. Lumin.*, vol. 192, pp. 224–230, 2017.

[54] J. Drabik, R. Kowalski, and L. Marciniak, "Enhancement of the sensitivity of single band ratiometric luminescent nanothermometers based on Tb^{3+} ions through activation of the cross relaxation process," *Sci. Rep.*, vol. 10, no. 1, pp. 1–11, 2020.

[55] S. Zhou, G. Jiang, X. Li, S. Jiang, X. Wei, Y. Chen, M. Yin, and C. Duan, "Strategy for thermometry via Tm^{3+}-doped $NaYF_4$ core-shell nanoparticles," *Opt. Lett.*, vol. 39, no. 23, pp. 6687–6690, 2014.

[56] W. Zhou, F. Pan, L. Zhou, D. Hou, Y. Huang, Y. Tao, and H. Liang, "Site occupancies, luminescence, and thermometric properties of LiY_9 $(SiO_4)_6O_2$: Ce^{3+} phosphors," *Inorganic chemistry*, vol. 55, no. 20, pp. 10415–10424, 2016.

[57] J. Drabik, K. Ledwa, and Ł. Marciniak, "Implementing defects for ratiometric luminescence thermometry," *Nanomaterials*, vol. 10, no. 7, p. 1333, 2020.

[58] Y. Chen, J. Qiu, Z. Chen, Y. Zhao, B. Li, and C. Zeng, "New luminescent lanthanide complexes and Tb,Eu co-doped complex as a wide temperature self-calibrating thermometer," *Dyes Pigm.*, vol. 194, p. 109671, 2021.

[59] H. Chen, G. Bai, Q. Yang, Y. Hua, S. Xu, and L. Chen, "Non-contact fluorescence intensity ratio optical thermometer based on Yb^{3+}/Nd^{3+} codoped $Bi_4Ti_3O_{12}$ microcrystals," *J. Lumin.*, vol. 221, p. 117095, 2020.

[60] K. Soler-Carracedo, I. R. Martín, F. Lahoz, H. C. Vasconcelos, A. D. Lozano-Gorrín, L. L. Martín, and F. Paz-Buclatin, "Er^{3+}/Ho^{3+} codoped nanogarnet as an optical FIR

based thermometer for a wide range of high and low temperatures," *J. Alloys Compd.*, vol. 847, p. 156541, 2020.

[61] L. Marciniak, A. Bednarkiewicz, and W. Strek, "The impact of nanocrystals size on luminescent properties and thermometry capabilities of Cr, Nd doped nanophosphors," *Sens. Actuators B Chem.*, vol. 238, pp. 381–386, 2017.

[62] P. V. dos Santos, M. T. de Araujo, A. S. Gouveia-Neto, J. A. Medeiros Neto, and A. S. B. Sombra, "Optical temperature sensing using upconversion fluorescence emission in Er^{3+}/Yb^{3+}-codoped chalcogenide glass," *Appl. Phys. Lett.*, vol. 73, no. 5, pp. 578–580, 1998.

[63] X. Zhu, W. Feng, J. Chang, Y.-W. Tan, J. Li, M. Chen, Y. Sun, and F. Li, "Temperature-feedback upconversion nanocomposite for accurate photothermal therapy at facile temperature," *Nat. Commun.*, vol. 7, no. 1, pp. 1–10, 2016.

[64] X. Zhu, J. Li, X. Qiu, Y. Liu, W. Feng, and F. Li, "Upconversion nanocomposite for programming combination cancer therapy by precise control of microscopic temperature," *Nat. Commun.*, vol. 9, no. 1, pp. 1–11, 2018.

[65] A. R. N. Bastos, C. D. S. Brites, P. A. Rojas-Gutierrez, C. DeWolf, R. A. S. Ferreira, J. A. Capobianco, and L. D. Carlos, "Thermal properties of lipid bilayers determined using upconversion nanothermometry," *Adv. Funct. Mater.*, vol. 29, no. 48, p. 1905474, 2019.

[66] A. Teitelboim, B. Tian, D. J. Garfield, A. Fernandez-Bravo, A. C. Gotlin, P. J. Schuck, B. E. Cohen, and E. M. Chan, "Energy transfer networks within upconverting nanoparticles are complex systems with collective, robust, and history-dependent dynamics," *J. Phys. Chem. C*, vol. 123, no. 4, pp. 2678–2689, 2019.

[67] W. Xu, Z. Chen, J. Sun, J. Xu, H. Hao, D. Li, Y. Song, Y. Wang, and X. Zhang, "Non-contact ratiometric thermometer of $NaLuF_4$: Yb^{3+}/Er^{3+} phosphors based on multi-phonon assisted excitation," *J. Alloys Compd.*, vol. 766, pp. 305–311, 2018.

[68] A. M. Kaczmarek, H. S. Jena, C. Krishnaraj, H. Rijckaert, S. K. P. Veerapandian, A. Meijerink, and P. Van Der Voort, "Luminescent ratiometric thermometers based on a 4f–3d grafted covalent organic framework to locally measure temperature gradients during catalytic reactions," *Angew. Chem.*, vol. 133, no. 7, pp. 3771–3780, 2021.

[69] R. G. Geitenbeek, A.-E. Nieuwelink, T. S. Jacobs, B. B. V. Salzmann, J. Goetze, A. Meijerink, and B. M. Weckhuysen, “In situ luminescence thermometry to locally measure temperature gradients during catalytic reactions,” *ACS Catal.*, vol. 8, no. 3, pp. 2397–2401, 2018.

[70] F. T. Rabouw, S. A. Den Hartog, T. Senden, and A. Meijerink, “Photonic effects on the förster resonance energy transfer efficiency,” *Nature Commun.*, vol. 5, no. 1, pp. 1–6, 2014.

[71] L. Novotny and B. Hecht, *Principles of nano-optics*. Cambridge university press, 2012.

[72] B. Henderson and G. F. Imbusch, *Optical spectroscopy of inorganic solids*, vol. 44. Oxford University Press, 2006.

[73] P. Guyot-Sionnest, B. Wehrenberg, and D. Yu, “Intraband relaxation in cdse nanocrystals and the strong influence of the surface ligands,” *J. Chem. Phys.*, vol. 123, no. 7, p. 074709, 2005.

[74] A. Aharoni, D. Oron, U. Banin, E. Rabani, and J. Jortner, “Long-range electronic-to-vibrational energy transfer from nanocrystals to their surrounding matrix environment,” *Phys. Rev. Lett.*, vol. 100, no. 5, p. 057404, 2008.

[75] A. Erdemir and C. Donnet, “Tribology of diamond-like carbon films: recent progress and future prospects,” *J. Phys. D: Appl. Phys.*, vol. 39, no. 18, p. R311, 2006.

[76] R. Schirhagl, K. Chang, M. Loretz, and C. L. Degen, “Nitrogen-vacancy centers in diamond: nanoscale sensors for physics and biology,” *Ann. Rev. Phys. Chem.*, vol. 65, pp. 83–105, 2014.

[77] Y. Yang, C. Mi, F. Jiao, X. Su, X. Li, L. Liu, J. Zhang, F. Yu, Y. Liu, and Y. Mai, “A novel multifunctional upconversion phosphor: $\mathrm{Yb}^{3+}/\mathrm{Er}^{3+}$ codoped $\mathrm{La}_2\mathrm{S}_3$,” *J. Am. Ceram. Soc.*, vol. 97, no. 6, pp. 1769–1775, 2014.

[78] L. Rondin, *Réalisation d’un magnétomètre à centre coloré NV du diamant*. PhD thesis, École normale supérieure de Cachan-ENS Cachan, 2012.

[79] F. Jelezko and J. Wrachtrup, “Single defect centres in diamond: A review,” *Phys. Status Solidi A*, vol. 203, no. 13, pp. 3207–3225, 2006.

[80] L. Childress and R. Hanson, "Diamond NV centers for quantum computing and quantum networks," *MRS Bulletin*, vol. 38, no. 2, pp. 134–138, 2013.

[81] "Colored diamonds." `https://diamonds.com/colored-diamonds/`, 2021. Accessed: 2021-12-07.

[82] N. Mizuochi, T. Makino, H. Kato, D. Takeuchi, M. Ogura, H. Okushi, M. Nothaft, P. Neumann, A. Gali, F. Jelezko, *et al.*, "Electrically driven single-photon source at room temperature in diamond," *Nat. Photon*, vol. 6, no. 5, pp. 299–303, 2012.

[83] E. D. C. Sánchez, *Nanoscale magnetometry with a microcontroller-based magnetometer using a single nitrogen-vacancy defect in nanodiamond*. PhD thesis, Universidade Federal de Pernambuco, 2020.

[84] J. Klatzow, J. N. Becker, P. M. Ledingham, C. Weinzetl, K. T. Kaczmarek, D. J. Saunders, J. Nunn, I. A. Walmsley, R. Uzdin, and E. Poem, "Experimental demonstration of quantum effects in the operation of microscopic heat engines," *Phys. Rev. Lett.*, vol. 122, no. 11, p. 110601, 2019.

[85] G. Kucsko, P. C. Maurer, N. Y. Yao, M. Kubo, H. J. Noh, P. K. Lo, H. Park, and M. D. Lukin, "Nanometre-scale thermometry in a living cell," *Nature*, vol. 500, no. 7460, pp. 54–58, 2013.

[86] L. Rondin, J.-P. Tetienne, T. Hingant, J.-F. Roch, P. Maletinsky, and V. Jacques, "Magnetometry with nitrogen-vacancy defects in diamond," *Rep. Prog. Phys.*, vol. 77, no. 5, p. 056503, 2014.

[87] E. C. Sánchez, A. Pessoa, A. Amaral, and L. de S. Menezes, "Microcontroller-based magnetometer using a single nitrogen-vacancy defect in a nanodiamond," *AIP Adv.*, vol. 10, no. 2, p. 025323, 2020.

[88] F. Dolde, H. Fedder, M. W. Doherty, T. Nöbauer, F. Rempp, G. Balasubramanian, T. Wolf, F. Reinhard, L. C. Hollenberg, F. Jelezko, *et al.*, "Electric-field sensing using single diamond spins," *Nat. Phys.*, vol. 7, no. 6, pp. 459–463, 2011.

[89] M. Block, B. Kobrin, A. Jarmola, S. Hsieh, C. Zu, N. L. Figueroa, V. M. Acosta, J. Minguzzi, J. R. Maze, D. Budker, *et al.*, "Optically enhanced electric field sensing using nitrogen-vacancy ensembles," *Phys. Rev. Appl.*, vol. 16, no. 2, p. 024024, 2021.

[90] A. Laraoui, H. Aycock-Rizzo, Y. Gao, X. Lu, E. Riedo, and C. A. Meriles, "Imaging thermal conductivity with nanoscale resolution using a scanning spin probe," *Nat. commun.*, vol. 6, no. 1, pp. 1–8, 2015.

[91] Y.-K. Tzeng, P.-C. Tsai, H.-Y. Liu, O. Y. Chen, H. Hsu, F.-G. Yee, M.-S. Chang, and H.-C. Chang, "Time-resolved luminescence nanothermometry with nitrogen-vacancy centers in nanodiamonds," *Nano Lett.*, vol. 15, no. 6, pp. 3945–3952, 2015.

[92] K. V. Bogdanov, M. V. Zhukovskaya, V. Y. Osipov, E. V. Ushakova, M. A. Baranov, K. Takai, A. Rampersaud, and A. V. Baranov, "Highly intensive emission of the NV-centers in synthetic HPHT microdiamonds at low nitrogen doping," *APL Mater.*, vol. 6, no. 8, p. 086104, 2018.

[93] T. Chakraborty, F. Lehmann, J. Zhang, S. Borgsdorf, N. Wöhrl, R. Remfort, V. Buck, U. Köhler, and D. Suter, "CVD growth of ultrapure diamond, generation of NV centers by ion implantation, and their spectroscopic characterization for quantum technological applications," *Phys. Rev. Mater.*, vol. 3, no. 6, p. 065205, 2019.

[94] A. Haque and S. Sumaiya, "An overview on the formation and processing of nitrogen-vacancy photonic centers in diamond by ion implantation," *J. Manuf. Mater. Process*, vol. 1, no. 1, p. 6, 2017.

[95] J. Loubser and J. van Wyk, "Electron spin resonance in the study of diamond," *Rep. Prog. Phys.*, vol. 41, no. 8, p. 1201, 1978.

[96] M. W. Doherty, N. B. Manson, P. Delaney, F. Jelezko, J. Wrachtrup, and L. C. L. Hollenberg, "The nitrogen-vacancy colour centre in diamond," *Phys. Reports*, vol. 528, no. 1, pp. 1–45, 2013.

[97] J. P. Goss, R. Jones, P. R. Briddon, G. Davies, A. T. Collins, A. Mainwood, J. A. Van Wyk, J. M. Baker, M. E. Newton, A. Stoneham, *et al.*, "Comment on "electronic structure of the N-V center in diamond: Theory"," *Phys. Rev. B*, vol. 56, no. 24, p. 16031, 1997.

[98] J. R. Maze, A. Gali, E. Togan, Y. Chu, A. Trifonov, E. Kaxiras, and M. D. Lukin, "Properties of nitrogen-vacancy centers in diamond: the group theoretic approach," *New J. Phys.*, vol. 13, p. 025025, feb 2011.

[99] M. W. Doherty, N. B. Manson, P. Delaney, and L. C. L. Hollenberg, “The negatively charged nitrogen-vacancy centre in diamond: the electronic solution,” *New J. Phys.*, vol. 13, no. 2, p. 025019, 2011.

[100] M. W. Doherty, F. Dolde, H. Fedder, F. Jelezko, J. Wrachtrup, N. B. Manson, and L. C. L. Hollenberg, “Theory of the ground-state spin of the NV^- center in diamond,” *Phys. Rev. B*, vol. 85, no. 20, p. 205203, 2012.

[101] V. M. Acosta, E. Bauch, M. P. Ledbetter, C. Santori, K.-M. Fu, P. E. Barclay, R. G. Beausoleil, H. Linget, J. F. Roch, F. Treussart, *et al.*, “Diamonds with a high density of nitrogen-vacancy centers for magnetometry applications,” *Phys. Rev. B*, vol. 80, no. 11, p. 115202, 2009.

[102] P. Neumann, R. Kolesov, V. Jacques, J. Beck, J. Tisler, A. Batalov, L. Rogers, N. Manson, G. Balasubramanian, F. Jelezko, *et al.*, “Excited-state spectroscopy of single NV defects in diamond using optically detected magnetic resonance,” *New J. Phys.*, vol. 11, no. 1, p. 013017, 2009.

[103] M. L. Goldman, M. W. Doherty, A. Sipahigil, N. Y. Yao, S. D. Bennett, N. B. Manson, A. Kubanek, and M. D. Lukin, “State-selective intersystem crossing in nitrogen-vacancy centers,” *Phys. Rev. B*, vol. 91, p. 165201, Apr 2015.

[104] J. Harrison, M. J. Sellars, and N. B. Manson, “Optical spin polarisation of the N-V centre in diamond,” *J. Lumin.*, vol. 107, no. 1-4, pp. 245–248, 2004.

[105] V. M. Acosta, C. Santori, A. Faraon, Z. Huang, K.-M. C. Fu, A. Stacey, D. A. Simpson, K. Ganesan, S. Tomljenovic-Hanic, A. D. Greentree, S. Prawer, and R. G. Beausoleil, “Dynamic stabilization of the optical resonances of single nitrogen-vacancy centers in diamond,” *Phys. Rev. Lett.*, vol. 108, p. 206401, May 2012.

[106] C. L. Degen, “Scanning magnetic field microscope with a diamond single-spin sensor,” *Appl. Phys. Lett.*, vol. 92, no. 24, p. 243111, 2008.

[107] J. J. Sakurai and E. D. Commins, *Modern quantum mechanics, revised edition*. American Association of Physics Teachers, 1995.

[108] G. Davies, “Vibronic spectra in diamond,” *J. of Phys. C: Solid State Phys.*, vol. 7, no. 20, p. 3797, 1974.

[109] M. W. Doherty, V. M. Acosta, A. Jarmola, M. S. J. Barson, N. B. Manson, D. Budker, and L. C. L. Hollenberg, "Temperature shifts of the resonances of the NV^- center in diamond," *Phys. Rev. B*, vol. 90, p. 041201, Jul 2014.

[110] T. Plakhotnik, M. W. Doherty, J. H. Cole, R. Chapman, and N. B. Manson, "All-optical thermometry and thermal properties of the optically detected spin resonances of the NV —-center in nanodiamond," *Nano Lett.*, vol. 14, no. 9, pp. 4989–4996, 2014.

[111] M. W. Doherty, V. V. Struzhkin, D. A. Simpson, L. P. McGuinness, Y. Meng, A. Stacey, T. J. Karle, R. J. Hemley, N. B. Manson, L. C. Hollenberg, *et al.*, "Electronic properties and metrology applications of the diamond NV^- center under pressure," *Phys. Rev. Lett.*, vol. 112, no. 4, p. 047601, 2014.

[112] M. Popov, V. Churkin, A. Kirichenko, V. Denisov, D. Ovsyannikov, B. Kulnitskiy, I. Perezhogin, V. Aksenenkov, and V. Blank, "Raman spectra and bulk modulus of nanodiamond in a size interval of 2–5 nm," *Nanoscale Res. Lett.*, vol. 12, no. 1, pp. 1–6, 2017.

[113] M. Fujiwara, S. Sun, A. Dohms, Y. Nishimura, K. Suto, Y. Takezawa, K. Oshimi, L. Zhao, N. Sadzak, Y. Umehara, *et al.*, "Real-time nanodiamond thermometry probing in vivo thermogenic responses," *Science Adv.*, vol. 6, no. 37, p. eaba9636, 2020.

[114] L. Fu, G. Liu, X. Yang, Z. Fu, and Y. Yang, "Up-conversion luminescent properties and optical thermometry of $LaMgAl_{11}O_{19}$: Yb^{3+}/Er^{3+} phosphors," *Ceram. Int.*, vol. 41, no. 10, pp. 14064–14069, 2015.

[115] L. Marciniak, K. Waszniewska, A. Bednarkiewicz, D. Hreniak, and W. Strek, "Sensitivity of a nanocrystalline luminescent thermometer in high and low excitation density regimes," *J. Phys. Chem. C*, vol. 120, no. 16, pp. 8877–8882, 2016.

[116] V. M. Acosta, E. Bauch, M. P. Ledbetter, A. Waxman, L.-S. Bouchard, and D. Budker, "Temperature dependence of the nitrogen-vacancy magnetic resonance in diamond," *Phys. Rev. Lett.*, vol. 104, p. 070801, Feb 2010.

[117] C. Foy, L. Zhang, M. E. Trusheim, K. R. Bagnall, M. Walsh, E. N. Wang, and D. R. Englund, "Wide-field magnetic field and temperature imaging using nanoscale quantum sensors," *ACS Appl. Mater. Interfaces*, vol. 12, no. 23, pp. 26525–26533, 2020.

[118] C. D. S. Brites, A. Millán, and L. D. Carlos, *Handbook on the Physics and Chemistry of Rare Earths*, vol. 49, pp. 339–427. Elsevier, 2016.

[119] R. C. St.. John, *Applied linear regression models*. Taylor & Francis, 1983.

[120] P. Neumann, I. Jakobi, F. Dolde, C. Burk, R. Reuter, G. Waldherr, J. Honert, T. Wolf, A. Brunner, J. H. Shim, *et al.*, "High-precision nanoscale temperature sensing using single defects in diamond," *Nano Lett.*, vol. 13, no. 6, pp. 2738–2742, 2013.

[121] G. S. Kino and T. R. Corle, *Confocal scanning optical microscopy and related imaging systems*. Academic Press, 1996.

[122] M. Born and E. Wolf, *Principles of optics: electromagnetic theory of propagation, interference and diffraction of light*. Elsevier, 2013.

[123] R. Barakat, "Application of apodization to increase two-point resolution by the sparrow criterion. i. coherent illumination," *J. Opt. Soc. Am.*, vol. 52, pp. 276–283, Mar 1962.

[124] A. Carrasco-Casado, "Design of an optical-communication link with mars," 2016.

[125] J. G. White, W. B. Amos, and M. Fordham, "An evaluation of confocal versus conventional imaging of biological structures by fluorescence light microscopy.," *J. Cell. Biol.*, vol. 105, no. 1, pp. 41–48, 1987.

[126] B. A. R. Aiken, W. P. Hsu, and E. Matijević, "Preparation and properties of monodispersed colloidal particles of lanthanide compounds: III, yttrium III and mixed yttrium III/cerium III systems," *J. Am. Ceram. Soc.*, vol. 71, no. 10, pp. 845–853, 1988.

[127] L. F. Dos Santos, J. C. Martins, K. O. Lima, L. F. T. Gomes, M. T. De Melo, A. C. Tedesco, L. D. Carlos, R. A. S. Ferreira, and R. R. Gonçalves, "In vitro assays and nanothermometry studies of infrared-to-visible upconversion of nanocrystalline Er^{3+}, Yb^{3+} co-doped Y_2O_3 nanoparticles for theranostic applications," *Phys. B: Condens. Matter*, vol. 624, p. 413447, 2022.

[128] X. Yang, Z. Wu, Z. Yang, X. Zhao, C. Song, M. Yuan, K. Han, H. Wang, S. Li, and X. Xu, "Flame-made Y_2O_3: Yb^{3+}/Er^{3+} upconversion nanoparticles: Mass production synthesis, multicolor tuning and thermal sensing studies," *J. Alloys Compd.*, vol. 854, p. 157078, 2021.

[129] R. C. Powell, *Physics of Solid-State Laser Materials*, vol. 1. Springer Science & Business Media, 1998.

[130] P. Du, L. Luo, and J. S. Yu, "Facile synthesis of Er^{3+}/Yb^{3+}-codoped $NaYF_4$ nanoparticles: a promising multifunctional upconverting luminescent material for versatile applications," *RSC Adv.*, vol. 6, no. 97, pp. 94539–94546, 2016.

[131] X. Cheng, K. Yang, J. Wang, L. Yang, and X. Cheng, "Up-conversion luminescence and optical temperature sensing behaviour of Yb^{3+}/Er^{3+} codoped $CaWO_4$ material," *Opt. Mater.*, vol. 58, pp. 449–453, 2016.

[132] J. Zhu, P. Du, and J. S. Yu, "Evolution of Er^{3+}/Yb^{3+}-codoped $NaGdF_4$ nanorods at room temperature for non-contact nanothermometer and optical heater," *Applied Physics A*, vol. 126, no. 3, pp. 1–10, 2020.

[133] A. Khalid, K. Chung, R. Rajasekharan, D. W. M. Lau, T. J. Karle, B. C. Gibson, and S. Tomljenovic-Hanic, "Lifetime reduction and enhanced emission of single photon color centers in nanodiamond via surrounding refractive index modification," *Sci. Rep.*, vol. 5, p. 11179, 2015.

[134] L. Gontrani, P. Tagliatesta, A. Agresti, S. Pescetelli, and M. Carbone, "New insights into the structure of glycols and derivatives: A comparative x-ray diffraction, raman and molecular dynamics study of ethane-1,2-diol, 2-methoxyethan-1-ol and 1,2-dimethoxy ethane," *Crystals*, vol. 10, 11 2020.

[135] S. Burikov, T. Dolenko, S. Patsaeva, Y. Starokurov, and V. Yuzhakov, "Raman and ir spectroscopy research on hydrogen bonding in water-ethanol systems," *Mol. Phys.*, vol. 108, no. 18, pp. 2427–2436, 2010.

[136] J. Zhao, Z. Lu, Y. Yin, C. McRae, J. A. Piper, J. M. Dawes, D. Jin, and E. M. Goldys, "Upconversion luminescence with tunable lifetime in $NaYF_4$:Yb, Er nanocrystals: role of nanocrystal size," *Nanoscale*, vol. 5, no. 3, pp. 944–952, 2013.

[137] M. Łukaszewicz, R. Tomala, and R. Lisiecki, "From upconversion to thermal radiation: spectroscopic properties of a submicron Y_2O_3: Er^{3+}, Yb^{3+} ceramic under ir excitation in an extremely broad temperature range," *J. Mater. Chem. C*, vol. 8, no. 3, pp. 1072–1082, 2020.

[138] S. Delice, M. Isik, and N. Gasanly, "Effect of heating rate on thermoluminescence characteristics of Y_2O_3 nanoparticles," *J. Lumin.*, vol. 212, pp. 233–237, 2019.

[139] W. R. Manning, O. Hunter, and B. R. Powell, "Elastic properties of polycrystalline yttrium oxide, dysprosium oxide, holmium oxide, and erbium oxide: room temperature measurements," *J. Am. Ceram. Soc.*, vol. 52, no. 8, pp. 436–442, 1969.

[140] P. Woźny, M. Runowski, and S. Lis, "Emission color tuning and phase transition determination based on high-pressure up-conversion luminescence in YVO_4: Yb^{3+}, Er^{3+} nanoparticles," *J. of Lumin.*, vol. 209, pp. 321–327, 2019.

[141] S. Goderski, M. Runowski, P. Woźny, V. Lavín, and S. Lis, "Lanthanide upconverted luminescence for simultaneous contactless optical thermometry and manometry–sensing under extreme conditions of pressure and temperature," *ACS Appl. Mater. Interfaces*, vol. 12, no. 36, pp. 40475–40485, 2020. PMID: 32805851.

[142] G. Boulon, G. Alombert-Goget, Y. Guyot, M. Guzik, T. Epicier, N. P. Blanchard, L. Chen, L. Hu, and W. Chen, "Conjugation of TEM-EDX and optical spectroscopy tools for the localization of Yb^{3+}, Er^{3+} and Co^{2+} dopants in laser glass ceramics composed of $MgAl_2O_4$ spinel nano-crystals embedded in SiO_2 glass," *J. Mater. Chem. C*, vol. 2, no. 44, pp. 9385–9397, 2014.

[143] G. Boulon, Y. Guyot, M. Guzik, T. Epicier, P. Gluchowski, D. Hreniak, and W. Strek, "Yb^{3+} ions distribution in YAG nanoceramics analyzed by both optical and TEM-EDX techniques," *J. Phys. Chem. C*, vol. 118, no. 28, pp. 15474–15486, 2014.

[144] M. Kraft, C. Wurth, V. Muhr, T. Hirsch, and U. Resch-Genger, "Particle-size-dependent upconversion luminescence of $NaYF_4$:Yb, Er nanoparticles in organic solvents and water at different excitation power densities," *Nano Res.*, vol. 11, no. 12, pp. 6360–6374, 2018.

[145] E. D. C. Sanchez, "Optically detected magnetic resonance in nanodiamonds with single nitrogen-vacancy defects," Master's thesis, UFPE, abril 2016.

[146] R. Loudon, *The quantum theory of light*. OUP Oxford, 2000.

[147] E. Suarez, D. Auwärter, T. J. Arruda, R. Bachelard, P. W. Courteille, C. Zimmermann, and S. Slama, "Photon-antibunching in the fluorescence of statistical ensembles of emitters at an optical nanofiber-tip," *N. J. Phys.*, vol. 21, no. 3, p. 035009, 2019.

[148] G.-Q. Liu, X. Feng, N. Wang, Q. Li, and R.-B. Liu, "Coherent quantum control of nitrogen-vacancy center spins near 1000 kelvin," *Nat. Commun.*, vol. 10, no. 1, pp. 1–8, 2019.

[149] D. M. Toyli, D. J. Christle, A. Alkauskas, B. B. Buckley, C. G. Van de Walle, and D. D. Awschalom, "Measurement and control of single nitrogen-vacancy center spins above 600 K," *Phys. Rev. X*, vol. 2, no. 3, p. 031001, 2012.